Macroscopic modelling of radio emission from ultra-high-energy-cosmic-ray-induced air showers




This work is part of the research program of the 'Stichting voor Fundamenteel Onderzoek der Materie (FOM)', which is financially supported by the 'Nederlandse Organisatie voor Wetenschappelijk Onderzoek (NWO)'.

Printed by: Ipskamp Drukkers, Enschede, December 2012

RIJKSUNIVERSITEIT GRONINGEN

Macroscopic modelling of radio emission from ultra-high-energy-cosmic-ray-induced air showers

Proefschrift

ter verkrijging van het doctoraat in de
Wiskunde en Natuurwetenschappen
aan de Rijksuniversiteit Groningen
op gezag van de
Rector Magnificus, dr. E. Sterken,
in het openbaar te verdedigen op
vrijdag 11 januari 2013
om 12.45 uur

door

Krijn Dominique de Vries

geboren op 4 april 1985
te Oldenzaal

Promotores:	Prof. dr. O. Scholten
	Prof. dr. K. Werner
Beoordelingscomissie:	Prof. dr. H. Falcke
	Prof. dr. F. Halzen
	Prof. dr. D. Seckel

Contents

Chapter 1

Introduction

1.1 The discovery of cosmic rays

The discovery of cosmic rays starts in 1895 when Becquerel finds a new type of radiation, radioactive radiation [1]. In the search for sources of this radioactive radiation it was believed that they were to be found in Earth materials. Several experiments were done to test this hypothesis using an electroscope originally developed by Theodore Wulf. It was also Wulf who performed several experiments at larger heights on the top of the Eiffel tower [2]. If the radiation was due to materials inside Earth a drop in the intensity was expected. Even though a drop was measured its magnitude was not large enough which lead to the conclusion that there must be another source for the radiation. Finally, it was Victor Hess who, with a series of balloon flights in 1912, resolved the source of the radiation [3]. His measurements showed that the radiation dropped in the first kilometer, but started to rise again up to twice the value that was measured at Earth's surface at around five kilometers height. From this experiment and several others performed in the following years, going up to even larger heights of 40 kilometers, Hess drew the conclusion that the source of this radiation must come from space.

1.2 Toward ultra-high-energy cosmic rays: Extensive air showers

After the discovery of cosmic rays more measurements were done to find the nature of these rays. This, for example, lead to the discovery of the already by Dirac predicted "positive electron" [4], the positron, by Anderson [5] who received the 1936 nobel prize together with Victor Hess for their discoveries [6]. It was also shown that at energies larger than 10^{14} eV the cosmic-ray flux is extremely small. In 1939 Pierre Victor Auger found that cosmic-ray events measured at Earth were coincident in time [7]. The conclusion was that these cosmic rays were secondary particles originating from more energetic particles colliding in the atmosphere, an air shower. From these measurements it was also concluded that the energy of the primary particle goes up to or even beyond 10^{15} eV. This discovery in combination with the low flux at the highest energies lead to the development of several air-shower detection experiments.

The era of Ultra-High-Energy Cosmic Rays (UHECR's), with energies typically larger than 10^{18} eV, started around 1960 with measurements at the Volcano Ranch experiment [8], and the prediction of a cut-off in the cosmic-ray spectrum at energies larger than 10^{20} eV. Greisen [9], Zatsepin and Kuzmin [10], predicted the interaction of high energy protons with the Cosmic Microwave Background (CMB) at these energies. Heavier nuclei will experience this interaction at higher energies, but as already noted by Greisen [9], photodesintegration will occur in the same energy range as the interaction with the CMB and a similar cut-off is expected.

As a direct consequence of these findings larger air shower arrays were constructed, such as SUGAR [11], Haverah park [12], and Yakutsk [13]. Nevertheless, it was only after 1990 when the first large scale UHECR detectors were build (AGASA [14], HiRes and HiRes-II [15]). The need for these large scale detectors is because of the extremely small flux at the highest energies which drops to one particle per square kilometer per century at energies of 10^{19} eV. Currently the largest cosmic-ray detectors are those at the Pierre Auger Observatory (POA) [16] on the Southern hemisphere and the Telescope Array [17] at the Northern hemisphere.

Along with these experiments came a better understanding of the extensive air shower itself which is currently known to be a disk of particles flying toward Earth with the speed of light. Initially simple models like the Heitler model [18, 19] were used to model the shower development. More recently extensive Monte Carlo codes like CORSIKA [20] and CONEX [21, 22] have been developed giving an accurate description of the shower. It

should be noted that the high energy interaction models inside CORSIKA and CONEX still find difficulties predicting the total muon number in the air shower [23, 24].
Since the shower consists mainly out of high energy photons producing a huge lepton content, it is no surprise that the two main detection methods are sensitive to the electronic and muonic content of the shower. At the Pierre Auger Obervatory, for example, the main detectors are the Surface Detector (SD) consisting out of water Cherenkov tanks measuring Cherenkov light emitted by high energy muons flying through and the Fluorescence Detector (FD) measuring light emitted from Nitrogen atoms that are exited by the electronic component in the air shower.
There are several physics goals addressed in the search of UHECRs. There is of course the GZK cut-off that is to be detected. Furthermore, at these extreme energies several questions are still unknown. What is the chemical composition of the initial cosmic ray? Where do these UHECR's come from, how are they accelerated? Is there a possibility for cosmic-ray astronomy? From the particle physics point of view the first interaction in Earth's atmosphere is of great interest. The center of mass energy of this first interaction is a factor 10-100 larger than the largest energies achieved at Earth based accelerators.

1.3 The cosmic-ray flux spectrum

Many of the open questions in cosmic-ray physics have been answered by measuring the cosmic-ray flux spectrum. The main features of this spectrum are shown in Fig. 1.1. The flux spectrum follows a steep non-thermal power law, scaling approximately E^{-3}. The first feature in the spectrum is the knee which is observed at an energy of $5 \cdot 10^{15}$ eV. There is still no clear explanation for this knee-like structure. One of the reasons for this structure might be that particles at these energy cannot be contained within their acceleration region any more. Another theory is that at these energies particles are not bound in the magnetic fields of the galaxy any more and start to leave the galaxy. In both models, the Larmor radius of particles with fixed energy scales with $1/Z$, where Z is the charge of the particle, it follows that the singly charged protons leave the acceleration or galaxy before the highly charged heavier ions. Additional information about the relative abundances of the different types of particles is needed to test these models.
A second knee-like structure is observed at an energy of $4 \cdot 10^{17}$ eV and can be explained by the iron atoms leaving the acceleration region or the

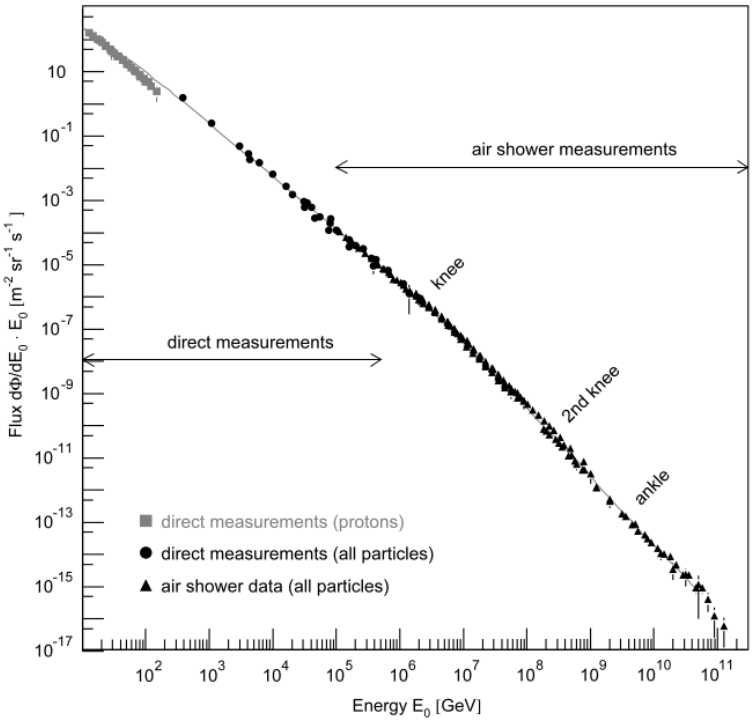

Figure 1.1: The main features of the cosmic-ray flux spectrum. Figure taken from [36].

galaxy. The ankle structure at $4 \cdot 10^{18}$ eV is believed to be the onset of the extragalactic component with a harder spectrum than the galactic component.

The current status of the different experimental efforts determining the cosmic-ray flux spectrum at the highest energies can be seen in Fig. 1.2, where the overall observed cosmic-ray flux spectrum, multiplied by E^2, is shown. It follows that the spectrum is measured up to energies of 10^{21} eV. The latest results at the PAO [37] and TA [38] give a strong hint for a GZK like cut-off at an energy around $10^{19} - 10^{20}$ eV. This is also seen in Fig. 1.3, where the latest results from the PAO are shown. Here the flux spectrum is multiplied by E^3, and a clear cut-off at an energy of $10^{19} - 10^{20}$ eV is observed. Several processes might be the cause for this cut-off, among which the GZK interaction of high energy protons with the CMB. The heavier primaries may decay through photodesintegration on the CMB. Another option might simply be that the accelerators are running out of steam. Therefore, it is of great importance to measure the spectrum above 10^{19} eV with more detail and obtain complementary information about the chemical composition of cosmic rays at these energies.

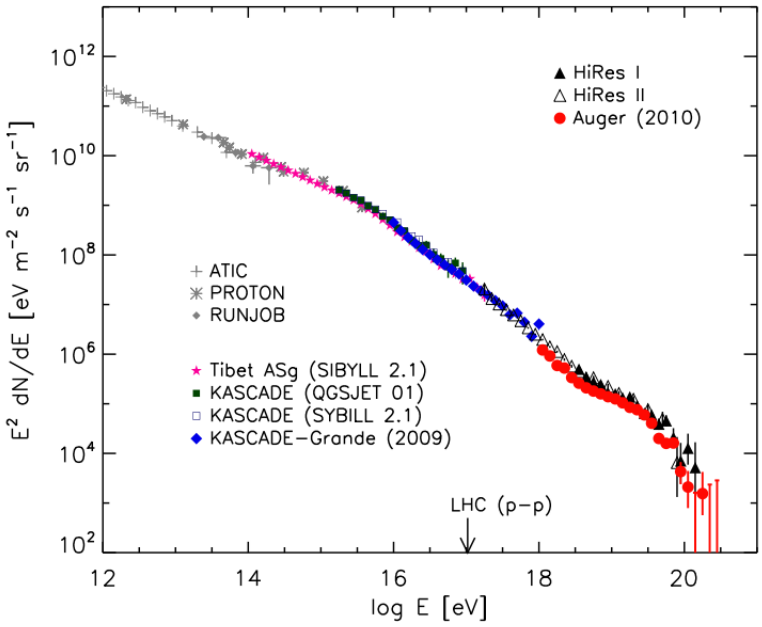

Figure 1.2: The cosmic-ray spectrum as measured by the different collaborations, ATIC [25], PROTON [26, 27], RUNJOB [28], TIBET [29], KASCADE [30], KASCADE-Grande [31], Akeno [32, 33], HiRes-MIA [23, 34], HiRes I and II [15], and Auger [35]. Figure taken from [36].

1.4 Radio emission from extensive air showers

Radio detection of air showers is a complementary technique to the FD and SD measurements. As already noticed by Allen [39] radio emission is sensitive to the air shower profile, which itself is a measure for the mass of the initial cosmic ray. Already in 1941 Blackett and Lovell proposed to use radar detection to measure air showers [40]. Radar waves were thought to reflect of the ionizing trail left behind by an air shower.
It would take another 20 years for the first detection of radio emission from air showers. A new mechanism was proposed where the emission was expected to be coherent over the typical size of the shower front which was known to be of the order of several meters, corresponding to emission in the MHz regime. Shortly thereafter Jelley *et al.* measured the first radio pulses from air showers [41]. This lead to a number of experiments over a wide frequency range. Several low frequency measurements were performed at Haverah Park [41, 42]. Also high frequency measurements were performed by Fegan *et. al.*, measuring radio pulses between 200 and 520 MHz [43]. Nevertheless, due to technical difficulties the detection of radio emission was not continued. A review of the history of the radio detection in this period is given in [39].

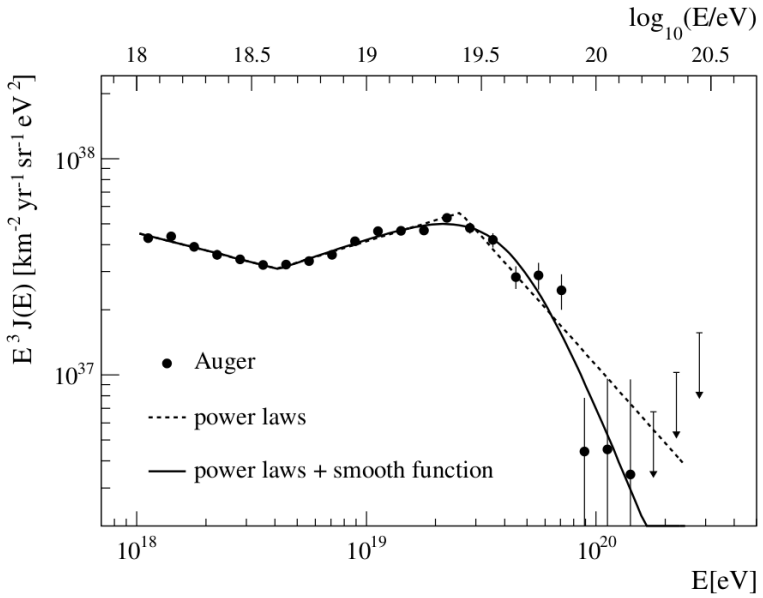

Figure 1.3: The cosmic-ray spectrum at the highest energies as measured by the Pierre Auger Collaboration. Figure taken from [37].

At the same time attempts were made to model radio emission from air showers. The first models shown to give the correct emission mechanisms were those developed by Askaryan [44] in 1962, who predicted that there would be a net electron excess in the shower front that would emit coherent radiation, while Kahn and Lerche [45] in 1966 developed a macroscopic model based on the geomagnetically induced transverse current in the shower front. Several other models have been developed by Colgate [46], Allen [39], Fuji and Nishimura [47], and Castagnoli *et al.* [48] using different approaches and air shower models. Even though these models already included the correct emission mechanisms, the used air shower models were too simplistic.

It was only in the early 21st century that radio detection from air showers was given a boost again. Measurements at the LOPES [49, 50] and CODALEMA [51, 52] sites gave a new impulse to the field. Plans were made for large scale arrays at the Pierre Auger Observatory [53, 54, 55, 56], LOFAR [57], and more recently at the Ice Cube site [58].

These measurements also gave an impulse to the theory of radio emission from air showers. Renewed efforts were done using more realistic shower geometries [59, 60]. Several new models were developed which can be separated in two categories, those giving a microscopic description adding the emission from single particles like REAS [61], and those following a macroscopic approach based on the currents and charge densities in the shower

like MGMR [62, 63]. There used to be a huge discrepancy between microscopic and macroscopic models, where the microscopic models predicted uni-polar pulses in time domain, and the macroscopic models predicted bi-polar pulses which differed a factor of ten in magnitude. These discrepancies have only recently been resolved [64].
Along with the convergence between the microscopic and macroscopic models came a better understanding of the emission mechanisms. The LOPES and CODALEMA [52] collaborations showed that the main emission mechanism was due to the deflection of charged particles in Earth's magnetic field. More recently [65], polarization studies showed that there is a secondary emission due to the net charge excess in the shower front as predicted by Askaryan [44].
The latest development from the theory side is the inclusion of Cherenkov effects in the emission that turn out to be crucial for an understanding of the signal at realistic observer distances [66]. Currently several codes have been developed that include these Cherenkov effects like CoREAS [67], ZHAires [68], SELFAS [69], and EVA [70]. These effects might have been observed at LOFAR [57] where the Lateral Distribution Function (LDF) of the radio signal is measured in great detail. Also radio emission from air showers at high frequencies (>200 MHz) has been detected by the ANITA collaboration [71], which might be a consequence of the Cherenkov effect due to which the signal is compressed in a very small time window leading to high frequency components in the emission.

1.5 Thesis overview

This thesis is based on two simulation codes that have been developed and expanded in the period starting from 2008 up to 2012. These are the Macroscopic Geo-Magnetic Radiation (MGMR) model [62, 63] and the Electric fields, using a Variable index of refraction in Air shower simulations (EVA) code [70]. A detailed description of both models is given in respectively Chapter 2 and Chapter 4 for MGMR and EVA. Comparison of MGMR simulations with the microscopic REAS3 [72] model will be shown in Chapter 3, and comparison to data measured at the Pierre Auger Observatory is given in Chapter 5. This follows a chronological order.
The structure of this thesis is thus based on the developments of the MGMR and EVA codes over time starting in 2008. To get a clear picture of these developments we consider the three crucial ingredients for modeling radio emission from air showers,

- The air shower

- The emission mechanisms
- The atmosphere.

1.5.1 The air shower

When a high-energy cosmic ray interacts in Earth's atmosphere, a cascade of secondary particles is induced. This can be visualized as a thin 'pancake' of particles flying toward Earth with approximately the speed of light. In the earliest version of MGMR the air shower is parameterized by two functions. These are the total particle number over time, the shower profile $N(t')$, where t' is the negative retarded emission time, and the longitudinal particle distribution in the shower front, $f_p(h)$, where h is the distance behind the shower front. The main parameter in this distribution is the typical thickness of the 'pancake' given by $L = 10\ m$ as obtained from air shower measurements. The lateral particle distribution in the shower front is neglected. These parameterizations are described in detail in Chapter 2. In Chapter 2, also the first improvement on the modeling of the air shower in MGMR is shown. Where previously the shower profile was parameterized, in the hybrid version of MGMR also shower profiles as obtained directly from Monte-Carlo simulations can be included. Furthermore, where the thickness of the longitudinal particle distribution in the shower front was first set to $L = 10$ m following air shower measurements, this is now obtained from Monte-Carlo simulations and set to $L = 3.9$ m.
In Chapter 3, the MGMR model is compared to the microscopic REAS3 model. It follows that at large observer distances the simulations are in very good agreement, for small observer distances the models still differ up to a factor of three. It is shown that this difference can be contributed to the different description of the air shower, which for REAS3 is based on a full Monte-Carlo simulation.
This difference is overcome by the EVA code as described in Chapter 4 [70]. The EVA code contains the CX-MC-GEO package which uses the pure cascade mode of the CONEX air shower simulation program to obtain the full three dimensional particle distributions in the shower front, the shower profile $N(t')$, the lateral particle distribution in the shower front $w_1(r)$, and the longitudinal particle distribution in the shower front $w_2(r, h)$ which depends on the radial distance from the shower axis r. These distributions are fitted using the FITMC package to obtain analytic expressions which are used in the electric field calculation. As described in Chapter 4, there are still some assumptions in the sense that a radial symmetry is assumed in the shower front, and the particle distributions are averaged over the

development of the air shower. The developments of the air shower model over time are given in Table 1.1 a).
In Chapter 2 and Chapter 4, methods are given to distinguish between different primary particles. It should however be noted that this is not possible on a shower-to-shower basis. The main difference for primaries of different mass is the position in the atmosphere where the electronic component of the shower is maximal. The used measure is defined by the depth $X_{max}(g/cm^2)$ the shower has reached at its maximum. Due to statistical fluctuations the shower maximum for different primaries will differ on average, but for individual showers they may overlap. Therefore, even though it is be possible to determine the position of the air shower maximum, the primary particle can only be determined on a statistical basis.

1.5.2 The emission mechanisms

At the starting point of this thesis in 2008, the emission mechanisms were not clear from the theoretical point of view. Where the most known and used REAS [61] code was based on geosynchrotron emission predicting uni-polar pulses, the MGMR code described in [62] was based on the macroscopic transverse currents induced by the Lorentz force acting on the charged leptons in the shower front predicting bi-polar pulses. The strength of the geomagnetic component scales with the induced drift velocity v_d of the charged leptons in the shower front. In the original version of MGMR in 2008, the drift velocity was derived to be $v_d = 0.04 \cdot c$. In Chapter 2, the more realistic value $v_d = 0.025 \cdot c$ is used as obtained from [73]. For EVA simulations, the drift velocity is obtained directly from Monte-Carlo simulations.
As shown in Chapter 2, from the macroscopic point of view there is a secondary emission mechanism due to a net excess charge in the shower front which was already predicted by Askaryan in 1962 [44]. The fraction of charge excess in the shower front $C_x = 0.23$ is taken to be constant for MGMR simulations, where for EVA simulations this fraction is obtained from Monte-Carlo simulations. The induced polarization by the two emission mechanisms is discussed in Chapter 2, and it follows that the different polarization patterns and their interference can be used to disentangle the charge-excess emission and the geomagnetic emission.
As described in Chapter 3, after the inclusion of a missing radiation component due to the start and end-points of the particle tracks in the microscopic REAS3 model, the main differences between REAS3 and MGMR were overcome. At this point both models predicted bi-polar pulses of

similar strength, and also the polarization of the radio signal was shown to be similar. With this convergence, the main emission mechanisms are considered to be understood.
In Chapter 5, the different polarization patterns of the geomagnetic emission and the charge-excess emission are used to see if the charge-excess emission can be observed in data. This is done for measurements at the Pierre Auger Observatory [53, 54, 55, 56], and for the first time in nature a clear signature of the charge-excess in the air shower is observed. The emission mechanisms and the parameters determining their strength are given in Table 1.1 b).

1.5.3 The atmosphere

On first hand, one would expect the atmosphere to only influence the air shower development. Nevertheless, already before the starting point of this thesis it was shown in [73] that event though the deviation of the index of refraction from unity is small ($O(10^{-4})$), this small deviation might already lead to Cherenkov effects in the emission.
The simulations described in Chapters 2 and 3 for both MGMR and REAS are done for an index of refraction equal to unity. The main function of the atmosphere is to obtain a proper description of the air shower development. Where MGMR uses an exponential model for the atmosphere, REAS3 uses a layered atmosphere. The differences for the air shower development are however negligible.
In Chapter 4, the inclusion of a realistic index of refraction following the law of Gladstone and Dale, depending on the atmosphere is discussed. It is shown that the small deviation of the index of refraction from unity has a huge effect on the predicted emission. Cherenkov effects in the form of very sharp pulses containing extremely high frequency components are observed at intermediate distances from the shower axis, $50 - 400$ m, depending on zenith angle. Since this is a geometry effect, the emission mechanisms do not alter. The consequences and applications of these Cherenkov effects are discussed in the final parts of Chapter 4. Where previously the emission was seen at relatively low frequencies < 100 MHz, for a realistic index of refraction emission is predicted in the GHz regime due to Cherenkov effects. Furthermore, the signal strength as a function of distance to the shower axis is not a monotonously decreasing function any more, but contains a peak which can be linked to the position of the air shower maximum. The atmosphere and index of refraction used by the different simulations are given in Table 1.1 c).

Table 1.1: Historical development of the MGMR-based models. a) The air shower model and extracted shower parameters that lie at the basis of the original MGMR [62], MGMR as expanded in Chapter 2, and the EVA model given in Chapter 4. The shower profile is denoted by $N(t')$, the lateral particle distribution in the shower front as $w_1(r)$, and the longitudinal particle distribution in the shower front by $w_2(r,h);f_p(h)$. b) The emission mechanisms included into the simulation. The geomagnetically induced drift velocity v_d is given as well as the charge-excess fraction C_x. c) The refractive index n, and the atmosphere model used for the different simulations.

	MGMR(2008 [62])	MGMR (Ch. 2, 2012)	EVA (Ch. 4, 2012)
a) Air Shower:			
$N_e(t_r)$	Parameterized	Hybrid	Monte Carlo
$w_1(r)$	$\delta(r)$	$\delta(r)$	Monte Carlo
$w_2(r,h);f_p(h)$	Parameterized	Parameterized	Monte Carlo
Thickness	$L = 10$ m	$L = 3.9$ m	
b) Emission Mechanisms:			
Geomagnetic	Yes	Yes	Yes
Drift velocity	$v_d = 0.04 \cdot c$	$v_d = 0.025 \cdot c$	Monte Carlo
Charge excess	No	Yes	Yes
Fraction		$C_x = 0.23$	Monte Carlo
Dipole	Yes	Yes	No
c) Atmosphere:			
Atmosphere model	Exponential	Exponential	Layered
Refractive index	$n = 1$	$n = 1$	$n = n_{GD}$

Chapter 2

Macroscopic Geo-Magnetic Radiation model

This chapter is an adapted version of the article published in Astroparticle Physics, 34, 267 (2010):

The Lateral Distribution Function of Coherent Radio Emission from Extensive Air Showers; Determining the Chemical Composition of Cosmic Rays

Krijn D. de Vries[1], Ad M. van den Berg[1], Olaf Scholten[1], and Klaus Werner[2].
[1] Kernfysisch Versneller Instituut, University of Groningen, 9747 AA, Groningen, The Netherlands
[2] SUBATECH, University of Nantes – IN2P3/CNRS– EMN, Nantes, France.

2.1 Abstract

In this chapter we introduce the MGMR model as given in [62]. All calculations are done for an index of refraction equal to its vacuum value of unity. Furthermore, the lateral particle distribution in the air shower front is neglected. A new expression is derived to calculate the coherent radio pulse at small distances from the shower axis. It is shown that for small distances to the shower axis the shape of the electric pulse is determined by the 'pancake' function, describing the longitudinal distribution of charged particles within the shower front, while for large distances the pulse is determined by the shower profile. This reflects in a different scaling of the lateral distribution function (LDF) at small and at large distances. As a first application we calculate the LDF for proton- and iron-induced showers and we show that this offers a very sensitive measure to discriminate between these two. Even though the LDF changes significantly for a realistic index of refraction as is discussed in Chapter 4, the shown method and physics to determine the position of the air shower maximum are very similar. Furthermore, we show that due to interference between the geomagnetic and the charge-excess contributions the intensity pattern of the radiation is not circular symmetric.

2.2 Introduction

In the early 21st century much progress has been made modeling electric pulses initiated by extensive air showers (EAS) [62, 74, 73]. One of the reasons for this progress are the results from the LOPES [49, 50] and CODALEMA [51, 52] experiments. Both experiments indicate that the dominant emission mechanism is due to induction effects from Earth's magnetic field which exerts a Lorentz force on the charged particles in the shower. The emission process can be described in a microscopic model where the individual electrons and positrons move on cyclotron orbits [59, 60, 61, 74]. The importance of coherent radio emission was already noted in earlier research on radio emission from air showers [39, 41, 45, 75]. This approach has received renewed attention with the realistic calculations in the Macroscopic Geo-Magnetic Radiation (MGMR) model as presented in Ref. [62]. The experimental results have triggered plans for an extensive array of radio detectors at the Pierre Auger Observatory [53, 54, 55]. A clear theoretical understanding of the pulse shape and its dependence on the distance from the shower axis is therefore of importance. In this chapter we derive a new expression for the electromagnetic pulse that is more appropriate for

observer positions that are closer to the shower axis while the expression derived in Ref. [62] is appropriate for large distances. This allows us to address quantitatively the differences in the structure of the electromagnetic pulse emitted by the EAS at large and small distances. It was already noticed in an earlier study [62] that in a macroscopic calculation the structure of the electromagnetic pulse at small distances is strongly affected by the distribution of the particles in the shower front (the pancake). In Ref. [76] the importance of length scales was emphasized in the understanding of macroscopic geo-magnetic radiation from the EAS indicating that the physics at short distances differs from that at large distances.
In Ref. [74] it is argued that in the synchrotron-emission model REAS2, the lateral distribution function (LDF) can be used to disentangle the chemical composition of cosmic rays. As shown in Ref. [77] the predictions of the macroscopic model and the synchrotron-emission models such as used in Refs. [74, 78, 79] differ greatly. In particular the latter models predict a unipolar pulse which contradicts the fact that the intensity of the emitted radiation should vanish at the longest wavelength [76], a condition that is satisfied by the bi-polar pulse in the MGMR model. In [64, 80], it has been shown that this is due to the omission of the bremsstrahlung contributions at the beginning and the end of the particle trajectories in the synchrotron-emission models as will be discussed in the following chapter. As an application of the new calculation scheme for the MGMR model, we will investigate the differences in the LDF for iron- and proton-induced showers.
In Section 2.3 a quick overview of the MGMR model is given. For completeness we will shortly review the derivation of the expression for the electric field. As the next step we concentrate on the short distance scales in Section 2.4 where a new expression is derived for the electric field at small impact parameters. For simplicity, we will limit ourselves to vertical incoming air showers. The geometry considered is an incoming shower with velocity $\vec{\beta} = -\beta\hat{z}$, an observer placed at a distance $\vec{d} = d\hat{x}$ from the shower axis with a magnetic field $\vec{B} = B\hat{y}$ perpendicular to the air shower. As a first application of the new calculation scheme it is shown in Section 2.5 that the LDF depends on the orientation of the observer with respect to the shower axis. This angular dependence is due to interference of the leading magnetic contribution with secondary contributions. Of these secondary contributions, the one which is generated by charge excess in the shower is the most important. As a second application the influence of the chemical composition of the cosmic ray on the LDF is discussed in Sections 2.6 and 2.7.

2.3 The model

When an ultra-high-energy cosmic ray collides in the atmosphere, a cascade of secondary particles is created, moving towards Earth with a velocity close to that of the speed of light. This can be visualized by a 'pancake' of particles. The basic picture in the MGMR model [62] is that the charged particles in the pancake, mostly electrons and positrons, will be deflected in Earth's magnetic field causing the flow of a macroscopic electric current. The strength of this electric current is time dependent and will thus radiate. We will temporarily make the assumption that there is an equal amount of electrons and positrons in the shower; in a later section the effects of charge excess will be discussed.
The total amount of electrons and positrons traveling in the shower front can be described as a function of height $z = -c\beta_s t' + h$, where t' is the shower time (negative) and the front of the shower hits Earth at $t' = 0$. This implies that the front of the shower is located at a height of $z = -c\beta_s t'$ with the particles lagging behind at a distance h within the pancake following a distribution $f_p(h)$. The distribution of particles is parameterized as

$$N(z, t') = N_e f_t(t')\, f_p(h) \tag{2.1}$$

where $f_t(t')$ is the normalized shower profile, and the total number of particles at the shower maximum equals $N_e = 6 \times (E_p/10^{10}\text{eV})$ defined by the maximum number of particles for a 10^{19} eV shower [81].
The longitudinal profile $N_e f_t(t')$ is parametrized [82] as a function of the penetration depth X in units of g cm^{-2},

$$N_e f_t(t) = N_e e^{(X - X_{max} - 1.5X \ln s)/X_0} \ . \tag{2.2}$$

The penetration depth is written as a function of height as $X(z) = (\rho(0)/C)\, e^{-Cz_s}$. Using $\rho(0) \approx 1168$ g m^{-3}, and $X(0) \approx 1000$ g cm^{-2} gives $C = 1.168{\cdot}10^{-4}$ m^{-1}. The parameter X_{max} is taken to reproduce the shower maximum from simulations [81], $X_{max} = (840 + 70 \log_{10}(E_p/10^{20}\text{ eV}))$ g cm^{-2}. The shower age $s(X)$ can be parameterized as [82],

$$s(X) = \frac{3X/X_0}{X/X_0 + 2X_{max}/X_0}, \tag{2.3}$$

where $X_0 = 36.7$ g cm^{-2} is the radiation length of electrons in air.
For the pancake thickness a parametrization can be made using measured arrival time distributions. This can be fitted using a Γ-probability distribution function (Γ-pdf) [82, 83],

$$f_p(h) = h^{\beta} e^{-2h/L} \times (4/L^2), \tag{2.4}$$

where $\beta = 1$ and $L = 3.9\,\mathrm{m}$ have been used, see Section 2.6.
The electrons and positrons will be deflected in Earth's magnetic field which macroscopically induces a net current in the $\hat{x}$ direction given by,

$$j^x(x, y, z, t') = \langle v_d q \rangle \, e \, N(z, t') \delta(x) \delta(y) \; , \tag{2.5}$$

where q is the sign of the electric charge e. We disregard the lateral distribution of the charged particles and fix the position of the charged particles at the shower axis. The drift velocity, $\langle v_d q \rangle$, depends rather strongly on the model assumptions made and we adopt a value of $\langle v_d q \rangle = 0.025\ c$ following the geometry given in [73].
The vector potential is given by the Liénard-Wiechert fields [84] in terms of the current density Eq. (2.5),

$$A^x(t, \vec{d}) = J_0 \int \frac{f_t(t_r) f_p(h)}{\mathcal{D}} \, dh \; , \tag{2.6}$$

where $J_0 = \langle v_d q \rangle N_e e / \left[4\pi\varepsilon_0 c\right]$, d is the distance from the observer to the shower axis, and where the retarded distance can be rewritten as

$$\mathcal{D} = \sqrt{(-c\beta_s t + h)^2 + (1 - n^2\beta_s^2) d^2} \; . \tag{2.7}$$

The retarded time is defined by $c(t - t_r)/n = R$, where $R = \sqrt{(z^2 + d^2)}$, n is the index of refraction of air and can be expressed as [62, 73],

$$ct_r = \frac{ct - n^2\beta_s h - n\mathcal{D}}{(1 - n^2\beta_s^2)} \; . \tag{2.8}$$

At a large distance from the shower axis the point-like approximation [62, 77] is valid in which the pancake thickness is set to zero, $f_p(h) = \delta(h)$. In this limit a simple analytical expression for the electric field can be derived [62],

$$E_x(t, \vec{d}) \approx J_0 \frac{c^2 t_r^2 4}{d^4} \frac{d}{dt_r} [t_r f_t(t_r)] \; , \tag{2.9}$$

with $ct_r \approx -d^2/2ct$. In general this approximation is valid at distances above $d = 500\,\mathrm{m}$ since the typical time window for the pulse lies between 10^{-8} and 10^{-7} s. From Eq. (2.9) we see that the electric field scales as d^{-4} and that the integral over time vanishes (i.e. zero response at zero frequency) when the shower profile vanishes at Earth's surface.

2.4 Radial dependence of the pulse strength

For the shape of the pulse it is very important to understand the interplay between the different length scales [76]. While at large distances from the shower the important length scale is related to a projection of the shower profile along the line of sight of the observer, we will show in this section that for small distances the pancake thickness parameter, L, is important. To describe the electric field for small impact parameters we encounter the problem that the integral in Eq. (2.6) becomes numerically unstable. We therefore first derive a new equation for the pulse which is particularly suited for small distances from the core.

For an observer placed close to the shower axis it is more transparent to change variables in Eq. (2.6) and integrate over the retarded shower time at which the signal is emitted since the signal moves with the same velocity as the shower. The vector potential can thus be written as,

$$\begin{aligned} A^x(t,\vec{d}) &= J_0 \int\limits_{t_r^-(t)}^{t_r^+(t)} dt_r \frac{\partial h}{\partial(ct_r)} \frac{f_t(t_r)}{\mathcal{D}} f_p(h) \\ &= -J_0 \int\limits_{t_r^-(t)}^{t_r^+(t)} dt_r \frac{f_t(t_r)}{z} f_p(h) \ . \end{aligned} \tag{2.10}$$

The retarded time t_r is related to the observing time t and the distance from the shower front h by Eq. (2.8) which can be rewritten in the limit $n = 1$ and $\beta_s = 1$ as

$$ct_r = \frac{c^2t^2 - d^2 - h^2}{2(ct + h)} \ , \tag{2.11}$$

The Jacobian in this case is non-zero due to the fact that at a fixed observer time t, the received signal is emitted at different shower times, depending on the emission point within the pancake. Hence, $t_r^- = -\infty$ and $t_r^+ = t_r(t, h = 0)$ for a fixed observer time t. The Jacobian can now be derived from Eq. (2.11),

$$\frac{\partial h}{\partial(ct_r)} = \frac{\mathcal{D}}{ct_r - h} \tag{2.12}$$

Making use of the fact that the terms coming from the derivative working on the integration limits and the partial integration vanish since f_p vanishes

at the limits, the electric field can now be expressed as

$$\begin{aligned} E^x(t,\vec{d}) &= -J_0 \int_{t_r^-(t)}^{t_r^+(t)} dt_r f_t(t_r) \frac{d}{dt}\left(\frac{f_p(h)}{z}\right) \\ &= -J_0 \int_{t_r^-(t)}^{t_r^+(t)} dt_r f_t(t_r) \left(\frac{d}{dt}+\frac{d}{dt_r}\right)\left(\frac{f_p(h)}{z}\right) \\ &- J_0 \int_{t_r^-(t)}^{t_r^+(t)} dt_r \frac{df_t(t_r)}{dt_r}\frac{f_p(h)}{z} \\ &- \left.\frac{f_t(t_r)f_p(h)}{z}\right|_{t_r^-(t)}^{t_r^+(t)}. \end{aligned} \tag{2.13}$$

Using

$$\left(\frac{d}{dt}+\frac{d}{dt_r}\right)\left(\frac{f_p(h)}{z}\right) = \frac{\beta}{z}\frac{df_p(h)}{dh}, \tag{2.14}$$

we can write

$$\begin{aligned} E^x(t,\vec{d}) &= -J_0 \int_{t_r^-(t)}^{t_r^+(t)} dt_r f_t(t_r) \frac{\beta}{z}\frac{df_p(h)}{dh} \\ &- J_0 \int_{t_r^-(t)}^{t_r^+(t)} dt_r \frac{df_t(t_r)}{dt_r}\frac{f_p(h)}{z}, \end{aligned} \tag{2.15}$$

where t, t_r and h are related by Eq. (2.8). For very small impact parameters the second term on the right-hand side in Eq. (2.15) becomes an integral over the time derivative of the shower profile which vanishes at the given limits. This happens since the signal travels along with the shower and thus h becomes approximately independent of t_r. Hence the main contribution to the electric field for very small impact parameters comes from the first term on the right-hand side of equation Eq. (2.15).
When the shower profile is finite at the surface of Earth, $z = 0$, the terms in Eq. (2.15) suffer from a $1/z$ divergence. To regularize this divergence we introduce an exponential suppression term in the shower profile function,

$$F_t(t_r) = f_t(t_r) - f_t(0)e^{-z/a}, \tag{2.16}$$

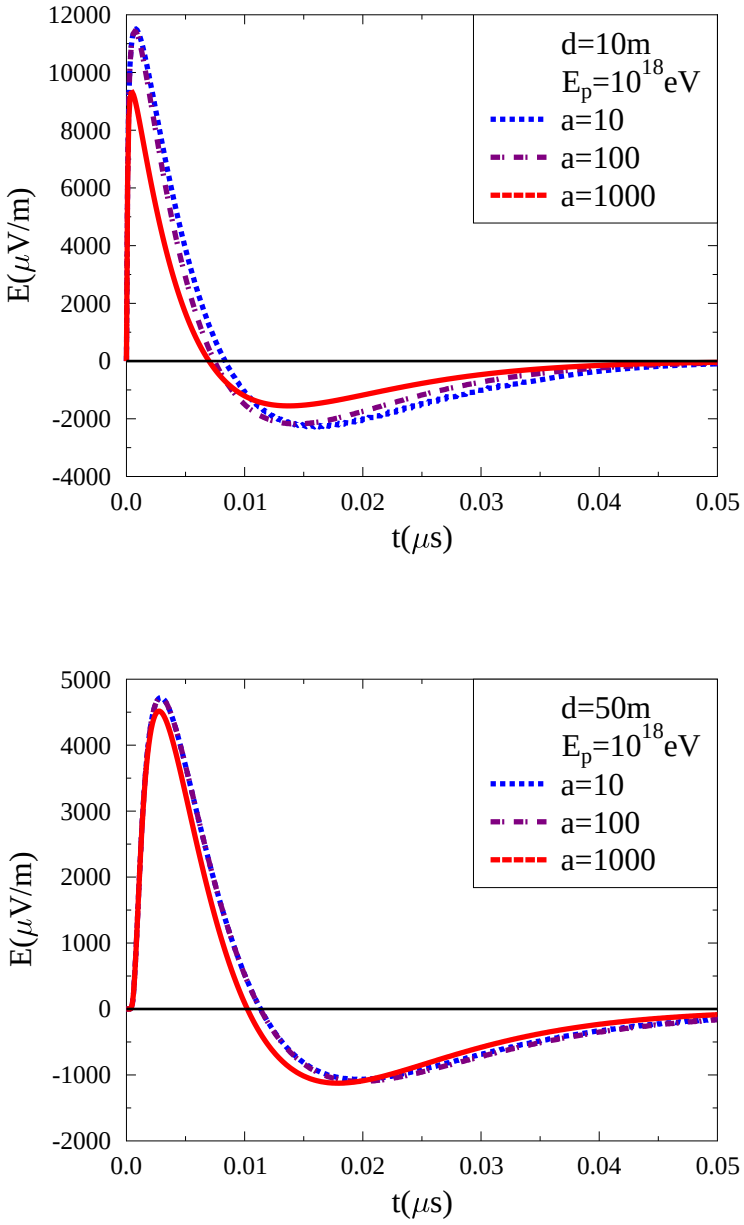

Figure 2.1: The unfiltered electric field for different values of the cut-off parameter $a = 10$, $a = 100$, and $a = 1000$, at a distance $d = 10\,\mathrm{m}$ (top) and $d = 50\,\mathrm{m}$ (bottom) from the shower axis. The pancake thickness parameter is taken as $L = 3.9$; see Section 2.6.

where a is the cut-off distance. The divergence in Eq. (2.15) is now eliminated since the shower profile function vanishes linearly for $z = 0$. The electric field for different values of a is given in Fig. 2.1 where the simulations are done for a vertical incoming shower with a primary energy of $E_p = 10^{18}\,\mathrm{eV}$. The calculations show that at a distance of $d = 50\,\mathrm{m}$ even a

value as large as $a = 1000\,\mathrm{m}$ hardly affects the pulse. At a distance of only $d = 10\,\mathrm{m}$ a value of $a = 100\,\mathrm{m}$ gives already a stable result. It has been verified that this result hardly depends on the altitude of the observer or energy of the cosmic ray, and can also be used for more energetic showers where the shower maximum is close to Earth's surface. This is due to the fact that the maximum of the observed electric field is emitted well before the shower is fully developed. We note here that, therefore the observation of radio signals from air showers are particularly suited to study the early stages of the shower development. Interesting to notice is that the signal at a distance of only 50 m from the core is hardly affected by the shower properties at a height below 1 km.

Another interesting aspect of Fig. 2.1 is that the pulse-shape does not vary strongly with distance. At large distances where Eq. (2.9) applies one expects a variation like d^2 in pulse length. Instead one finds that the zero-crossing of the pulse changes from 9 to 11 ns while the distance changes by a factor 5 from $d = 10$ to 50 m. This time scale corresponds to a length scale of about 3 m which is determined by the pancake thickness as supported by test calculations.

The dependence of the calculated pulse height on d is shown in Fig. 2.2. Based on Eq. (2.9) one would expect the pulse strength to be proportional to d^{-4} as given by the black line in the figure. Only at very large distances this dependence is seen.

In Fig. 2.3 the power P above 25 MHz divided by that at a distance of $d = 50$ m is plotted as a function of d. This quantity can easily be compared to actual measurements since the power is not affected by dispersion of the signal contrary to the pulse height and it corresponds to a semi-realistic filtering of the pulse. It is clearly seen that for small distances a smaller value of a should be used to reach a convergent result. The LDF for the power shows a distinct exponential structure for distances beyond 5 m from the core where the power drops by one order of magnitude over a distance of close to 70 m.

For observer distances approaching $d = 0$ m the pulse height tends to diverge. Since, for $n = 1$, the signal travels along with the shower with the same speed, an observer placed at the impact point of the shower will see the equivalent of a divergent Cherenkov peak. The precise structure of the pulse at very short distances will thus strongly depend on the index of refraction [73]. In addition one expects that at close proximity to the core the electric field is influenced by the lateral extent of the electrons in the shower since the particle density is strongly peaked near the shower axis. In Chapter 4 we will look into this effect in more detail.

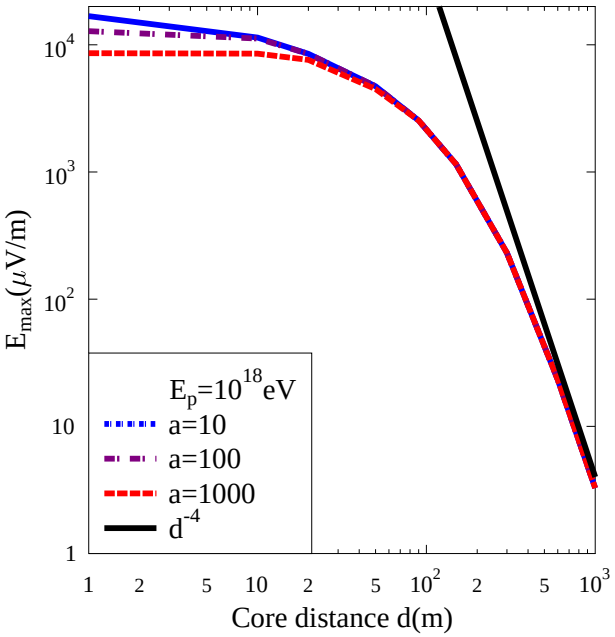

Figure 2.2: Lateral distribution function for the pulse height as function of distance on double logarithmic scale for different values of the cut-off parameter a.

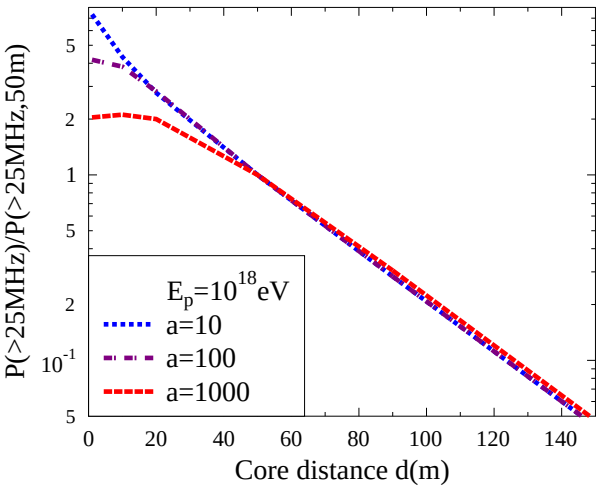

Figure 2.3: Lateral distribution function for the received power at frequencies above 25 MHz divided by that at a distance of $d = 50$ m.

2.5 Interference

The main secondary contribution, which is important for the present discussion, is due to the charge excess in the shower [62, 73] which is due to

compton scattering and the knock out of energetic electrons from ambient air molecules. The coherent emission from the charge excess in cosmic-ray induced showers was first discussed by Askaryan [44]. Even though the Askaryan effect is often associated with Cherenkov radiation, it also applies to the case in which the index of refraction is unity [85].
Macroscopically the charge-excess contribution can be described using a net negative charge moving with the speed of light toward Earth's surface. The contribution to the vector potential is now given by,

$$\begin{aligned} A^0_{Cx} &= \frac{eN_e}{4\pi\epsilon_0} C_x \int_0^\infty dh \frac{f_t(t_r) f_p(h)}{\mathcal{D}} \\ &- \frac{e}{4\pi\epsilon_0} \int_{-\infty}^{t'} \left(\int_0^\infty dh \frac{df_t(t')}{dt'} \frac{f_p(h)}{R} \right) dt' \qquad (2.17) \\ A^z_{Cx} &= \frac{eN_e}{4\pi\epsilon_0} C_x \int_0^\infty dh \frac{-\beta f_t(t_r) f_p(h)}{\mathcal{D}}. \qquad (2.18) \end{aligned}$$

The electric field is now obtained by,

$$\begin{aligned} E^{Cx}_x(t) &= \frac{-\partial A^0_{Cx}}{\partial x} \\ &= \frac{C_x e N_e}{4\pi\epsilon_0} \int_0^\infty dh \frac{x}{\mathcal{D}^2} \frac{z}{R} \dot{f}_t(t_r) f_p(h) \qquad (2.19) \\ E^{Cy}_y(t) &= \frac{-\partial A^0_{Cx}}{\partial y} \\ &= \frac{C_x e N_e}{4\pi\epsilon_0} \int_0^\infty dh \frac{y}{\mathcal{D}^2} \frac{z}{R} \dot{f}_t(t_r) f_p(h) \qquad (2.20) \\ E^{Cx}_z(t) &= \frac{-\partial A^0_{Cx}}{\partial z} - \frac{\partial A^z_{Cx}}{\partial ct} \\ &= \frac{C_x e N_e}{4\pi\epsilon_0} \int_0^\infty dh \frac{d}{\mathcal{D}^2} \frac{d}{R} \dot{f}_t(t_r) f_p(h) \qquad (2.21) \end{aligned}$$

where $C_x = 0.23$ is the approximate fraction of charge excess with respect to the total number of electrons and positrons in the shower as predicted by the Monte-Carlo simulations described in Section 2.6.

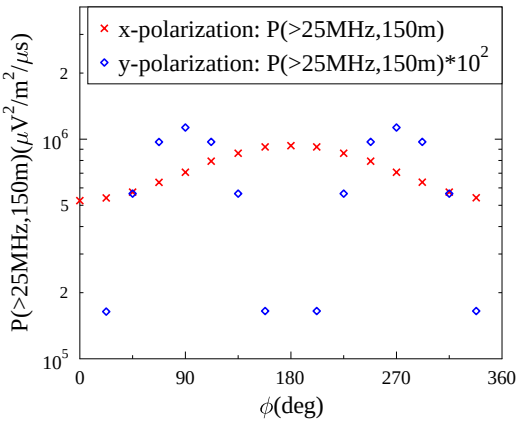

Figure 2.4: The strength of the signal for two different polarization directions is plotted as a function of the orientation of the observer with respect to the shower. The y-polarization has been multiplied by a factor 100 to put it on a similar scale. The magnetic field is chosen pointing to the North, while $\phi = 90°$ ($\phi = 180°$) corresponds to the observer at the East (North) side of the shower.

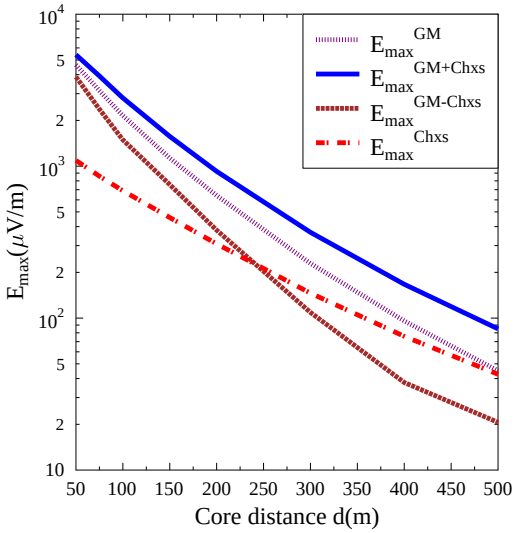

Figure 2.5: The behavior of the LDF as a consequence of different types of interference between geo-magnetic radiation and charge-excess radiation.

The interference of the geo-magnetic and the charge-excess contribution will be important for the observed pulse. For this interference the polarization direction of the two contributions should be considered. For a vertical shower ($\hat{z}$-direction) in a horizontal magnetic field ($\hat{y}$-direction) the

electric pulse generated by the induced electric current is polarized in the $\hat{x}$-direction independent of the orientation of the observer with respect to the shower axis. The radiation due to charge excess is polarized radially. Depending on the position of the observer the two contributions may interfere destructively (observer on the negative x-axis, $y = 0$), constructively (observer on the positive x-axis, $y = 0$), or be orthogonal (observer anywhere on the y-axis). This effect can be seen clearly in Fig. 2.4 where the dependence of the signal strength in the $\hat{x}$-, and $\hat{y}$-direction is plotted as function of the orientation of the observer with respect to the shower core. In Fig. 2.5 the LDF is shown separately for geo-magnetic and charge-excess radiation showing that while the two contributions differ by a factor 5 near the shower core, their magnitudes are about equal at a distance of 500 m. Depending on the orientation (azimuth) of the observer with respect to the shower the two contributions will interfere constructively or destructively. Since the charge-excess and the geo-magnetic contribution depend in a different way on the shower profile their LDF's differ. This gives rise to the interesting observation that for an observer at one side of the shower the charge-excess and the geo-magnetic contributions may interfere destructively resulting in a LDF that falls off rather steeply close to the core and flattens after the point of maximal destructive interference where even a local minimum could occur. For an observer positioned at the other side of the same shower the two contributions add constructively resulting in a relatively smooth LDF. In the perpendicular direction the two contributions will not interfere as their polarizations are orthogonal. The distance where a local minimum could occur and the LDF starts to flatten will depend on the relative magnitude of the charge-excess and the geo-magnetic contribution where the latter depends strongly on the angle of the shower with the magnetic field. It follows that one should be extremely careful in determining the LDF [86] since it is expected to depend on the orientation of the observer to the shower.

2.6 Hybrid approach

In the previous sections, all simulations were done using the basic MGMR model. The particle distributions in these simulations were parametrized using the analytical formula given in Section 2.3. In the current section we will discuss the hybrid approach to the MGMR model. Within this hybrid approach, the important macroscopic properties describing the electric field, such as the pancake thickness and the shower profile, are obtained from Monte-Carlo simulations.

These simulations are done using CX-MC-GEO which is part of the EVA package [70] that will be discussed in detail in Chapter 4. The CX-MC-GEO package is based on the cascade mode of the CONEX [21, 22] air shower simulation program. This code has been modified to include the deviation of charged particles in Earth's magnetic field, which is discussed in detail in Appendix B of Ref. [73]. Within the EVA package an analysis tool has been written, giving a histogrammed output of the full three-dimensional and timing information of the currents and particle distributions within a user-defined region of the shower front which in the simplest case becomes an average of all particles over the complete shower front. These currents and particle distributions are discussed in detail in Chapter 4.

As a first example the histogrammed output obtained by CX-MC-GEO, which will be used in Section 2.7 to study the differences of the LDF for a proton- and an iron-primary particle, will be discussed. The simulations are done for 40 proton- and 40 iron-induced showers to extract the longitudinal shower profiles and the pancake thicknesses at energies of 10^{17} and 10^{18} eV. The obtained shower profiles are shown in Fig. 2.6. As is expected the shower-to-shower fluctuations are rather large for proton- and small for iron-induced showers. The intrinsic fluctuations of a few showers becomes large. These fluctuations are due to the applied thinning which was rather crude for these showers. The shower profile drops to zero at $870\,\mathrm{g\ cm^{-2}}$ where the shower hits Earth's surface according to the conditions at the site of the Pierre Auger Observatory.

In the previous section the importance of the charge-excess contribution and its impact on the LDF is shown. To make this more quantitative the fraction of excess electrons is plotted in Fig. 2.7 for Monte-Carlo simulations of 40 proton- and 40 iron-induced showers at an energy of 10^{17} eV. An analysis for 10^{18} eV showers gives similar results. The charge excess is slightly increasing with increasing shower depth. Near the shower maximum the charge excess is close to 23% of the total number of electrons and positrons which is the value we have assumed in all our calculations described in Section 2.5. The charge-excess field strength scales linearly with the charge-excess fraction. The shower-to-shower fluctuations thus have a relatively small effect. The larger fluctuations that are observed are due to the crude thinning settings for these showers.

The other important parameter for the radio-emission calculations is the pancake thickness parameter. The relevant parameter for this is the mean distance of the electrons behind the shower front, $\langle h \rangle$, the mean pancake thickness parameter. In Fig. 2.8 this quantity is plotted for the set of showers at 10^{17} eV. Again the fluctuations are considerably larger for protons

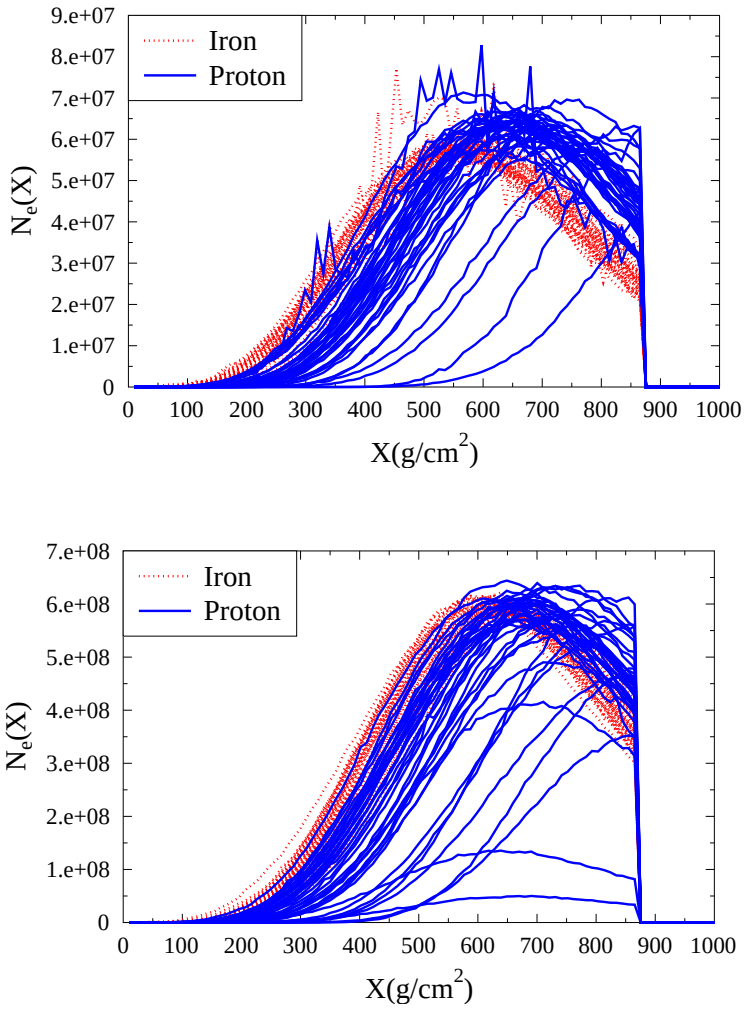

Figure 2.6: Total number of electrons and positrons as function of shower depth for 40 proton (blue curves) and 40 iron (red curves) initiated showers at energies $E = 10^{17}$ eV (top) and $E = 10^{18}$ eV (bottom).

than for iron. In addition one can see that the mean pancake thickness parameter is almost independent of shower height and of shower type. Calculations for showers for 10^{18} eV give similar results.

In the present calculations $L = \langle h \rangle$ has been fixed for the full shower development. From Fig. 2.8 it can be seen that $L = 4.3$ m is a reasonable average value for iron-induced air showers, and $L = 3.9$ m for proton-induced air showers. Where the width of the pancake function defined in Eq. (2.4) at $1/e$ of the maximum can be shown to be approximately $1.5L$. The fluctuations in the average value of L are small with respect to the fluctuations in the shower profiles and not considered in further analysis.

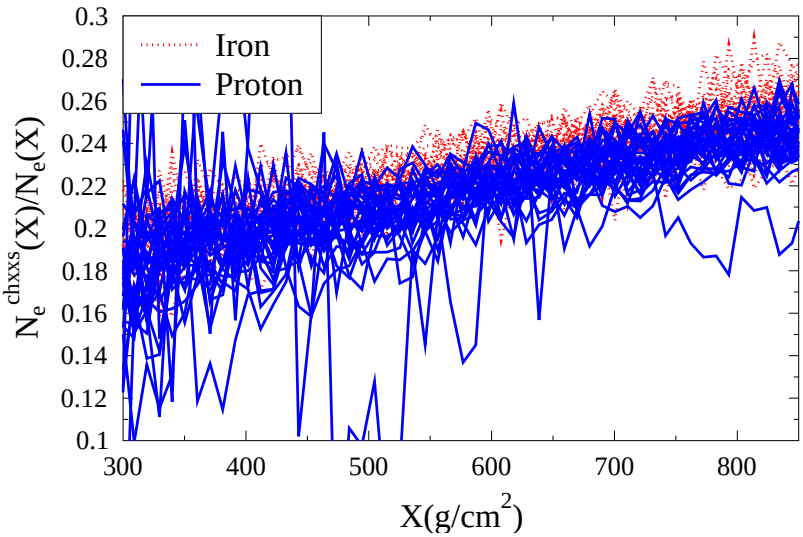

Figure 2.7: The fraction of charge-excess electrons with respect to the total number of electrons and positrons as a function of shower depth for 40 proton and 40 iron induced showers at an energy of 10^{17} eV.

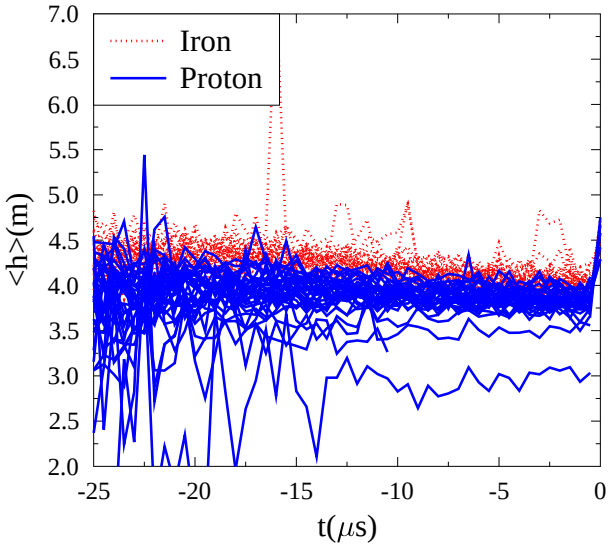

Figure 2.8: Mean distances of electrons behind the shower front for iron (red curves), and proton (blue curves) induced showers, as function of the negative shower time.

2.7 Composition

As a first application of the hybrid approach we study the LDF for proton- and iron-induced showers using MGMR in combination with CX-MC-GEO.

The smoothed shower profiles extracted from each Monte-Carlo simulation are used in the calculation of the radio signal. For the calculation at short distances we use a suppression coefficient of $a = 100$, since in Section 2.4 it is shown that this value gives reliable results at the distances considered here. The maximum of the field strength as function of distance is shown in Fig. 2.9. This is done for an observer placed on the x-axis where the charge-excess and geo-magnetic fields interfere constructively. This figure shows that the slope for iron-induced showers is less steep than for protons. One also sees that at a distance of $d = 100\,\mathrm{m}$ the calculated signal strength for iron and proton showers is almost the same. These features were also observed in REAS2 calculations [74].
To express the differences in the LDF more clearly we introduce a variable that is relatively easy to extract from data,

$$R^{25}_{50/300} = P(50, f > 25)/P(300, f > 25) \tag{2.22}$$

where $P(d, f > 25)$ is the power in the pulse for frequencies larger than 25 MHz at a distance d m from the shower core. In Fig. 2.10 the results of the calculations are displayed in a histogram. The averages of the values for iron- and proton-induced showers differ strongly, however due to shower-to-shower fluctuations some of the proton showers give rather similar values as for iron. The proton showers that give a similar value for $R^{25}_{50/300}$ are showers which have profiles (see Fig. 2.6) very similar to those of iron. At higher energies the average value of $R^{25}_{50/300}$ differs less between proton- and iron-induced showers. This is a direct consequence of the fact that X_{max}, the important parameter responsible for the observed effect, differs less for the different primary particles at higher energies, as can be seen in Fig. 2.6. As noted earlier, the LDF and thus also $R^{25}_{50/300}$, depends on the orientation of the observer with respect to the shower and comparisons should thus be made at the same azimuth with respect to the shower core. It has been checked that the qualitative differences between iron and protons remain as shown in Fig. 2.10 also for other azimuth positions of the observer. The reason for this is that the charge-excess fraction is similar for proton- and iron-induced showers.

2.8 Summary and conclusions

We have derived a new expression for the electric field emitted by an EAS at close proximity to the shower axis in the MGMR model. It differs from the expression used for the pulse strength at large distances by a change of integration variables. This change of variables expresses that at short

distances the pulse shape is determined by the pancake function and the shower profile can be integrated over. At large distances the picture is reversed and the pulse shape is determined by the shower profile where the pancake thickness is integrated over.
Due to the fact that the electron density is finite when the shower reaches Earth the pulse height becomes divergent at short distances from the core. This we have resolved by -artificially- suppressing the shower at small heights above Earth's surface. We show that this allows us to get accurate numerically-stable results at distances down to 30 m. At smaller distances other effects such as the lateral spread of the electrons in the shower, as well as shower-to-shower fluctuations will be important which are not included in the present schematic approach.
Since at short distances, the pulse shape is determined by the pancake function while at large distances it is governed by the shower profile this offers the possibility to use the LDF of the radio pulse to distinguish iron- and proton-induced showers. Before addressing this point we have added the radiation due to charge excess as the most important secondary process. It is shown that the determination of the polarization as a function of the azimuth angle can be used to study the different emission mechanisms of radio emission from an EAS. We have shown that the LDF is a very powerful tool to distinguish iron- and proton-induced showers although the effects of shower-to-shower fluctuations for protons can be large, where at the same time the power at a distance of 50 m from the shower core can be used as a measure for the energy.
All calculations in this chapter are performed for an index of refraction equal to its vacuum value of unity. In Chapter 4, it will be shown that for a realistic index of refraction Cherenkov effects play an important role in the radio emission. These Cherenkov effects also strongly influences the LDF. Nevertheless, as will be shown in Chapter 4 the applied method shown in this chapter still holds and can be used to determine the position of the shower maximum.

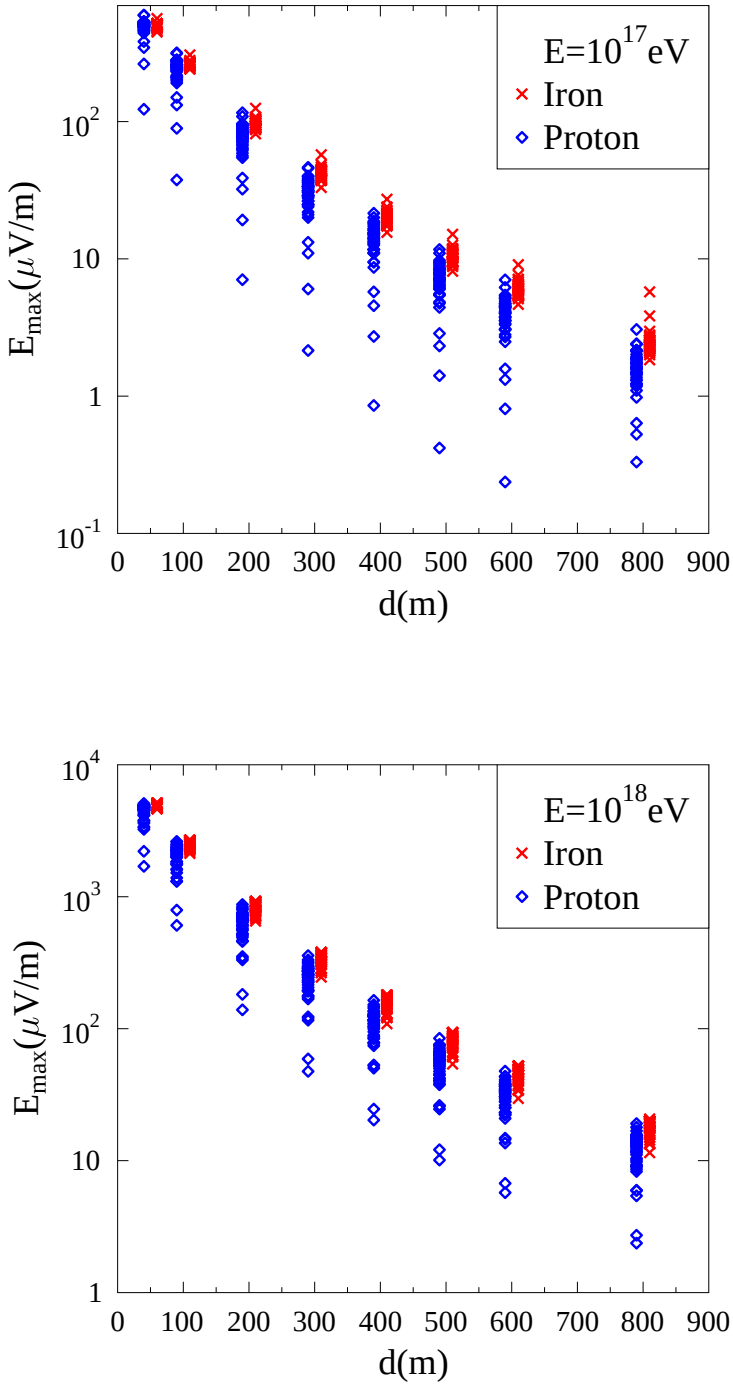

Figure 2.9: The LDFs are shown for proton (blue diamonds) and iron (red crosses) induced showers at an energy of 10^{17} eV (top), and 10^{18} eV (bottom), displayed in Fig. 2.6. The LDFs are given for an observer position leading to constructive interference between the charge-excess contribution and the contribution due to geo-magnetic radiation.

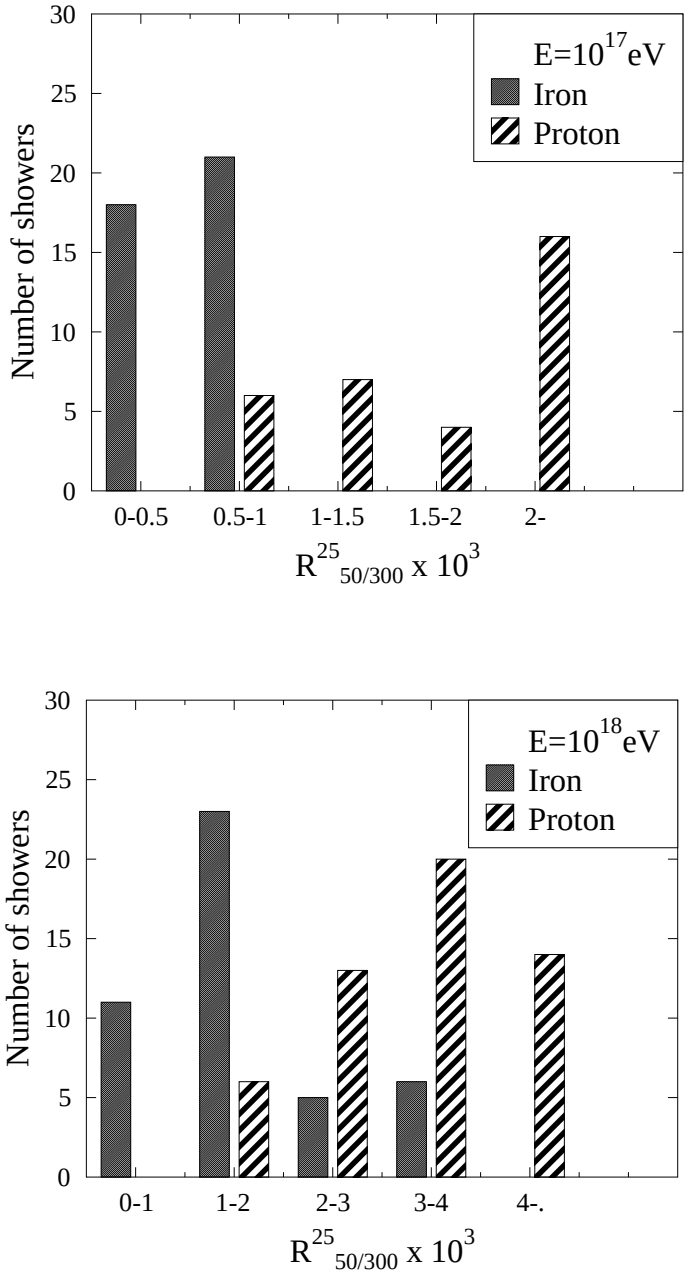

Figure 2.10: $R^{25}_{50/300}$, see text, for the 40 simulated proton and iron showers at an energy of $E = 10^{17}$ eV (top) and $E = 10^{18}$ eV (bottom).

Chapter 3

Microscopic vs. macroscopic modelling

Parts of this chapter have been published in the following articles:

A detailed comparison of REAS3 and MGMR simulations for radio emission from EAS.
arXiv:1202.3352
Marianne Ludwig[1], Tim Huege[2], Olaf Scholten[3] , Krijn D. de Vries[3].

The convergence of EAS radio emission models and a detailed comparison of REAS3 and MGMR simulations.
Nucl.Instrum.Meth. A662 (2012) S179-S186
Tim Huege[2] , Marianne Ludwig[1] , Olaf Scholten[3] , Krijn D. de Vries[3].

[1]*Institut für Experimentelle Kernphysik, Karlsruher Institut für Technologie - Campus Süd, 76128 Karlsruhe, Germany*
[2]*Institut für Kernphysik, Karlsruher Institut für Technologie - Campus Nord, Postfach 3640, 76021 Karlsruhe, Germany*
[3]*Kernfysisch Versneller Instituut, University of Groningen, 9747 AA, Groningen, The Netherlands*

3.1 Introduction

The existing and most used approach in the early days of MGMR was based on a microscopic approach modeling the geosynchrotron emission from charged leptons gyrating in Earth's magnetic field [82]. In the microscopic approach the total electric field is calculated by adding the emission from all leptons. Although both approaches are completely different, if the physics is described correctly a similar result should be obtained. Up to 2008 this was not the case. Where the microscopic models in the time domain predicted a unipolar pulse, the MGMR [62] model predicted a bipolar pulse. Also the magnitude of the electric field differed up to a factor ten. These differences were mainly due to a missing radiation component in the microscopic calculations [80]. By adding this missing radiation component a large part of the differences between MGMR and the microscopic models is overcome [64]. In this chapter, first an introduction to the microscopic approach is given and the missing radiation component is discussed. This chapter is concluded by giving a detailed comparison between MGMR and the microscopic approach of the REAS3 model, where the remaining differences are discussed.

3.2 The microscopic approach

In the REAS [82] code electromagnetic radiation is calculated by obtaining shower information and the particle tracks directly from the CORSIKA [20] air shower simulation program, which provides a full Monte Carlo simulation of the air shower. The REAS model has its basis in the electric field expressions as obtained from the Liénard-Wiechert potentials of classical electrodynamics,

$$\vec{E}(\vec{x},t) = e\left[\frac{\vec{n}-\vec{\beta}}{\gamma^2(1-\vec{\beta}\cdot\vec{n})^3R^2}\right]_{ret} \tag{3.1}$$

$$+ \frac{e}{c}\left[\frac{\vec{n}\times((\vec{n}-\vec{\beta})\times\dot{\vec{\beta}})}{(1-\vec{\beta}\cdot\vec{n})^3R}\right]_{ret}, \tag{3.2}$$

where $\vec{n}$ is the vector pointing from the emission point to the observer, $\dot{\vec{\beta}} = \dot{\vec{v}}/c$ the acceleration, $\gamma = \sqrt{1-\beta^2}$ the relativistic lorentz factor and R the distance from the emission point to the observer. The electric field is evaluated at the retarded emission time. In the first versions of REAS, REAS1 [82] and REAS2 [61], the continuous acceleration of the charges in

Earth's magnetic field was taken into account giving rise to synchrotron radiation. The result was a unipolar pulse that differed up to a factor of ten with the electric field as calculated by MGMR which is bipolar. As noted in [73], it was found that there was a missing radiation component due to the acceleration at the beginning and end-points of the particle tracks. In the latest REAS3 version [72] this contribution is included by means of the end-point formalism [87]. The corrected electric field expressions are given by,

$$\begin{aligned}\int \vec{E}(\vec{x},t)\mathrm{d}t &= \int_{t_1}^{t_2} \frac{e}{c}\left|\frac{\vec{n}\times[(\vec{n}-\vec{\beta})\times\dot{\vec{\beta}}]}{(1-\vec{\beta}\cdot\vec{n})^3 R}\right|_{ret} \mathrm{d}t = \vec{F}(t_2)-\vec{F}(t_1) \\ &= \frac{e}{cR}\left(\frac{\vec{n}\times(\vec{n}\times\vec{\beta}_2)}{(1-\vec{\beta}_2\cdot\vec{n})}\right) - \frac{e}{cR}\left(\frac{\vec{n}\times(\vec{n}\times\vec{\beta}_1)}{(1-\vec{\beta}_1\cdot\vec{n})}\right), \qquad (3.3)\end{aligned}$$

where the tracks of the individual particles are divided into small subsegments and the start and end-points are accounted for. For each start and end-point at the times t_1 and t_2, the electric field is now evaluated with the corresponding velocity vector $\vec{\beta}_1 = \vec{v}_1/c$ at the start of each subsegment of the particle track and $\vec{\beta}_2 = \vec{v}_2/c$ at the end of each subsegment of the particle track. The field is evaluated within the Fraunhofer approximation which implies that the distance R is taken constant along the track of the particle.

3.3 A detailed comparison between REAS3 and MGMR

Since the same physics should be described one expects REAS3 and the macroscopic approach as given by MGMR to give similar results. Therefore in this section we give a detailed comparison between both models. This is done for a set of predefined showers as given in Table 3.1. To get rid of shower-to-shower fluctuations from the Monte-Carlo approach of REAS3, the hybrid version of MGMR is used to read the shower profile as obtained from CORSIKA [20] which is the same as used in the REAS3 simulations. The other input parameters for MGMR are determined from Monte Carlo simulations discussed in the previous chapter and set to $v_d = 0.025 \cdot c$, $C_x = 0.23$, and $L = 3.9$ m.

Before looking at the actual comparison we first discuss the differences in the air shower models that still remain. The largest difference between both models is the treatment of the particle distributions in the shower front.

Table 3.1: Overview of the set of prototype air showers which were simulated for a detailed comparison between REAS3 and MGMR. An inclination of $-37°$ corresponds to the magnetic field geometry of the Pierre Auger Observatory. Note, that the azimuth angle is given in the coordinate system of CORSIKA, i.e. the inclined air shower is coming from south-east.

Energy	**Zenith, Azimuth**	**Strength of $\vec{B}$**	**Inclination of $\vec{B}$**
10^{17} eV	0°, 0°	0.23 Gauss	$-37°$
10^{18} eV	0°, 0°	0.23 Gauss	$-37°$
10^{19} eV	0°, 0°	0.23 Gauss	$-37°$
10^{17} eV	0°, 0°	0.23 Gauss	0° (horizontal)
10^{17} eV	0°, 0°	0.23 Gauss	90° (vertical)
10^{17} eV	0°, 0°	0.0 Gauss	-
10^{17} eV	50°, 45°	0.23 Gauss	$-37°$

Where REAS3 uses the histogrammed information as obtained directly from the CORSIKA air shower simulation, MGMR uses a parameterized shower front in which the lateral particle distribution is neglected and the longitudinal particle distribution follows the parameterization as given in Eq. (2.4), $f_p(h) = h^\beta e^{-2h/L} \times (4/L^2)$. Another more subtle difference is the atmosphere that is used, where REAS3 uses a similar atmosphere as in CORSIKA, the US standard atmosphere, MGMR uses an exponential given by,

$$X\,[h] = \frac{1000.0}{\cos\theta}\left(\frac{g}{cm^2}\right) \cdot \exp\left[\frac{\log(0.68)}{4000.0}\frac{h}{(m)}\right]. \tag{3.4}$$

3.3.1 Vertical air showers

We start the comparison by considering a vertical air shower at three different energies of 10^{17} eV, 10^{18} eV, and 10^{19} eV as given by the first three lines in Table 3.1. The observer position is chosen to be 200 m to the north of the impact point of the shower. Note that the magnetic field configuration is equal to the magnetic field at the AERA site of the Pierre Auger Observatory [56]. From Fig. 3.1, we see that the obtained electric field for both REAS3 and MGMR scales approximately linear with the energy of the primary particle $E \sim E_p^{0.96}$. This scaling with energy can be understood by the fact that the maximum number of charged particles at the shower maximum scales approximately like, $N_{max} = E_p/GeV$. Where the electric field for coherent emission scales with the total number of charged particles. Due to geometry effects, at larger primary energies the shower maximum lies closer to Earth's surface, the scaling is not perfectly linear.

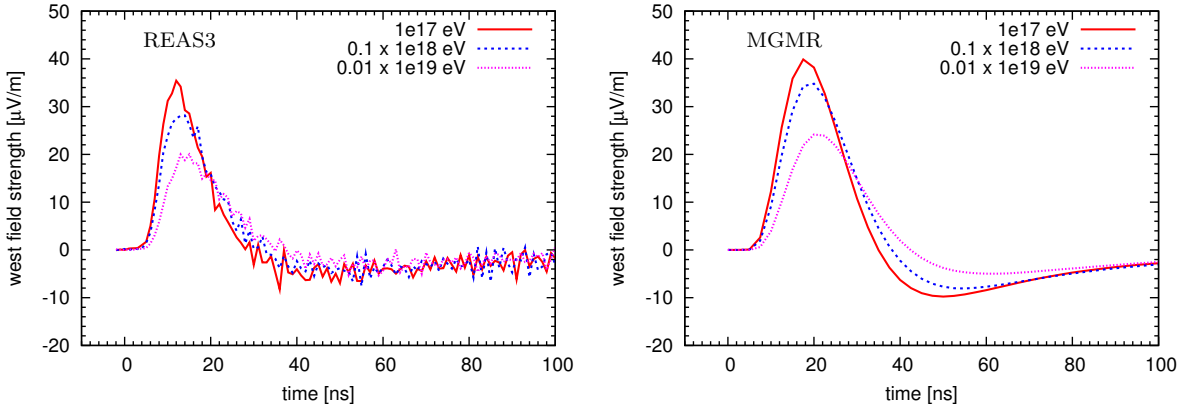

Figure 3.1: Comparison of the east-west polarization component emitted by vertical air showers with three different primary energies at an observer position 200 m north from the shower core: 10^{17} eV (solid red), 10^{18} eV (dashed blue) and 10^{19} eV (dotted magenta) for REAS3 (left) and MGMR (right). The pulse for 10^{18} eV is multiplied with 0.1 and for 10^{19} eV with 0.01 to allow a better comparison within the same plot. REAS3 and MGMR obtain similar results.

Furthermore, from Fig. 3.1 it is clear that both models agree in pulse shape and height within 10% for this specific simulation.
Since we only expect a scaling with energy, we will for the moment concentrate on the 10^{17} eV shower. In Fig. 3.2 we plot the east-west polarization of the electric field observed at different distances to the north of the impact point of the shower. For this specific geometry we thus consider only the geomagnetic emission which is polarized in the $-v \times B$ direction, which is east-west. From Fig. 3.2 it is evident that when going to larger observer distances both models converge, whereas for smaller observer distances the difference grows up to a factor of two. This can also be seen in Fig. 3.3, where for both models the frequency spectra at different impact parameters is given.
The charge-excess component is radially polarized and for an observer positioned to the north of the impact point this is the north-south direction. To show the interference between charge-excess emission and the geomagnetic emission we show the LDF of the maximum unfiltered field strength for different observer directions with respect to the impact point (north, east, south, and west) in Fig. 3.4. The interference with the charge-excess component is clearly visible for MGMR as well as REAS3. This can also be seen in Fig. 3.5 where the contour plot of the 60 MHz component is given for the different polarizations. The east-west polarization shows a clear asymmetry due to the interference of the geomagnetic radiation with the charge-excess emission. This pattern is visible for both REAS3 as well

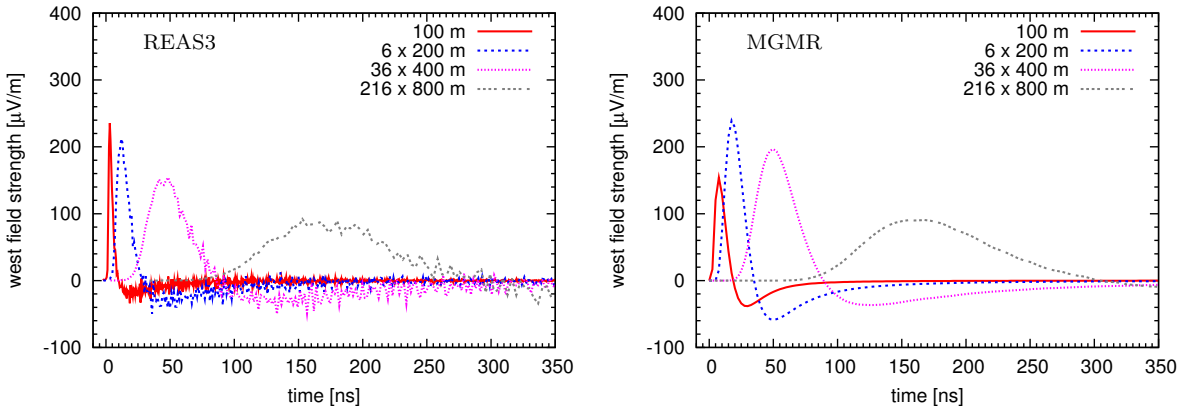

Figure 3.2: Comparison of the west polarization component emitted by a vertical air shower with a primary energy of 10^{17} eV for REAS3 (left) and MGMR (right). The figures show pulses for observers at different lateral distances to the shower core. With increasing distance, the results of both models converge.

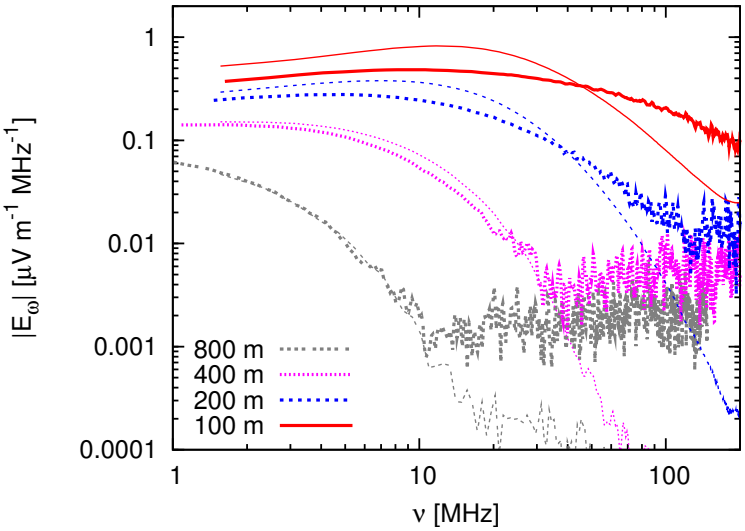

Figure 3.3: Comparison of the frequency spectra for REAS3 (thick lines) and MGMR (thin lines) for a vertical air shower with a primary energy of 10^{17} eV. The total spectral field strength is shown for observers at different lateral distances from 100 m up to 800 m.

as MGMR, nevertheless the asymmetry is stronger for MGMR than for REAS3. This difference can be understood from the underlying air shower model and will be discussed in Section 3.3.3. Since the geomagnetic radiation is fully polarized in the east-west direction, the north-south polarization is governed by the typical charge-excess pattern for both REAS3 and MGMR. An example of the interference is given in Fig. 3.6, where the raw electric field simulated with MGMR is shown for the four different ob-

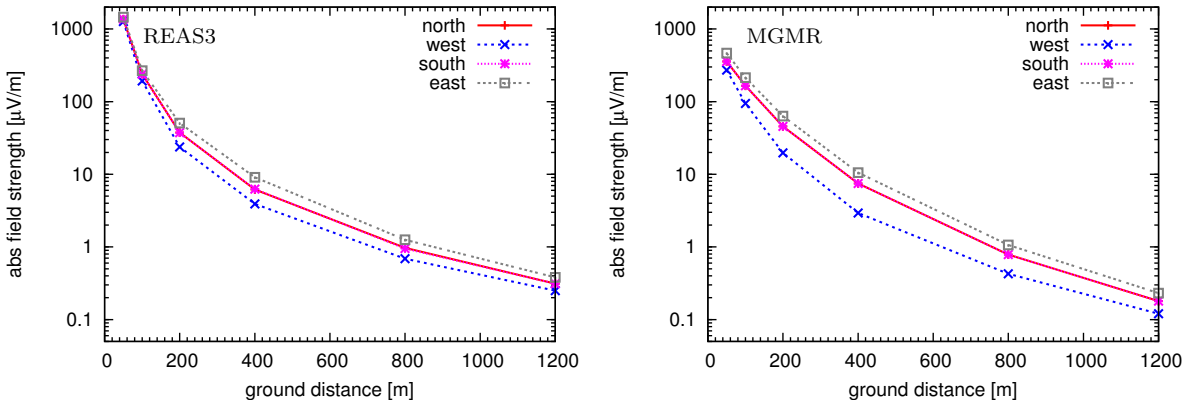

Figure 3.4: Comparison of the lateral dependences with full bandwidth amplitudes for a vertical air shower with a primary energy of 10^{17} eV predicted by REAS3 (left) and MGMR (right). The figures display the maximum absolute field strength at a given lateral distance of an observer to the shower axis.

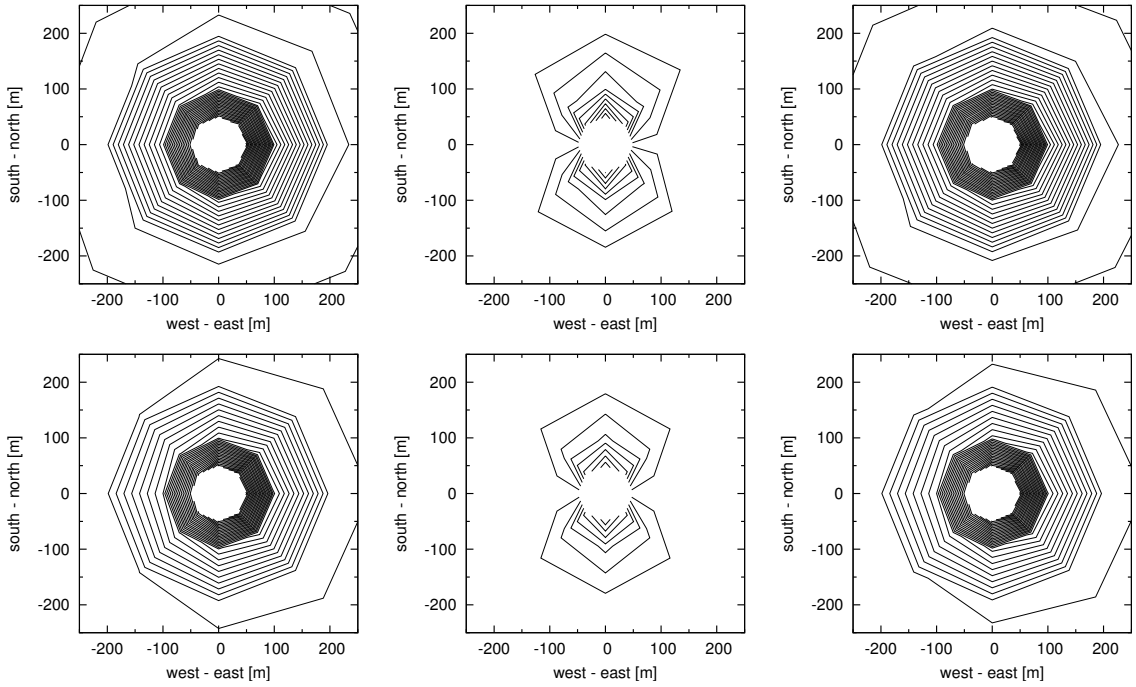

Figure 3.5: Contour plots of the 60 MHz field strength for the emission from a 10^{17} eV vertical air shower. From left to right: total field strength, north-south and east-west polarization component. Contour levels are 0.1 μVm^{-1}MHz^{-1} apart. The closest position of the simulated observers to the shower core is 50 m. Upper row: REAS3. Lower row: MGMR

server positions (east, north, west, south). For observers positioned to the north and south of the impact point, the geomagnetic and charge-excess

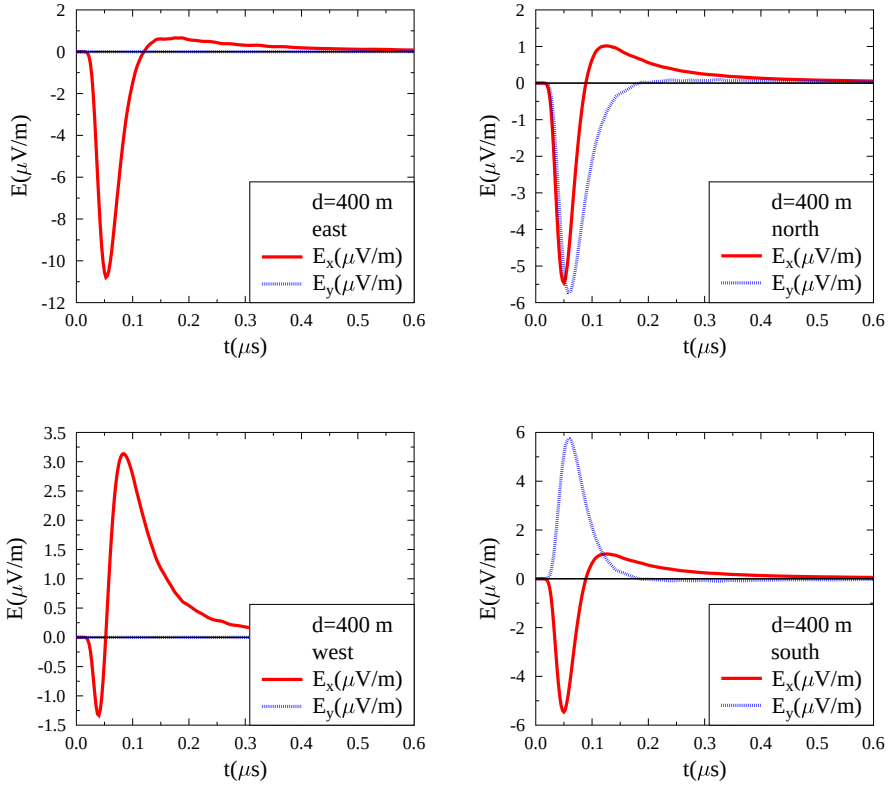

Figure 3.6: Raw electric field in the $\hat{x}$ (east) and $\hat{y}$ (north) polarization simulated with MGMR for observers positioned $d = 400$ m to the east, north, west and south of the impact point.

emission are clearly separated in respectively the $\hat{x}$ (east) and $\hat{y}$ (north) polarization, where the charge-excess emission flips sign indicating a radially inward polarization. From Fig. 3.6 it also follows that the charge-excess emission gives a slightly broader pulse than the geomagnetic emission. This leads to quite different pulse shapes in the east and west directions where the interference between both emission mechanisms is seen. An observer positioned to the east of the impact point sees a stronger signal due to constructive interference, whereas an observer positioned to the west of the impact point sees destructive interference even leading to a flip in polarity for the maximum of the raw electric field.

The pure charge-excess component is given in Fig. 3.7, where the electric field is plotted for a perpendicular 10^{17} eV air shower with the magnetic field switched off as well as the magnetic field parallel to the shower axis. The pulse seems to become unipolar for both REAS3 and MGMR, where the pulse shape and strength agree extremely well for this specific geom-

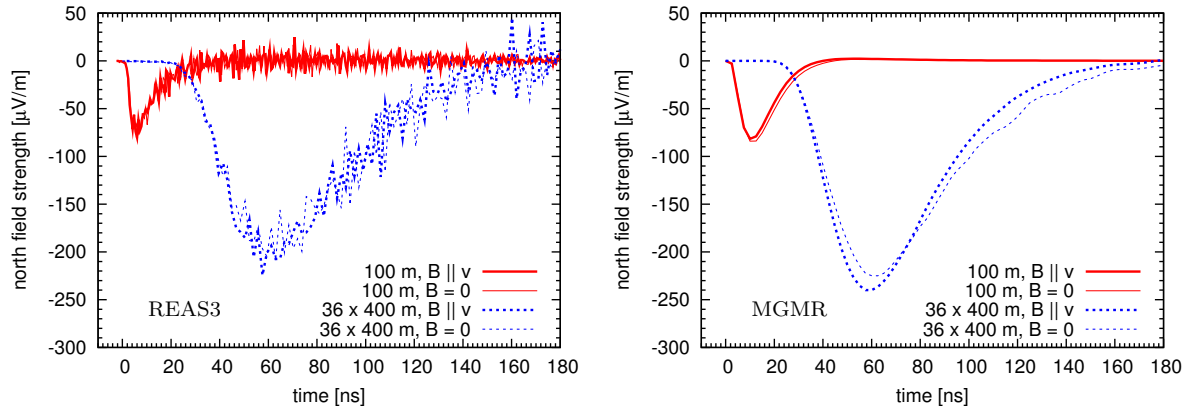

Figure 3.7: Comparison of the pulses emitted by a vertical 10^{17} eV air shower in the absence of a magnetic field (thin lines) and a magnetic field parallel to the shower axis (thick lines). Left: REAS3. Right: MGMR.

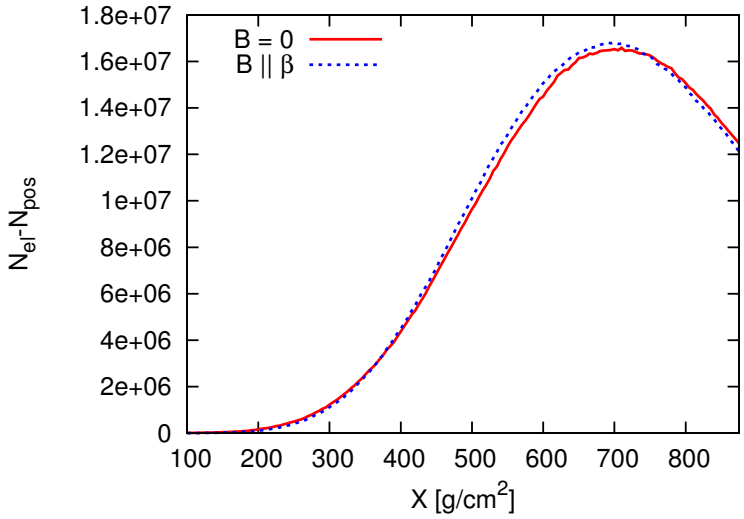

Figure 3.8: Longitudinal development of the charge-excess component for the shower without magnetic field (solid red) and for a magnetic field parallel to the shower axis (dashed blue).

etry. The fact that the pulse becomes unipolar can be understood from the charge-excess profile in Fig. 3.8 showing that the shower maximum is very close to Earth's surface at an altitude of 1400 meters or 875 g/cm^2. The differences in the simulations for the shower with the magnetic field switched off and the magnetic field parallel to the shower axis could be contributed to shower-to-shower fluctuations. In Fig. 3.9, we show the contour plots of the 60 MHz component. Here both models, as expected, show a clear radial polarization pattern.

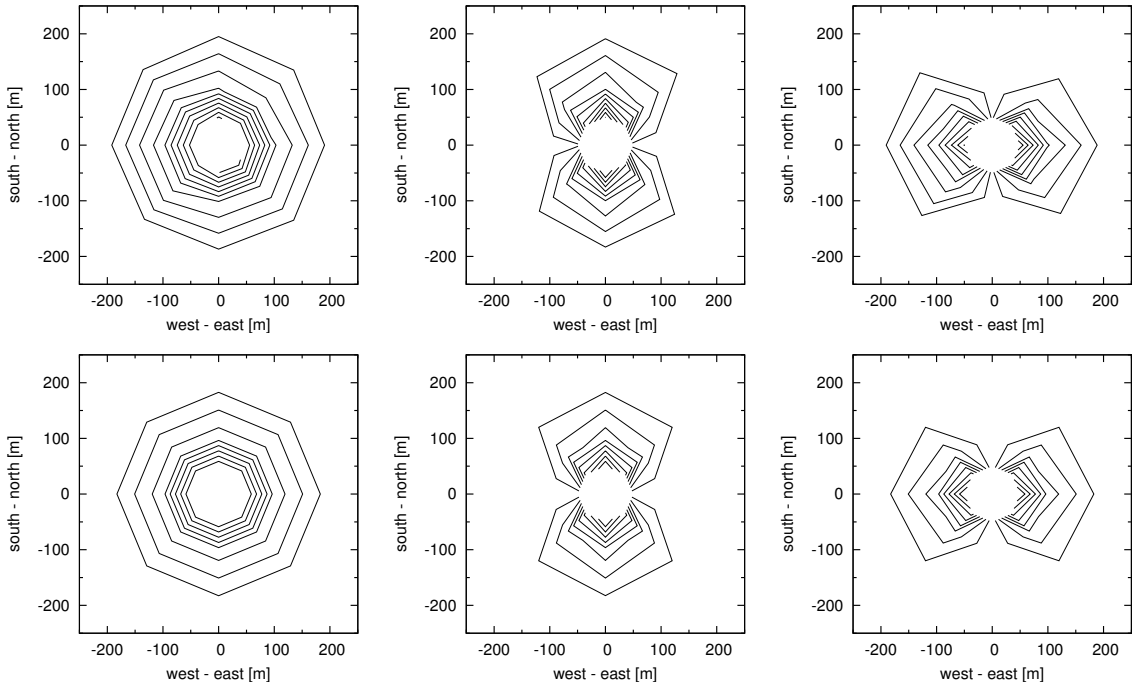

Figure 3.9: Contour plots of the 60 MHz field strength for the emission from a 10^{17} eV air shower where the magnetic field is switched off completely. From left to right: total field strength, north-south and east-west polarization component. Contour levels are $0.1\,\mu\mathrm{Vm}^{-1}\mathrm{MHz}^{-1}$ apart. The closest position of the simulated observers to the shower core is 50 m. Upper row: REAS3. Lower row: MGMR

3.3.2 Inclined air showers

The comparison shown in the previous section was done for a perpendicular incoming air shower. In this section we consider an inclined air shower with a zenith angle of 50 degrees coming from the south-east. In Fig. 3.10 the electric field is shown for different observer distances to the north of the shower core. It should be noted that even though the observer distances are equal to those in Fig. 3.2, the impact parameters are much smaller since we consider an inclined air shower. From Fig. 3.10 it follows immediately that close to the shower core REAS3 and MGMR differ by a factor of 3 in pulse strength for the given geometry. Furthermore, the pulse shape is considerably sharper for REAS3 than for MGMR. This difference is due to the fact that in MGMR a constant longitudinal particle distribution is included which is a convolution between the pancake thickness and the lateral distribution of the charged particles. As shown in later EVA simulations (see Chapter 4), the effect of the pancake width becomes more important for observers positioned close to the shower axis than the lateral distribution. At larger distances from the shower axis, as expected the

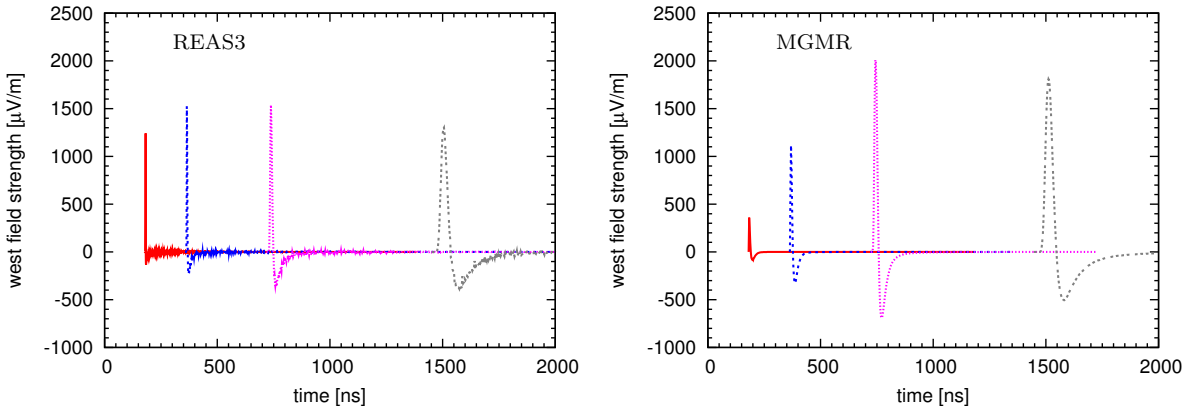

Figure 3.10: Comparison of the east-west polarization component emitted by a 50° inclined air shower with a primary energy of 10^{17} eV for REAS3 (left) and MGMR (right). The figures show pulses for observers at different lateral distances to the shower core. With increasing distance, the results converge. For small distances, the predictions of both models differ by a factor of three.

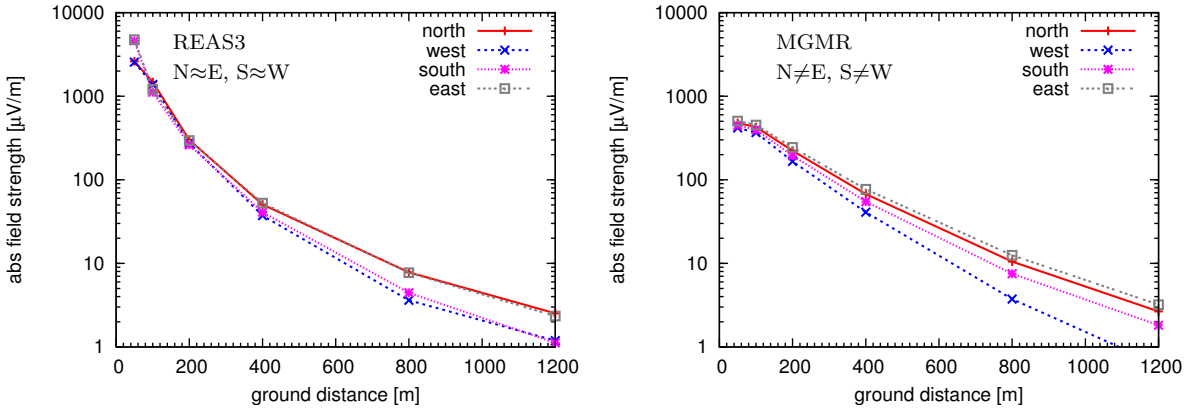

Figure 3.11: Comparison of the lateral dependences with full bandwidth amplitudes for an air shower with zenith angle of 50° and primary energy of 10^{17} eV predicted by REAS3 (left) and MGMR (right). The figures display the maximum absolute field strength at a given lateral distance to the shower core for observers along various azimuthal directions.

difference becomes less and MGMR seems to predict a slightly stronger electric field. The interplay between the geomagnetic radiation and the charge-excess emission can be seen in Fig. 3.11, where the LDF of the maximum unfiltered electric field is given. It follows that REAS3 predicts equal pulse strengths for observers positioned to the east and north of the impact point of the shower and also for those positioned to the west and south. MGMR on the other hand shows different LDF's in all four observer directions (north, east, south and west). This effect might be due to the

implementation of the moving dipole contribution in MGMR, which is not taken into account for in REAS3. This is due to the angular averaging applied in REAS3. Another reason might be the different implementation of the charge-excess contribution. In MGMR, the fraction of charge excess is taken to be a constant fraction of the total number of electrons and positrons in the shower front equal to $C_x = 0.23$. From Fig. 3.12, however we see that the fraction of charge excess is not constant, but varies from 14% to 26% along the shower profile.

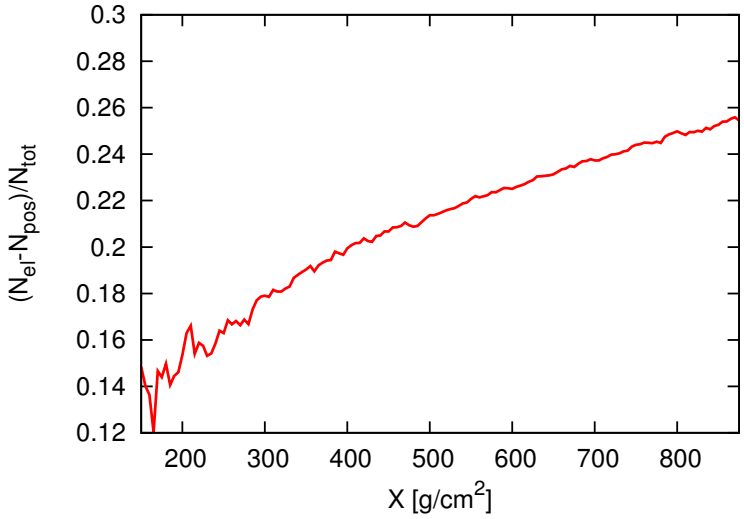

Figure 3.12: Fraction of charge excess with respect to the total number of electrons and positrons as a function of atmospheric depth. With larger atmospheric depth the fraction rises. The large fluctuations below 200 g/cm^2 are due to small particle statistics.

3.3.3 The underlying shower model

The comparison between REAS3 and MGMR discussed in the previous section shows good agreement between the two models. The pulse height differs from a factor of three for small impact parameters and inclined showers to within the 10% level for large impact parameters and vertical showers. Furthermore, the asymmetry due to the interference between geomagnetic radiation and charge-excess emission is observed for both REAS3 and MGMR. Can we understand these remaining differences from the initial differences in the underlying air shower models?
The main difference between both models was the pulse strength for small impact parameters. This can indeed be understood from the underlying air shower model. As explained in the previous chapter, for small impact

parameters the pulse shape and strength is mainly sensitive to the particle distribution in the shower front. Where REAS3 uses the full Monte Carlo information of the shower front, MGMR ignores the lateral distribution of the particles in the shower front and used a parameterization for the longitudinal distribution as given in Eq. (2.4). To check if this is the source of the differences, simulations were performed for a modified version of REAS3, implementing the parameterizations for the shower front as used by MGMR. Furthermore, in REAS3 the electrons and positrons are shifted 7.5 m from the shower axis to take into account for the contribution due to the moving dipole. In Fig. 3.13, we show the comparison between MGMR and the standard and modified version of REAS3.
This is done for observers 100 meters and 800 meters to the north of the vertical 10^{17} eV shower. As expected there is hardly any difference for the simulations at 800 meters from the shower axis. On the other hand, there is a large difference for observers 100 meters from the shower axis. It follows that the modified version of REAS3 agrees much better with the MGMR simulations compared to the standard version. This might be an indication that the average pancake thickness parameter $L = 3.9$ meters is too large when using the approximations done in the MGMR model. This will also be seen in later EVA simulations.

3.3.4 A realistic pancake thickness in MGMR

As stated in the introduction, the pulse shape is a direct reflection of the important length scales involved in an air shower. At small impact parameters the pancake thickness is the important parameter. With this in mind, we can understand why the differences between MGMR and REAS3 are more prominent for small impact parameters. Both simulations use the same shower profile, and hence predict similar pulses for large impact parameters.
In the earlier MGMR calculations [62], the pancake thickness was taken from the measured particle distribution in the shower front at ground, $L = 10\,\mathrm{m}$, which is biased towards relatively large distances from the shower core. This was corrected to $L = 3.9$ m as obtained from Monte-Carlo simulations in the previous chapter. This comparison between REAS3 and MGMR and results from EVA in the following chapter show that $L = 3.9$ m still yields an overestimate since the most important part of the electromagnetic pulse is emitted from distances close to the shower axis [88].
It should however be noticed that in the MGMR model the lateral distribution of the shower particles is ignored, and the effects are taken into

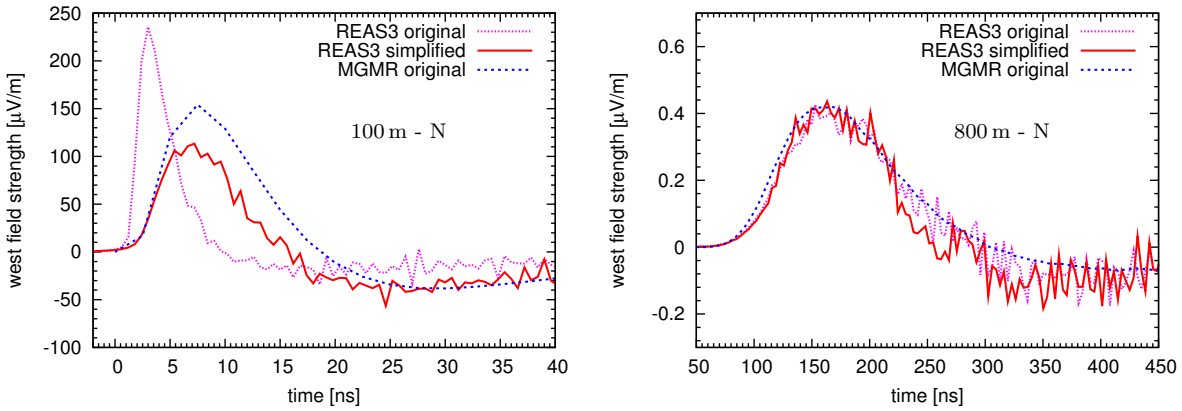

Figure 3.13: A comparison between the radio pulses predicted by MGMR and a modified version of REAS3 where the longitudinal displacement of the particles in the shower pancake follows the distribution used in MGMR and the lateral distribution is replaced by a systematic offset of electrons and positrons. The pulses for a 10^{17} eV vertical air shower are shown for observers 100 m (top) and 800 m (bottom) north of the shower core.

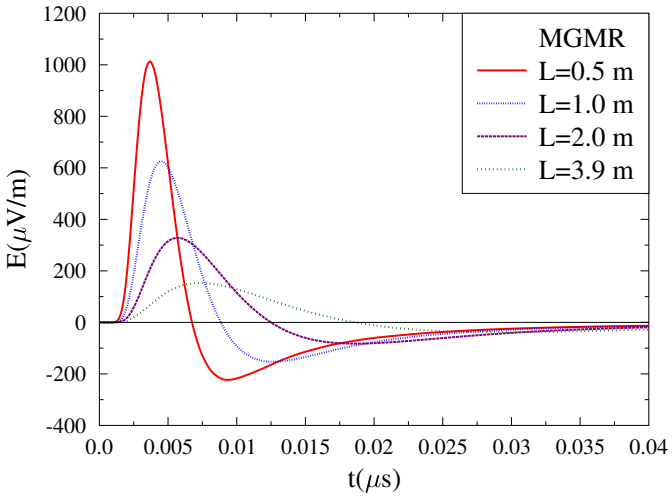

Figure 3.14: MGMR simulations for different values of the pancake thickness parameter L. The simulations are done for a 10^{17} eV vertical shower with the observer positioned 100 m to the north of the impact point. The most realistic value for the shower pancake in MGMR for the air showers considered in this paper is $L = 2$ m.

account by an effective pancake thickness. In figure Fig. 3.14 we show the influence of the pancake thickness parameter L on the simulated pulse shape. This is done for the 10^{17} eV vertical shower for an observer position 100 m north of the shower core. Since the relative importance of the real

pancake distribution and the lateral distribution depends on the observer geometry the effect can be estimated only on average. It follows that for this specific geometry a value of $L = 2$ m gives a good comparison to REAS3 as given in Fig. 3.13.

3.4 Conclusion

A detailed comparison between the microscopic approach of the REAS3 model and the macroscopic MGMR model shows that there has been a huge increase in the understanding of the radio emission for both the pulse shape and strength as well as the emission mechanism over the last few years.
There are still differences between both approaches that are mainly due to the different assumptions in the models. REAS3 obtains the particle distributions in the shower front from Monte Carlo simulation, ignoring the dipole contribution due to the azimuthal averaging procedure that is applied. MGMR ignores the lateral particle distribution in the shower front and uses a simple parameterization for the longitudinal particle distribution. The differences between both models vary from a factor of two to three in pulse height for inclined showers and small impact parameters up to less than 10% for vertical showers and large impact parameters. Since at small impact parameters the pulse shape and strength is mainly determined by the particle distributions in the shower front, this clearly indicates that the effective pancake thickness parameter L used by MGMR as obtained in the previous chapter is too large at small impact parameters. This is confirmed by calculations in the previous sections.
Since the lateral particle distribution in the shower front is ignored, the pancake thickness parameter L should be regarded as an effective parameter that corresponds to a convolution of the real pancake thickness and the radial extent of the shower.

Chapter 4

The EVA code: Coherent Cherenkov radiation from cosmic-ray-induced air showers

Parts of this chapter are published (or have been submitted) in the following articles:

Coherent Cherenkov Radiation from Cosmic-Ray-Induced Air Showers
Phys.Rev.Lett. 107:061101, (2011)
K. D. de Vries[1], A. M. van den Berg[1], O. Scholten[1], and K. Werner[2]

A Realistic Treatment of Geomagnetic Cherenkov Radiation
Astroparticle Physics 37, 516, (2012)
Klaus Werner[2], Krijn D. De Vries[1], and Olaf Scholten[1]

The air shower maximum probed by Cherenkov effects from radio emission
Krijn D. de Vries[1], Olaf Scholten[1], and Klaus Werner[2]
Submitted to Astroparticle Physics

[1]*Kernfysisch Versneller Instituut, University of Groningen, 9747 AA, Groningen, The Netherlands*
[2]*SUBATECH, University of NantesIN2P3/CNRSEMN, Nantes, France*

4.1 Introduction

It is a well-known fact that an emitting source moving at a velocity exceeding the wave-propagation velocity in the medium will induce a shock-wave. Prime examples of this phenomenon are the sonic boom emitted by a supersonic airplane, a bow-wave from a moving ship, and Cherenkov radiation emitted by an electric charge moving at almost the vacuum speed of light in a medium with an appreciable index of refraction. In this chapter we show that a similar effect occurs in the radio emission from a cosmic-ray-induced air shower.

In Chapter 2 we saw that even when the index of refraction of air would be equal to that of vacuum this varying electric current emits electromagnetic waves and coherent emission occurs at a wavelength longer than the size of the charge cloud, i.e. for radio frequencies $\nu < 300\,\mathrm{MHz}$ [76]. As is well known the propagation speed of electromagnetic waves is c/n where c denotes the velocity of light in vacuum. In this chapter we investigate the effect of the index of refraction of air, n, on the emission following Ref. [73]. The effects of Cherenkov radiation from EAS have also been addressed in Ref. [89]. In this chapter we show that for realistic values for n the Cherenkov effect introduces distinct features in the ground pattern of the emitted radiation. In the first section we discuss a simple one-dimensional model to describe Cherenkov effects. In the following section we give the general derivation of the electric fields for a realistic varying index of refraction. We also discuss the evaluation of the fields by using the EVA 1.0 package. The particle distributions and currents as obtained from Monte Carlo simulations are discussed as well as the fit-functions that are used to calculate the fields. We show results for a realistic calculation and discuss the effects of the refractivity. To conclude we discuss how Cherenkov effects influence the different emission mechanisms. These Cherenkov effects cause the radio pulse to be very sensitive to the position of the shower maximum which may be used to determine the chemical composition of the initial cosmic ray.

4.2 Cherenkov effects: A simple model

Following the discussion in Chapter 2, the vector potential for a point-like source can be written as,

$$A^{\beta}(t,\vec{x}) = \frac{\mu_0}{4\pi}\frac{J^{\beta}(t',\vec{\xi})}{\mathcal{D}}. \tag{4.1}$$

Here J^μ is the four-current at the position $\vec{\xi} = -\beta ct' \hat{x}^{||}$ along the shower axis, where t' is the negative retarded time when the signal is emitted. The observer is located at the position $\vec{x} = d\ \hat{x}^{\perp}$. For a point source, the retarded distance, as derived in Chapter 2, becomes,

$$\mathcal{D} = \sqrt{(-c\beta t)^2 + (1 - n^2\beta^2)d^2}\ , \tag{4.2}$$

where in the macroscopic description of radio emission from air showers, $\beta = 1$. Nevertheless, β is kept in the notation for completeness. From Eq. (4.2), we already see that for a finite refractivity $N = n - 1$ the retarded distance vanishes at positive values of d, and t. The singularity in the vector potential due to the vanishing of the retarded distance is the well-known Cherenkov effect. At this point the critical values of d_c, and t_c where the retarded distance vanishes can be defined by the condition,

$$\mathcal{D}(t_c, d_c) = 0\ . \tag{4.3}$$

Furthermore, there is the light-cone condition that has to be fulfilled which is given by,

$$c(t - t') = nR, \tag{4.4}$$

where $R = \sqrt{(-\beta ct')^2 + d^2}$ is the distance from the observer to the emission point. Using these two equations, we can link the critical values t_c when Cherenkov effects are observed, the critical emission time t'_c, and the distance where Cherenkov effects are observed d_c. The critical values are linked by,

$$\beta ct_c = \sqrt{n^2\beta^2 - 1}\ d_c \tag{4.5}$$

$$-\beta ct'_c = \frac{d_c}{\sqrt{n^2\beta^2 - 1}}. \tag{4.6}$$

An extensive air shower typically reaches its maximum (the point where it contains the largest amount of electrons and positrons) at around four kilometers height. The radius of the Cherenkov cone for emission at this height corresponds to approximately 100 meters for a constant index of refraction equal to its value at sea level, $n = 1.0003$. This means that Cherenkov effects may play an important role in radio emission from air showers for observers at intermediate distances around $50 - 300$ meters from the shower axis depending on zenith angle, energy, and composition of the initial cosmic ray. The opening angle at which Cherekov emission is observed, the so-called Cherenkov angle, is given by

$$\cos\theta_c = \frac{z_c}{R_c}, \tag{4.7}$$

using $z_c = -\beta c t'_c$ and $R_c = \sqrt{z_c^2 + d_c^2}$. In combination with Eq. (4.6) one can easily show that,

$$\cos\theta_c = \frac{1}{n\beta}. \tag{4.8}$$

Another, more intuitive interpretation of the Cherenkov effect is obtained by linking the retarded distance to the derivative of the observer time with respect to the emission time. One can easily show that the relation

$$\mathcal{D} = R\frac{dt}{dt'} \tag{4.9}$$

holds. This means that at the critical times t_c and t'_c, the derivative dt'_c/dt_c diverges. The physical interpretation of this divergence is that no longer an infinitesimal part of the shower is observed at a fixed observer time t_c, but rather the signals emitted along a finite track. Due to this boosting the observed signal is strongly amplified.

4.3 The vector potential: Solving for the singularities

Since the atmospheric density is height dependent, the refractivity will depend on height $N = N(z)$. In this work the refractivity is modeled by the Gladstone-Dale law,

$$N = 0.266\frac{\mathrm{cm}^3}{\mathrm{g}}\rho(z). \tag{4.10}$$

Where $\rho(z)$ is the density of air at a height z. The Liénard-Wiechert potentials of classical electrodynamics are used in the more general form for a point-like source,

$$A^{\beta}_{PL}(t,\vec{x}) = \frac{\mu_0}{4\pi}\frac{J}{|\tilde{R}V|}, \tag{4.11}$$

where $V = c^{-1}d\xi/dt'$, and $\tilde{R}$ is the four vector defined by $\tilde{R}^0 = c(t-t')$ and $\tilde{R}^i = -L\partial/\partial\xi^i L$, with L being the optical path length between the emission point $\vec{\xi}(t')$ and the observer. Note that since the density of the atmosphere is a function of height, in principle the signal does not travel along a straight line but on a curved trajectory.
In [73] it is shown that for a realistic varying index of refraction, the denominator in the vector potential can still be linked to the derivative of the emission time with respect to the observer time $1/|\tilde{R}V| \propto dt'/dt$.

In Fig. 4.1, the emission height, $z = -\beta ct'$, is plotted as a function of observer time for a 27 degrees inclined air shower with an energy $5 \cdot 10^{17}$ eV for an observer 100 meters from the shower axis. It is seen from this figure that t' is a non-monotonic function of t and Cherenkov effects may occur. For an index of refraction equal to unity the emission height as a function of observer time is, as expected, continuously decreasing and hence no divergences occur in the vector potential. On the other hand, for a realistic index of refraction as well as a constant index of refraction equal to its value at sea level there is clearly a point on the curve where the derivative $dz/dt = -\beta c\, dt'/dt$ diverges giving rise to Cherenkov effects. Another interesting point to notice is that the observer time corresponding to the critical Cherenkov time $t = t_c$ corresponds to the starting time of the pulse.

To overcome the divergences in the vector potential we make use of

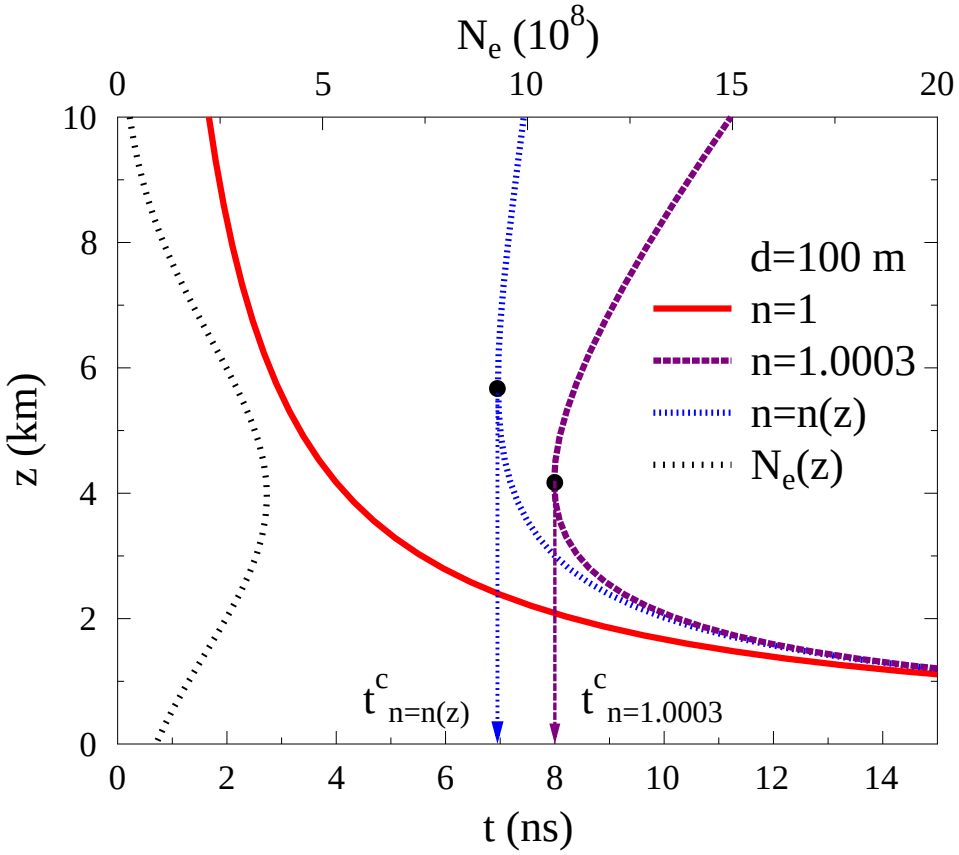

Figure 4.1: The emission height $z = -\beta ct'$ as function of the observer time t for three different values of the index of refraction. The dashed line gives the shower-profile as function of z for a $E = 5 \times 10^{17}$ eV proton-induced shower.

the finite extent of the particle distribution in the shower front. The finite extent can be expressed through a weight function $w(r^1, r^2, h)$, where r^1 and

r^2 are the transverse distances to the shower axis and h is the longitudinal distance behind the shower front. The exact form of the weight function will be discussed in the following section. In principle one now needs to make the convolution of the weight function and the currents, and from thereon calculate the vector potential. Nevertheless, due to translational invariance (which is a very good approximation in this case since the index of refraction changes very slowly) we can safely make the convolution with the point-like vector potential,

$$A^\beta(t,\vec{x}) = \int d^2\vec{r} \int dh\; w(\vec{r},h) A^\beta_{PL}(t, x^{||} - h, \vec{x}^\perp + \vec{r}). \tag{4.12}$$

It is usefull to define the transverse coordinate $\vec{y}^\perp = \vec{x}^\perp + \vec{r}$. The vector potential now becomes,

$$A^\beta(t,\vec{x}) = \int d^2\vec{y}^\perp \int dh\; w(\vec{y}^\perp - \vec{x}^\perp, h) A^\beta_{PL}(t, x^{||} - h, \vec{y}^\perp). \tag{4.13}$$

Due to the divergences in the vector potential we cannot simply interchange integration and derivation and make the convolution with E_{PL} and the weight function w. Therefore, in the following a general derivation will be given for an arbitrary non-monotonic emission time t' as a function of the observer time t. This function can in general contain several branches at the critical times $t = t_{c,i}$. At these branch points,

$$|t' - t'(t_c)| \sim |t - t_c|^{1/2}, \;\; \text{and,} \;\; \frac{dt'}{dt} \sim |t - t_c|^{-1/2}. \tag{4.14}$$

Hence the denominator has a square-root divergence that can be safely integrated. In general the critical time t_c is a function of the observer position with respect to the emission point. Therefore we can define a critical value h_c where the denominator becomes singular,

$$\tilde{R}V(t,h_c) = 0. \tag{4.15}$$

Thus the expression for a single branch is now given by,

$$A^\beta(t,\vec{x}) = \int d^2\vec{y}^\perp \int_0^{h_c} dh\; w(\vec{y}^\perp - \vec{x}^\perp, h) A^\beta_{PL}(t, x^{||} - h, \vec{y}^\perp). \tag{4.16}$$

To avoid the interference of the derivatives needed to obtain the electric field with one of the divergences in the vector potential we now shift the divergence in the vector potential to the lower limit of the integral by

defining the coordinate $\lambda = h_c - h$. The final form of the vector potential now becomes,

$$A^\beta(t,\vec{x}) = \int d^2\vec{y}^\perp \int_0^{h_c} d\lambda\; w(\vec{y}^\perp - \vec{x}^\perp, h_c - \lambda) A^\beta_{PL}(t, x^{||} - h_c + \lambda, \vec{y}^\perp). \quad (4.17)$$

The electric fields are obtained by the standard relation,

$$E^{||} = c\left(-\frac{\partial A^0}{\partial x^{||}} - \frac{\partial A^{||}}{\partial ct}\right) \quad (4.18)$$

$$E^{\perp i} = c\left(-\frac{\partial A^0}{\partial x^{\perp i}} - \frac{\partial A^{\perp i}}{\partial ct}\right). \quad (4.19)$$

4.3.1 The electric field: Solving for the derivatives

To obtain the electric field we first need to solve for the derivatives acting on the point like vector potential given by $A^i_{PL} = J^i/|\tilde{R}V|$. After the coordinate transformations, the arguments of $A^i_{PL}(t, x^{||} - h_c + \lambda, \vec{y}^\perp)$ are the observer time t, the longitudinal coordinate $x^{||} - h_c + \lambda$, and the lateral coordinate $\vec{y}^\perp$ which will be omitted in the following since the derivatives do not act on this integration variable. Furthermore, we adapt the notation $\partial^0 f = \partial f/\partial ct$, and $\partial^z f = -\partial f/\partial z$. The total derivatives are given by, $d^0 f = df/dct$, $d^z f = -df/dx^{||}$. We consider for a fixed h and a fixed observer position, the retarded time $t'(t, x^{||} - h)$. A critical time t'_c corresponds to a critical time t_c for a fixed value of $z - h$, i.e. $t_c = t_c(z - h)$ and thus $t'_c = t'_c(z - h)$. We have

$$d^z t'_c = \partial^0 ct' d^z t_c + \partial^z t'. \quad (4.20)$$

In the following we will make use of definitions and relations obtained in [73]. For $t = t_c$, we have

$$\tilde{R}V = c(t_c - t'_c) - \tilde{R}_j V^j|_{t'=t'_c} = 0. \quad (4.21)$$

We compute the derivative d^z:

$$\begin{aligned}
0 &= d^z ct_c - d^z ct'_k + (\bar{g}^z_j - \tilde{V}_j d^z ct'_k)V^j && (4.22)\\
&= d^z ct_c - (1 - \tilde{V}^j V^j) d^z ct'_k + \bar{V}^z && (4.23)\\
&= d^z ct_c - \tilde{V}V d^z ct'_c + \bar{V}^z && (4.24)\\
&= d^z ct_c - \tilde{V}V(\partial^0 ct' d^z ct_c + \partial^z ct') + \bar{V}^z, && (4.25)
\end{aligned}$$

which leads to (using $\bar{V}^z = \bar{V}^{||}$)

$$d^z ct_c = \frac{-\bar{V}^{||} + \tilde{V}V\partial^z ct'}{1 - \tilde{V}V\partial^0 ct'}. \tag{4.26}$$

Using

$$\partial^\alpha ct' = \frac{\bar{R}^\alpha}{\tilde{R}V}, \tag{4.27}$$

we get

$$d^z ct_c = -\frac{\bar{V}^{||} - \tilde{V}V\bar{R}^{||}/\tilde{R}V}{1 - \tilde{V}V\bar{R}^0/\tilde{R}V}. \tag{4.28}$$

The time derivative of h_c as obtained from its definition is

$$d^0 h_c = (d^z ct_c)^{-1}, \tag{4.29}$$

which gives

$$d^0 h_c = -\frac{\tilde{R}V - \tilde{V}V\bar{R}^0}{\tilde{R}V\bar{V}^{||} - \tilde{V}V\bar{R}^{||}}. \tag{4.30}$$

Using $\tilde{R}V = 0$, and $\bar{R}^{||} = L = \bar{R}^0$, we find

$$d^0 h_c = -1 \tag{4.31}$$

The other derivative of h_c is trivial:

$$d^z h_c = -1. \tag{4.32}$$

The potential A, its denominator $\tilde{R}V$, and also the arguments ct' of its numerator J are evaluated at the parallel coordinate $x^{||} - h_c + \lambda$, so the total time derivatives are,

$$d^0 = \partial^0 + d^0 h_c \partial^z, \tag{4.33}$$

explicitly

$$d^0 = \partial^0 - \partial^z. \tag{4.34}$$

We get

$$d^0 ct' = (\partial^0 - \partial^z)ct' = \frac{\bar{R}^0 - \bar{R}^z}{\tilde{R}V} = 0, \tag{4.35}$$

and with

$$\partial^\alpha \tilde{R}V = \bar{V}^\alpha - \tilde{V}V\partial^\alpha ct' \tag{4.36}$$

(eq. (22) from [73]), we obtain

$$d^0 \tilde{R}V = 0. \tag{4.37}$$

At this point we have all the desired derivatives to solve for the electric fields as given in Eq. (4.18) and Eq. (4.19). Starting with the vector potential given by $A^i_{PL} = \frac{\mu_0}{4\pi} J^i/|\tilde{R}V|$ and using the derivatives derived above the time derivative of the vector potential is given by,

$$-\frac{\partial A^i}{\partial ct} = \int d^2y_\perp \int_0^{h_c} d\lambda \, \left\{ -w' A^i_{PL} + w \dot{A}^i_{PL} \right\}, \tag{4.38}$$

where we omitted the arguments of the vector potential to simplify the notation. Here $w' = dw/dh$, and $\dot{A}^i_{PL} = \frac{\mu_0}{4\pi} K^i$, where $K^i = dJ/dt'$. The term acting on the upper limit of the integration vanishes since $w(0) = 0$ as will be discussed in Section 4.4. We separate the longitudinal and transverse components of the electric field. The longitudinal derivative is given by,

$$-\frac{\partial A^0}{\partial x^{||}} = -\int d^2y_\perp \int_0^{h_c} d\lambda \, w' A^0_{PL}, \tag{4.39}$$

Where the derivative acting on A^0_{PL} vanishes exactly. The transverse derivative of the zeroth component of the vector potential is given by,

$$-\frac{\partial A^0}{\partial x^{\perp i}} = \int d^2y_\perp \int_0^{h_c} d\lambda \, w^i A^0_{PL}, \tag{4.40}$$

where $w^i = \partial w/\partial r^i$ is the transverse derivative of the weight function w. Pluging in these derivatives in Eq. (4.18) and Eq. (4.19) now gives the electric field components. The longitudinal electric field component is given by,

$$E^{||} = -c \int d^2y_\perp \int_0^{h_c} d\lambda \, \left\{ w' A^0_{PL} - w' A^{||}_{PL} + w \dot{A}^{||}_{PL} \right\}. \tag{4.41}$$

The transverse electric field component is given by,

$$E^{\perp i} = c \int d^2y_\perp \int_0^{h_c} d\lambda \, \left\{ w^i A^0_{PL} + w' A^\perp_{PL} - w \dot{A}^{\perp i}_{PL} \right\}. \tag{4.42}$$

The formulas simplify considerably far from the singularity as well as at the singularity, but we keep the exact expressions in order to interpolate

correctly between the two extremes. It should be noted that the above expression concerns a single branch, the complete field is the sum over all branches.
It should be noted that Eq. (4.41) and Eq. (4.42) are not plagued with singularities since the particles in the shower front are distributed over over a finite volume. We also explicitly include both the near- and the far-field components of the radiation. In this sense it differs considerably from the calculations presented in [68] where an ad-hoc frequency cut-off is introduced in the calculations of 300 MHz, and the near-field component of the electric field is neglected (the Fraunhofer condition). As can be seen from Fig. 4.24 below, the data show a considerable intensity above 300 MHz. A question that arises in this respect is the validity of the Fraunhofer condition when Cherenkov effects come into play which implicitly is assumed in [68]. Often the Fraunhofer condition is formulated as $a^2 \sin^2\theta/R < \lambda/2\pi$,where a is the length of the emission trajectory, θ is the opening angle from the emission point to the observer, λ the wavelength of the emitted signal, and R the distance from the emission point to the observer. If there is a single point on a where the Cherenkov condition is fulfilled, the electric field will diverge at this point whereas the field is finite at all other points. This implies that thus the Fraunhofer condition is not valid. A Lorentz-invariant formulation of the Fraunhofer condition is $a^2 \sin^2\theta/\tilde{R}V < \lambda/2\pi$, where the distance R is replaced by the retarded distance $\tilde{R}V$. Since the retarded distance vanishes at the Cherenkov angle this clearly shows that at this point the Fraunhofer condition is no longer valid for which reason we have not made this assumption in our approach.

4.4 Monte-Carlo simulations and fitting procedures: EVA 1.0

The numerical evaluation of Eq. (4.41) and Eq. (4.42) is done employing the EVA 1.0 package, which

- provides the weights w,
- provides the currents J needed to compute the potentials A^{μ}_{PL},
- does the numerical integration of Eq. (4.41) and Eq. (4.42) and the summation over the branches.

Both the weights w and the point-like currents J are obtained from realistic Monte Carlo simulations of air showers. The EVA package consists of several elements:

- the air shower simulation code CX-MC-GEO, including analysis tools to extract four-currents and the shape of the shower,
- the automatic fitting procedure FITMC which allows to obtain analytical expressions for the currents,
- the EVA program which solves the non-trivial problem to compute the retarded time and the denominator $\tilde{R}V$, for a realistic index of refraction.

We first discuss air showers. The shower front is considered a point, moving along a straight line trajectory, see Fig. 4.2. One defines an observer level which is a plane of given altitude z with respect to the sea level. One

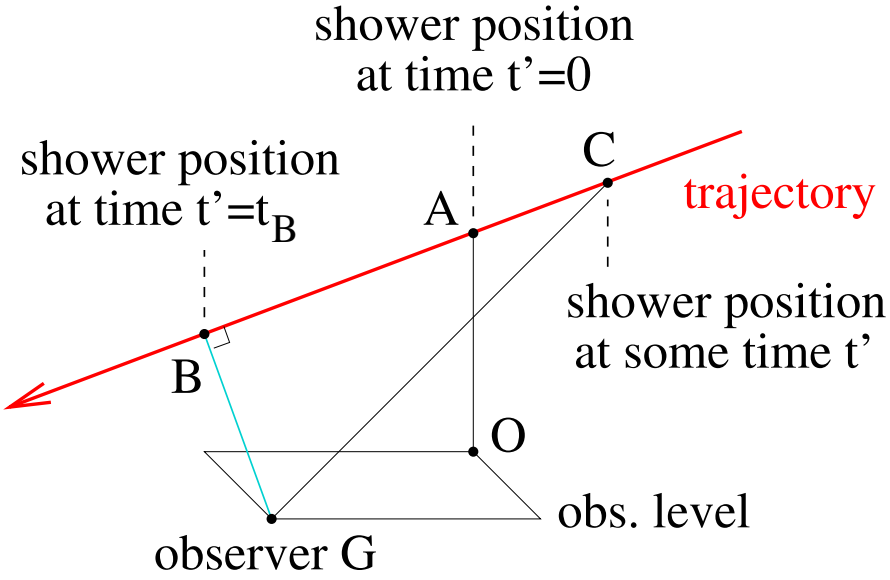

Figure 4.2: Air shower as seen by an observer G. The point B is the point of closest approach with respect to the observer G. The point C is the shower position at some time t'. The point B corresponds to the shower position at $t' = t_B$ (which may be taken to be zero).

defines some arbitrary point A on the trajectory. The corresponding projection to the observer level is named O (origin) and the observer position is given in terms of coordinates (x, y) with respect to O. The x-axis is the intersection of the shower plane OAC and the observer level. The angle between the shower trajectory and the vertical axis OA is referred to as inclination and denoted as θ. In many applications, A and O coincide: in this case they represent the impact point. For horizontal showers the two points are different. The geomagnetic field is specified by an angle α with respect to the vertical, and an angle ψ with respect to the shower plane ($\psi = 0$ means that B points towards the shower origin). One can of

course see it the other way round (maybe even more natural): for a given orientation of the geomagnetic field, ψ defines the orientation of the shower axis. In the EVA framework, one has to specify the altitude z, the distance $a = |OA|$, the inclination θ, the energy E of the shower, and the observer coordinates x, y. In addition the angles α and ψ and the magnitude B of the geomagnetic field have to be given. The actual air shower simulations are done with a simulation program called CX-MC-GEO, being part of the EVA package. It is based on CONEX [21, 22], which has been developed for air shower calculations based on a hybrid technique, which combines Monte Carlo simulations and numerical solutions of cascade equations. It is also possible to run CONEX in a pure cascade mode, and this is precisely what we use. This provides full Monte Carlo air shower simulations, using EGS4 [90] for the electromagnetic cascade, and the usual hadronic interaction models (QGSJET, EPOS, etc) to simulate hadronic interactions. Two features have been added to CONEX. First of all a magnetic field, which amounts to replacing the straight line trajectories of charged particles by curved ones. This concerns both the electromagnetic cascade and the hadronic one. In addition, analysis tools have been developed, which allow to get a complete information of charged particle flow in space and time. These features have already been developed to compute currents in [73], so in particular more details about the implementation of the magnetic field can be found there (though we did not use the names EVA and CX-MC-GEO yet). We also discuss in [73] some details about the different internal coordinate systems needed to extract information about currents. The results shown in [66] were also based on CX-MC-GEO simulations, referred to as CONEX-MC-GEO at the time. In [73], we provide several results concerning particle numbers and currents for different orientations of the axis with respect to the geomagnetic field. All the results are still valid, the corresponding programs did not change since. An important ingredient of our approach is the parametrization of the results (currents J, distributions w), which have be obtained from simulations in the form of discrete tables. This is necessary partly to perform semi-analytical calculations such that numerically stable functions have to be dealt with without having huge cancellations in the results. It is especially important for the stable calculation of Cherenkov effects. It allows for the calculation of a smooth shower evolution, whereas when working with histogrammed distributions in position and time, it is not possible to reconstruct a continuous shower evolution and the artificially introduced sudden changes in the particle trajectories may give rise to spurious radio signals. The parametrization of Monte Carlo distributions is done in FITMC. This program takes the distributions (four currents) as obtained from the simulations in the

form of histograms, to obtain analytical expressions, using standard minimization procedures. FITMC creates actually computer code to represent the analytical functions, and this code is then executed at a later stage. The basic distribution is the so-called electron number N (which counts the number of electrons and positrons) as a function of the shower time t , which is fitted as

$$N(t') = A\exp(B + C(t' + D) + E(t' + F)^2 + G(t' + H)^3) \tag{4.43}$$

As an illustration, we show here the case of a shower with an initial energy of $5 \cdot 10^{17}$ eV, an inclination $\theta = 27°$, and an azimuth angle $\psi = 0°$, defined with respect to the magnetic north pole. The angle ψ refers to the origin of the shower. So $\psi = 0°$ thus implies that the shower moves from north to south. We consider the magnetic field at the CODALEMA site, i.e. $|B| = 47.3\ \mu T$ and $\alpha = 153°$, so the shower makes an angle of roughly $54°$ with the magnetic field. In Fig. 4.3, we plot the electron number N, as a function of the shower time t, for a simulated single event, together with the fit curve. A thinning procedure has been applied (here and in the following) to obtain the shown simulation results. The time $t = 0$ refers to the point of closest approach with respect to an observer at $x = 0$, $y = 500$ m, $z = 140$ m. We suppose $a = 0$ (so the shower hits the ground at $x = y = 0$). The magnitudes of the components J^μ of the currents have a similar t' dependence as $N(t')$. Therefore we parametrize the ratios $J^\mu/(Nec)$, with N being the electron number, e the elementary charge, and c the velocity of light. We use the following parametric form:

$$\frac{J^\mu(t')}{N(t')ec} = A + B(x + C) + D(x + E)^2 + F(x + G)^3. \tag{4.44}$$

In Fig. 4.4 we plot the longitudinal current component J^z
(divided by Nec), as a function of the shower time t', for a simulated single event, together with the fit curve. At early times - far away from the shower maximum there are of course large statistical fluctuations. But since $N(t')$ is very small here, this region does not contribute to the pulse. In Fig. 4.5, we plot the transverse current components J^x and J^y, (divided by Nec), as a function of the shower time t', for a simulated single event, together with the fit curves. The EVA program uses these analytical fit functions for the current components,

$$J^\mu = \left\{\frac{J^\mu}{Nec}\right\}_{fit} \cdot N_{fit} \cdot e \cdot c, \tag{4.45}$$

to compute the vector potential. The currents have to be evaluated at $t = t'$, the retarded time. The central part of EVA is actually the determination of the retarded time $t'(t, \vec{x})$ for a given observer position. This is

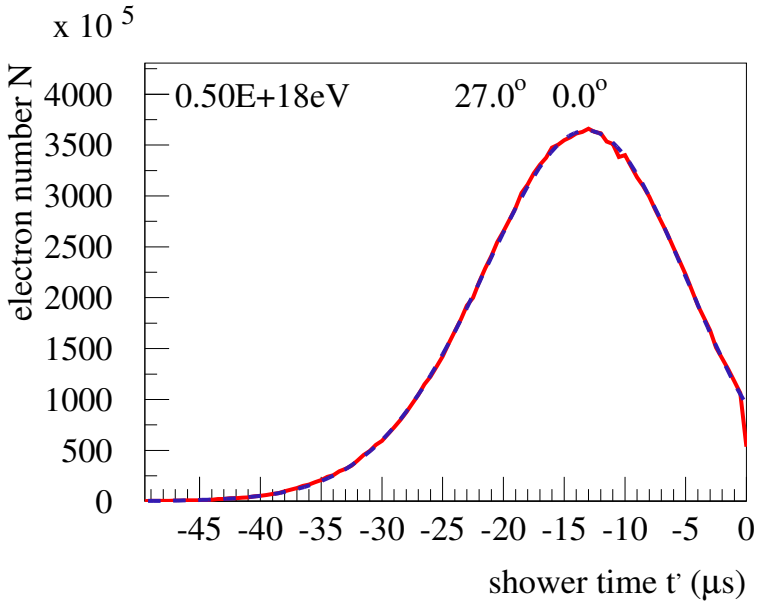

Figure 4.3: The number N of electrons and positrons, as a function of the shower time t' for a shower with an inclination $\theta = 27^0$ and an azimuth angle $\psi = 0^0$ with respect to the magnetic north pole. The full red line represents the simulation result, the dashed blue line is the fit.

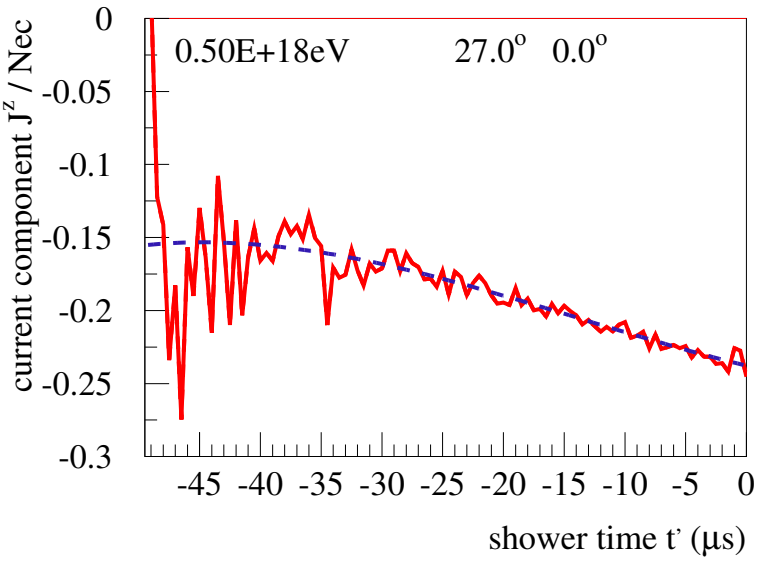

Figure 4.4: The longitudinal current component J^z, divided by Nec, as a function of the shower time t'. The full red line represents the simulation result, the dashed blue line is the fit.

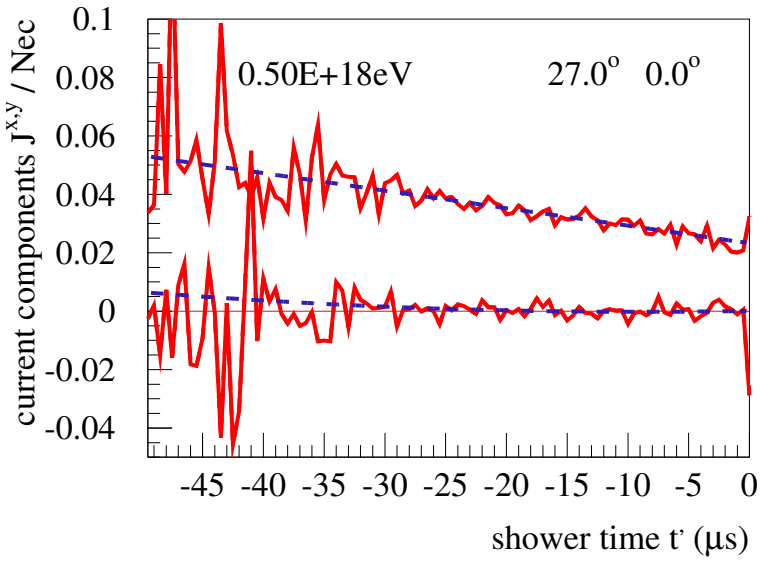

Figure 4.5: The transverse current components J^x (lower lines) and J^y (upper lines), divided by Nec, as a function of the shower time t'. The full red lines represents the simulation result, the dashed blue lines are the fits.

quite involved in case of a realistic index of refraction and described in detail in [73] (again without referring to EVA, but these are exactly the same programs being used). A result of such a calculation is shown in Fig. 4.1. A new feature compared to [73]- and most relevant for this paper - is the possibility to obtain information about the shape of the shower via the weight function w. The weight function w is not perfectly cylindrically symmetric, due to the geo-magnetic field but also due to statistical fluctuations, since we are considering individual Monte Carlo events. However, in this paper we will neglect these tiny deviation from symmetry, and consider a weight function $w(r, h)$ depending only on the two variables r and h, related to the general weight function as

$$w(r, h) = 2\pi r w(\vec{r}, h). \tag{4.46}$$

The lateral coordinate r measures the transverse distance from the shower axis, the longitudinal coordinate h is meant to be the distance behind the shower front. This front is a hypothetical point moving along the shower axis with the velocity of light c, such that all the particles are behind this front, expressed by a positive value of h. We will express the weight function as

$$w(r, h) = w_1(r) w_2(r, h), \tag{4.47}$$

with $\int\ dr\ w_1(r) = 1$, and with $\int\ dh\ w_2(r,h) = 1$ for all values of r.

We use again CX-MC-GEO to obtain w, then FITMC to obtain an analytical function, which is later used in the EVA program to compute the fields, based on the formulas described in the preceding section. All the simulation results shown in the following are based on the the same shower, mentioned earlier when discussing currents.
We first investigate the radial distribution $w_1(r)$. In Fig. 4.6, we show the radial distribution as obtained from the Monte Carlo simulation. The thin lines correspond to different times t', between $-25\ \mu s$ and $-5\ \mu s$. The points represent an average over all times, and also averaged over r-bins. Since the time dependence is quite small, we will use the radial distribution at the shower maximum t'_{max} as time-independent distribution $w_1(r)$. The thick red line corresponds to a fit to the Monte Carlo data, using the form

$$w_1(r) = \frac{\Gamma(4.5-s)}{\Gamma(s)\Gamma(4.5-2s)} \left(\frac{r}{r_0}\right)^{s-1} \left(\frac{r}{r_0}+1\right)^{s-4.5}, \tag{4.48}$$

with fit parameters r_0 ans s (providing an excellent fit).
Knowing $w_1(r)$, we now investigate how far the particles are moving behind the shower front, expressed in terms of the longitudinal distance h, for a given transverse distance r. From the above simulation, we obtain easily the mean distance $\bar{h}$ at a given r. We find a perfectly linear time dependence, of the form

$$\bar{h} = h_0 + c\Delta\beta t', \tag{4.49}$$

where $\Delta\beta$ can be obtained from fitting time dependence at different distances r, the result is shown in Fig. 4.7 as solid line. The quantity $\Delta\beta$ represents the velocity difference (in units of c) with respect to the the shower front, which itself moves with velocity c. So the velocity of the average position of the shower is $1-\Delta\beta$. Also shown in Fig. 4.7, as dashed line, is the value $1 - 1/n_{\rm ground}$, corresponding to the velocity of light in air with $n_{ground} = 1.0003$. We also plot as dotted line the $\Delta\beta$ obtained from $\gamma = 60$, corresponding to the average electron energy. The simulated curve (thick full line) is considerably below this dashed and the dotted curves, which means that the velocity of the average positions is larger than c/n_{ground}, it is also larger than the velocity of the average electron. The simulated velocity is even (slightly) larger than c. This is due to the fact that matter is moving on the average from inside (small r) to outside (large r), and the average $\bar{h}$ decreases with decreasing distance r. But the effect is small, the deviation of the shower velocity from c is less than 1/1000. We will ignore the small time dependence for the moment, and

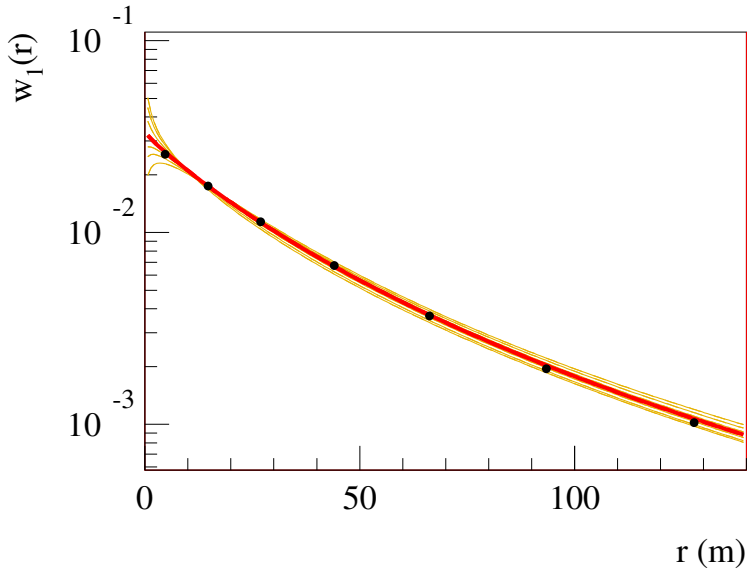

Figure 4.6: The radial distribution $w_1(r)$. The thin lines correspond to different times, the points represent an average, and the thick line corresponds to a fit (see text).

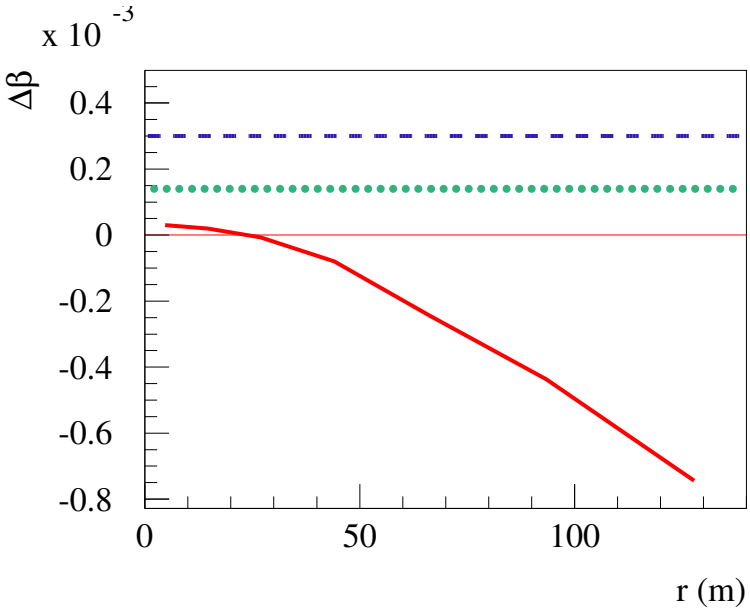

Figure 4.7: The longitudinal velocity difference $\Delta\beta$ versus r. We show the results for realistic simulations (thick solid line) and for $\gamma = 60$ (dotted line). Also shown: the value $1 - 1/n_{\text{ground}}$(dashed line).

consider in the following quantities at t'_{max}. To get some idea about the typical scales of the h-distribution $w_2(r, h)$, for a given value of r, we determine the mean value $\bar{h}$, as shown in Fig. 4.8. The mean value $\bar{h}$ is almost

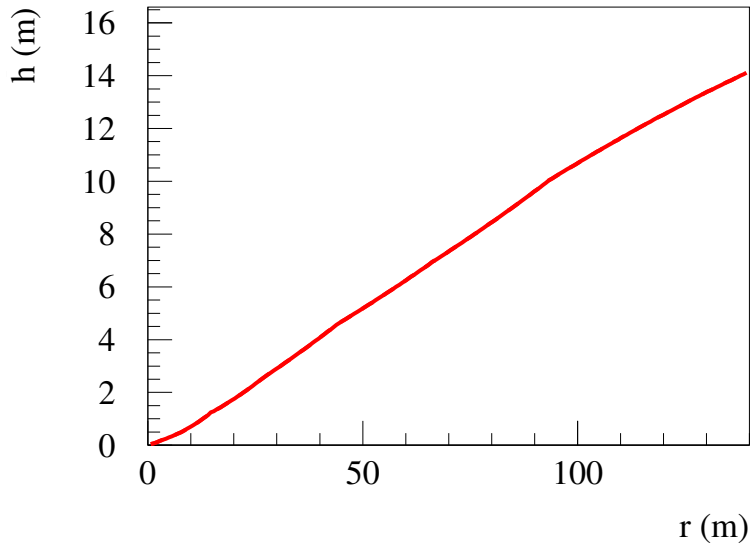

Figure 4.8: The mean value $\bar{h}$ for given values of the lateral distance r.

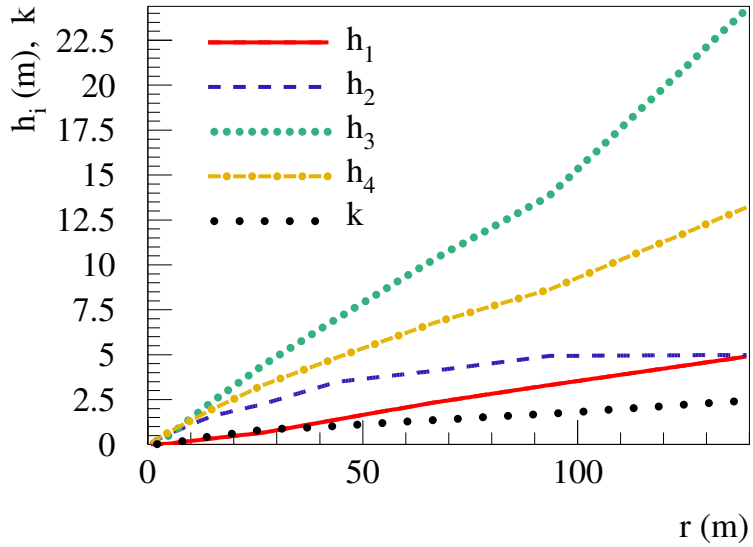

Figure 4.9: The parameters h_1, h_2, h_3, h_4, and k as a function of the lateral distance: h_1 (full line), h_2 (dashed line), h_3 (dotted line), h_4 (dashed-dotted line), k (wide-dotted line),

a linear function of the distance r, and for $r = 100$ m we get an average h of roughly 10 m. The w_2 distribution is obtained by fitting Monte Carlo

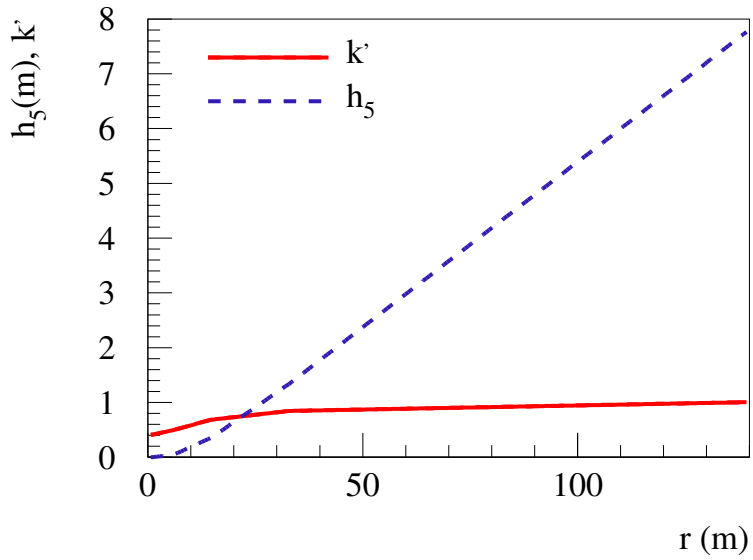

Figure 4.10: The parameters h_5 and k' as a function of the lateral distance: k' (full line) , h_5 (dashed line)

data in a range h between zero and $5\bar{h}$ for given r. We use

$$w_2(r,h) = \begin{cases} w_2^{MGD}(r,h) & \text{for } r > r_0 \\ w_2^{IGD}(r,h) & \text{for } r < r_0 \end{cases} , \tag{4.50}$$

with w_2^{MGD} being a "modified gamma distribution" of the form

$$w_2^{MGD}(r,h) = \frac{H(r,h)G(r,h)}{N(r)}, \tag{4.51}$$

with

$$H(r,h) = \Theta(h1-h)\left(2\left(\frac{h}{h_1}\right) - \left(\frac{h}{h_1}\right)^2\right) + \Theta(h-h_1), \tag{4.52}$$

and

$$\begin{aligned} G(r,h) &= \Theta(h_3-h)\left(h^{k-1}e^{-h/h_2}\right) \\ &+ \Theta(h-h_3)\left(h_3^{k-1}e^{-h_3/h_2}e^{-(h-h_3)/h_4}\right), \end{aligned} \tag{4.53}$$

with N being a normalization constant such that $\int\ dh\ w_2(r,h) = 1$. The function w_2^{IGD} is an "inverse gamma distribution" of the form

$$w_2^{IGD}(r,h) = \frac{(h_5)^{k'}}{\Gamma(k')}h^{-k'-1}e^{-h_5/h}. \tag{4.54}$$

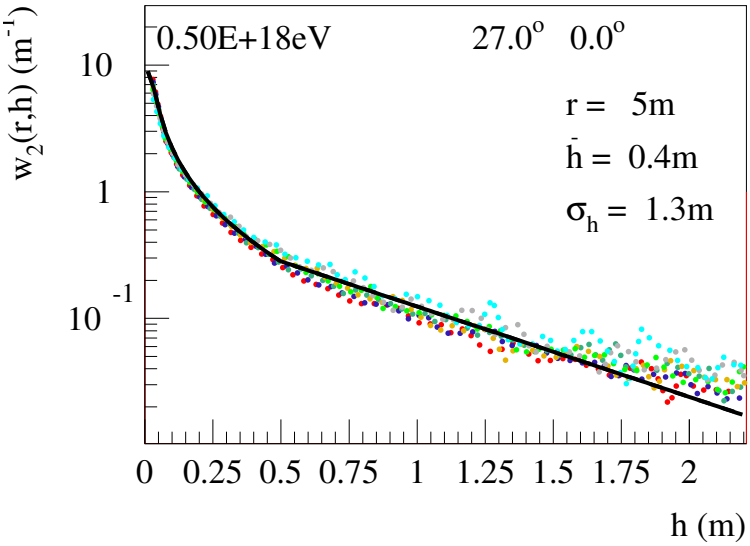

Figure 4.11: The distribution $w_2(r,h)$ for $r = 5\,\mathrm{m}$. The full black line represents the fit, the dotted lines are simulation results for different times.

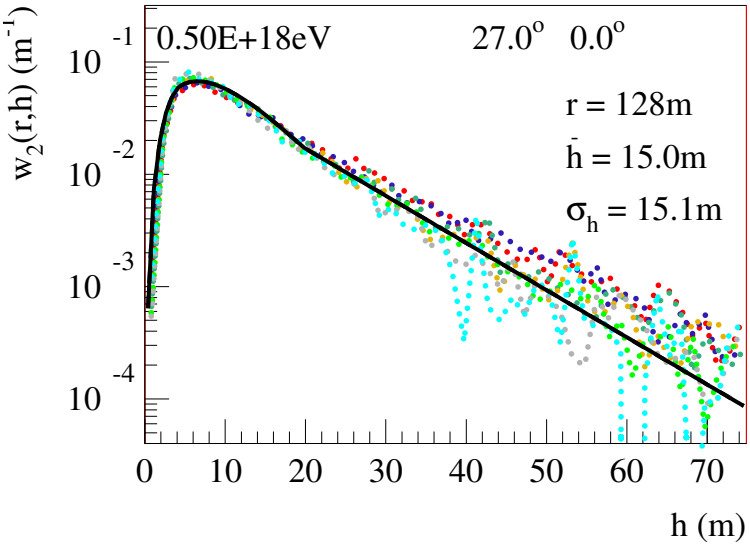

Figure 4.12: The distribution $w_2(r,h)$ for $r = 128\,\mathrm{m}$. The full black line represents the fit, the dotted lines are simulation results for different times.

We use $r_0 = 20$ m. The r-dependence is hidden in the parameters h_1, h_2, h_3, h_4, h_5, k, and k'. In Fig. 4.9 and Fig. 4.10, we plot the parameters,

as obtained from fitting the Monte Carlo data. All parameters grow with increasing distance r. Whereas h_2 seems to saturate, all the other parameters grow roughly linearly with r. With these parameters, we get good fits for h values up to five times the mean. In Fig. 4.11 and Fig. 4.12, we show the fits of w_2 together with Monte Carlo simulation results for different times. In Fig. 4.13, we show the fitted w_2 curves for three different values of r, conveniently plotted as $\bar{h}w_2$ versus $h/\bar{h}$ where one clearly sees the evolution of the shape with r. The reason to switch between w_2^{MGD}

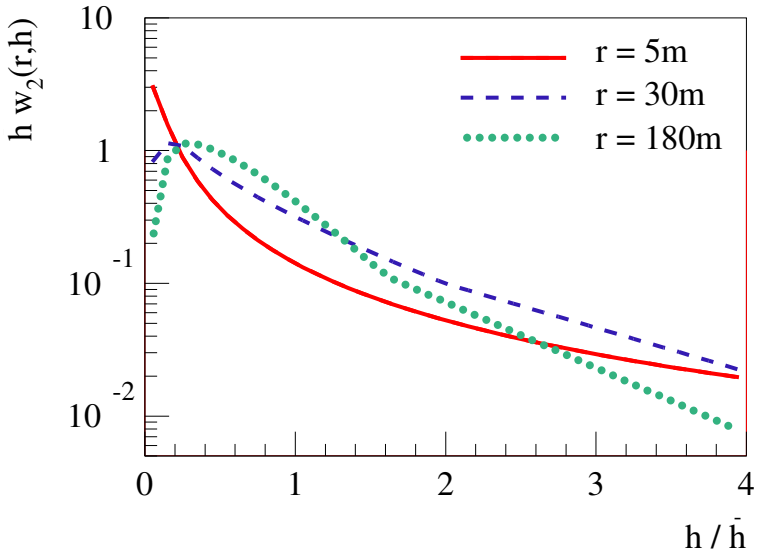

Figure 4.13: The distribution $w_2(r,h)$ for $r = 5\,\mathrm{m}$(full line), $r = 30\,\mathrm{m}$ (dashed line), and $r = 180\,\mathrm{m}$ (dotted line).

and w_2^{IGD} at $r_0 = 20$ m becomes clear from Fig. 4.11 through Fig. 4.13. From Fig. 4.13 it can be seen clearly that the particle distribution as obtained from the Monte-Carlo simulations behaves quite differently close to the shower axis compared to the distribution at large distances. This different behavior requires the use of different fit-functions in both regimes. At large distances from the core, the parametrization of w_2^{MGD} reproduces the Monte-Carlo result accurately. At small distances, it is important to have a smooth parametrization without jumps in the first derivatives, which is the case when using w_2^{IGD}. The above fit function w_2 leads to a delta-peak at $r = 0$. To still obtain numerical stability, a cut-off for the values k and h_5 is introduced such that the width of w_2^{IGD} is 1 mm. Since most of the particles are located at $r = \delta x^{\perp} = 1$ m from the shower axis, the path difference between signals emitted at this distance on both sides of the shower

axis acts as the important length scale in this regime. We estimate this path difference δR for a constant index of refraction equal to $n = 1.0003$: we have $\delta R \approx \frac{\partial R}{\partial x^\perp}\delta x^\perp \approx \sqrt{n^2\beta^2 - 1}\ \delta x^\perp \approx 3$ cm. Here we use that at the Cherenkov time (critical time for $h = 0$), we have $R^0 = n\beta x^{||}$, and $x_c^{||} = \sqrt{n^2\beta^2 - 1}\ x_c^\perp$ [91]. So a cut-off of $w_2^{IGD} \approx 1$ mm should give stable results. This has been tested numerically.

4.5 Results

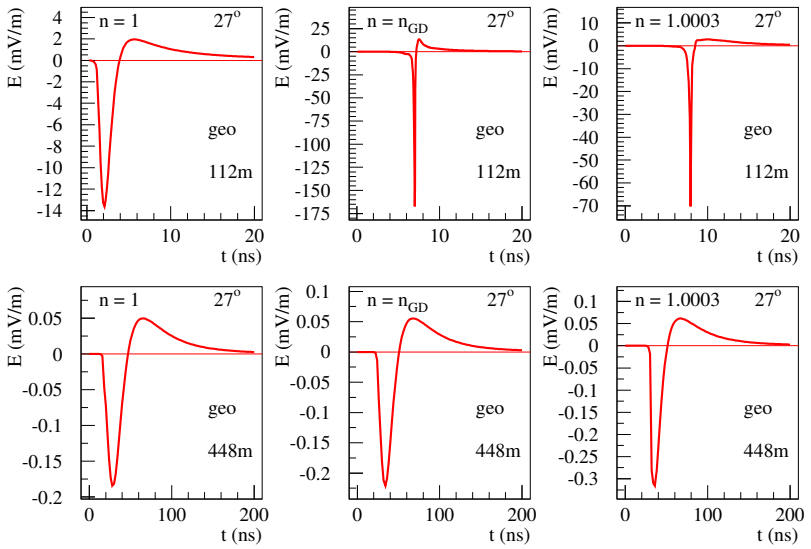

Figure 4.14: The y component of the geomagnetic contribution to the electric field as a function of the observer time t in ns, for an observer distance of 112 m (upper panel) and 448 m (lower panel) We compare different options for the index of refraction n, namely $n = 1$(left), $n = n_{\rm GD}$(middle), and $n = 1.0003$(right).

As already said, Eq. (4.18) and Eq. (4.19) are evaluated employing the EVA 1.0 package, which provides the weights w, the currents J, the denominators $\tilde{R}V$, and the integration procedures, as discussed in the previous section. We first consider the same "reference shower" (initial energy of $5 \cdot 10^{17}$eV, inclination 27^o) already discussed. We will distinguish between the geomagnetic contribution (caused by the currents due to the geomagnetic field) and the contributions due to charge excess. In Fig. 4.14 and Fig. 4.15, we show the results for the two contributions, for two different observer positions: 112 and 448 meters to the south of the impact point. We compare the realistic scenario ($n = n_{\rm GD}$) with the two "limiting cases"

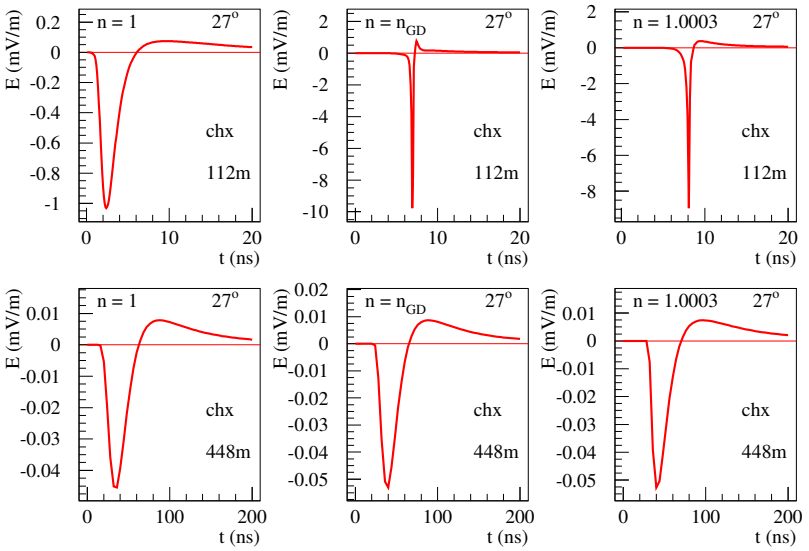

Figure 4.15: The x component of the charge-excess contribution to the electric field as a function of the observer time t in ns, for an observer distance of 112 m (upper panel) and 448 m (lower panel) We compare different options for the index of refraction n, namely $n = 1$(left), $n = n_{\rm GD}$(middle), and $n = 1.0003$(right).

$n = 1$ and $n = 1.0003$. One can clearly see big differences between the three scenarios, up to a factor of ten in width and magnitude. We also see, even in the realistic case ($n = n_{\rm GD}$), the appearance of "Cherenkov-like" behavior, with very sharp peaks. In Fig. 4.16 and Fig. 4.17, we consider a more inclined shower (70^o), for two different observer positions: 292 and 1170 meters to the south of the impact point. The differences between the realistic case ($n = n_{\rm GD}$) and the two "limiting cases" is even bigger: more than a factor of 100 in width and magnitude!

4.6 Geomagnetic Cherenkov radiation

As shown in the previous section, a realistic treatment of the index of refraction in the atmosphere appears to be crucial for the forms of the electromagnetic pulses. Can this be seen in experiments? What exactly should one look for?

To answer these questions we will have a closer look at the frequency spectra. As shown in Section 4.3, the fields are sums of terms of the form

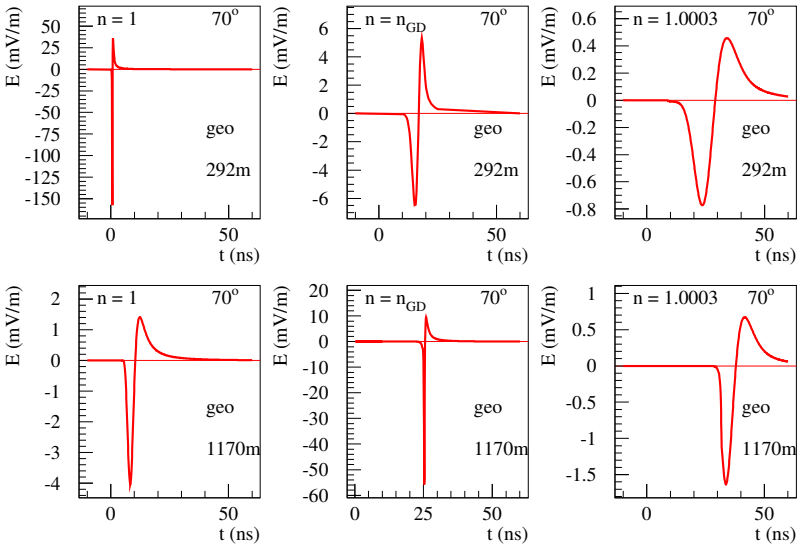

Figure 4.16: Same as Fig. 4.14, but here we consider a more inclined shower.

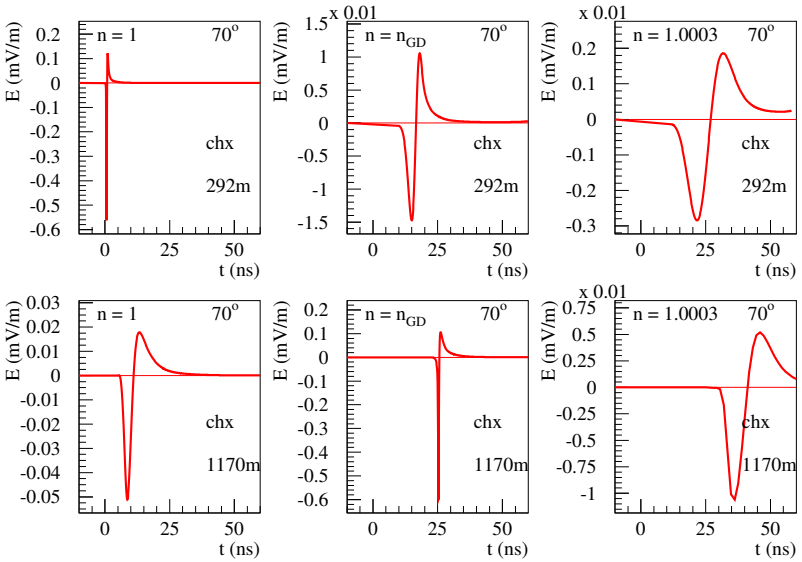

Figure 4.17: Same as Fig. 4.15, but here we consider a more inclined shower.

(up to factors)

$$\int dV \text{ pancake } \times \text{ currents } \times \left(\frac{dt'}{dt}\right), \tag{4.55}$$

where "currents" and "pancake" refer to respectively the point-like currents and the current distributions in the pancake, or its derivatives. The quan-

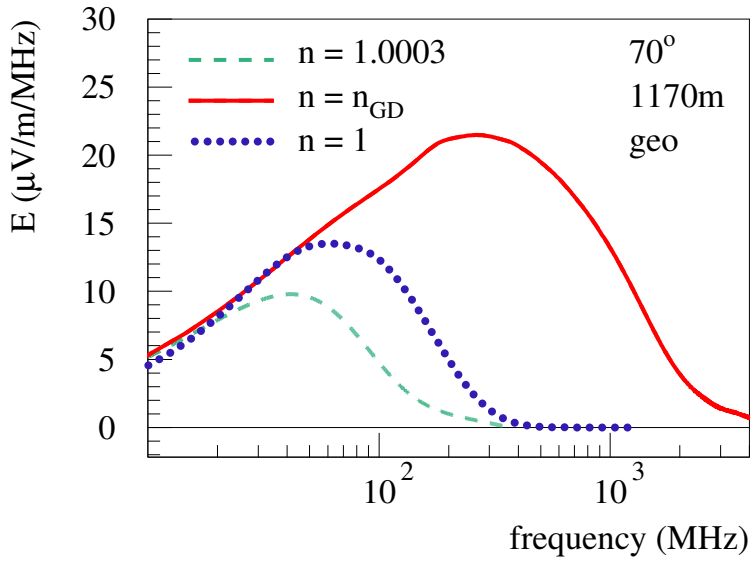

Figure 4.18: Fourier transform of geomagnetic component of the 70 degrees inclined shower observed at 1170 meters from the shower core. We plot the modulus of the Fourier transform.

tity dV is a pancake volume element. The currents and the "Cherenkov term" dt'/dt are taken at the retarded time $t = t'$, for a given observer time and position. Let us consider the evolution of an air shower in time t'. The currents are essentially proportional to the electron number $N_e(t')$ of the shower, the so-called "profile". We define t'_p to be the emission time (retarded time) corresponding to the profile maximum, also referred to as shower maximum. Another important quantity is the Cherenkov time t'_c, corresponding to the time where dt'/dt becomes singular.

The electric field contains terms governed by the derivatives of the currents, and therefore by the derivative of the profile. We consider therefore the expression "shower maximum" to represent the actual maximum of the profile or of its derivative.

A strong signal is expected when the two times t'_p and t'_c coincide. Such a situation is shown in Fig. 4.18, where we plot the Fourier spectrum for the geomagnetic component of the electromagnetic field for the 70 degrees inclined shower discussed in the previous section, with an initial energy of $5 \cdot 10^{17}$eV, and an observer positioned at a distance of $d = 1170$ m to the east of the impact point of the shower, corresponding to an impact parameter b of around 400 m. At this distance the shower maximum occurs at the Cherenkov time for a realistic index of refraction. The realistic case ($n = n_{GD}$) contains very high frequency components up to several GHz as

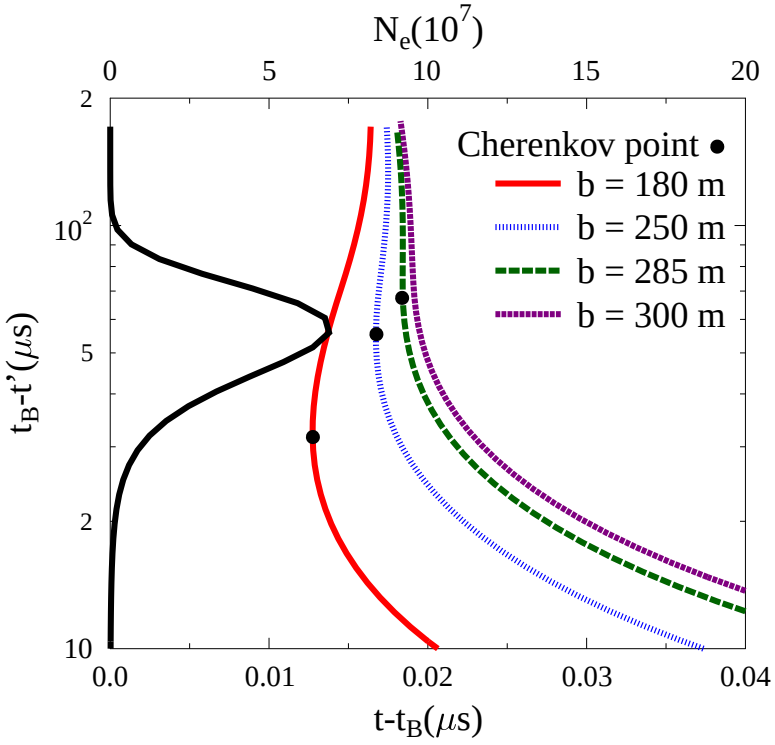

Figure 4.19: The shower profile as a function of t' (black line) and the retarded times t' as a function of the observer time t, relative to the time of closest approach t_B (red, blue, and magenta curves). The "Cherenkov points" correspond to the Cherenkov times (where dt'/dt is singular).

one would expect from the sharp peak in Fig. 4.16. The two limiting cases peak at lower frequencies, even below 100 MHz.

In the following, we discuss some very interesting features by taking the example of a 60 degrees inclined shower with an initial energy of 10^{17} eV, moving from west to east, in a magnetic field of strength 24.3μT and an inclination α of 54^o (Auger site). The observer is positioned to the east of the impact point. We will use the impact parameter rather than the horizontal distance (as in the examples before) to characterize the observer position.

In Fig. 4.19, we plot the shower profile N_e as a function of the retarded time t', and also the retarded times t' as a function of the observer time t, for three different choices of the impact parameter.

For large values of b (above 285m), like the case of 300 meters (magenta curve), there is no Cherenkov time, the function $t'(t)$ is single valued, and the derivative is always finite. We have "normal" emission, coming from around the the maximum of the profile corresponding to $t' = t'_p$, see Fig. 4.20. The form of the time signal is determined by the profile, we

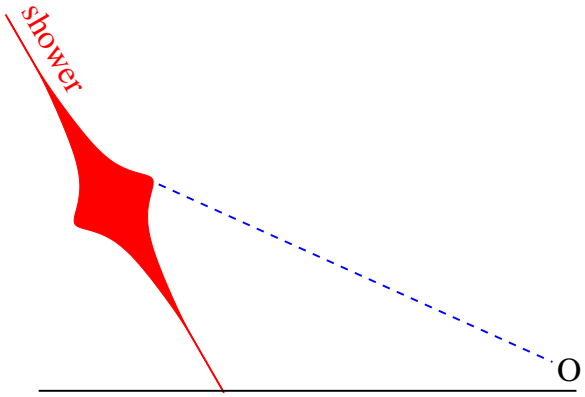

Figure 4.20: At large distance there is a unique relation between observer time and emission height. As indicated by the single dashed line the observer O receives "normal emission" from around the shower maximum.

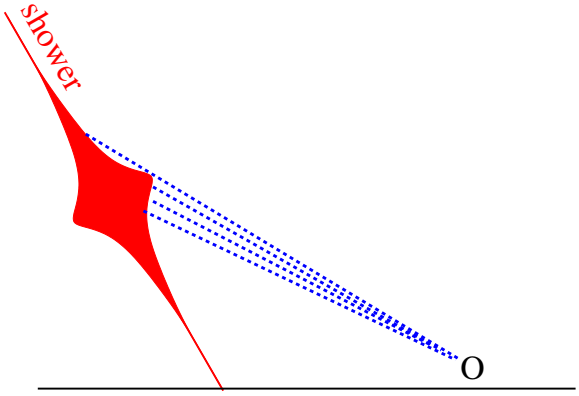

Figure 4.21: The signals emitted from a macroscopic part of the shower reach the observer simultaneously, the observer O observes "Cherenkov emission" from around the shower maximum.

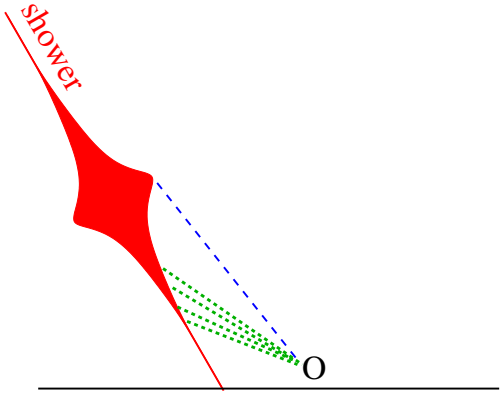

Figure 4.22: The observer O receives both "normal emission" from around the shower maximum and "Cherenkov emission" from later times.

expect maximum frequencies around few hundred MHz, as confirmed by the calculation shown in Fig. 4.23.
At impact parameters smaller than 285 meters, the function $t'(t)$ is double valued, so we we start observing a Cherenkov time. At 250 meters, the Cherenkov time coincides with the shower maximum, we have Cherenkov emissions from around the shower maximum. This means that due to $dt'/dt = \infty$, the emissions from a broad region around the maximum will be "compressed" and arrive almost at the same time at the observer, as sketched in Fig. 4.21. This leads to a strong and very short signal. Since the singularity is integrated over, as explained in Section 4.4, the actual width of the same signal is determined by the current distributions in the pancake, and we expect frequencies around a GHz, as confirmed by the calculation shown in Fig. 4.23.

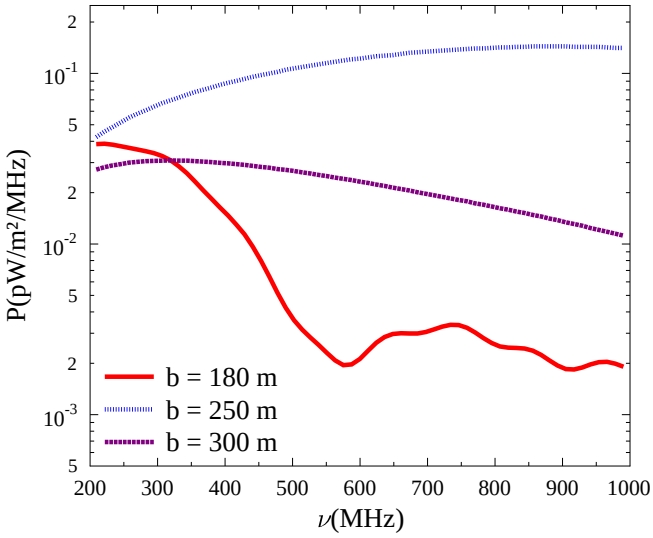

Figure 4.23: Flux densities for radio emission from a 10^{17} eV energy shower at 60^o zenith angle for impact parameters of 180, 250, and 300 meters.

If the observer is even closer to the shower, for example at an impact parameter of 180 meters, we still have a Cherenkov time, but this time is now significantly later than the shower maximum time (see the dot on the red curve in Fig. 4.19). Here we may have a very interesting situation: the observer may receive "normal" emission from around the shower maximum, but at the same time he may receive a significant contribution from much later, around the Cherenkov time, which again, due to the Cherenkov effect (signal compression), will be relatively strong and short (high frequency,

order of GHz). This situation is sketched in Fig. 4.22. The calculations in Fig. 4.23 show (as expected) two distinct peaks, one at small frequencies due to the normal emission from the shower maximum, and a second peak at high frequencies due to Cherenkov emission at much later times.
We thus predict not only high frequency components due to the geomagnetic Cherenkov effect, but in addition a double peak structure which reflects the simultaneous reception of signals from very different positions of the shower: "normal" emissions from around the maximum, and Cherenkov emission from much later times.

4.7 Comparing to data

The key result of the work presented in this chapter is the prediction of a sizable power emitted at higher frequencies, and a possible double peak structure with one peak at high frequencies. Furthermore, since these high frequency components occur only at the Cherenkov distance, upon applying a high-pass filter a clear Cherenkov ring should become visible in the LDF. The radius of this ring contains direct information on the shower maximum and thus the chemical composition of the original cosmic ray.
New experiments at the Pierre Auger observatory [54, 56], and LOFAR [57] should be able to measure the LDF in more detail, where first hints of "Cherenkov-like" effects in the LDF might have been observed [86, 92].
Emission at high frequencies (> 200 MHz) due to geomagnetic Cherenkov radiation might have been observed by the ANITA-collaboration [93], where pulses have been measured in the 200-1200 MHz band. Data published recently by the ANITA collaboration [71] shows the summed power of two cosmic-ray events for the range of 300-900 MHz.
In this measurement no indication is given of the arrival direction and the energy of the initiating cosmic ray, only that it most probably came from a relatively large zenith angle. The azimuth angle is unknown. Therefore also the air density along the path of the air shower is unknown, as well as its orientation with respect to the magnetic field. All this makes any quantitative comparison impossible. To get at least a qualitative understanding, we compare the data with the result of a simulation for a cosmic ray at a zenith angle of 60°, moving from west to east, in a magnetic field corresponding to the Auger site, with an observer east to the impact point, for various impact parameters b – the same situation as discussed in the previous chapter (changing the energy and the arrival direction of the cosmic ray will not change the qualitative discussion).
In Fig. 4.24, we compare the data with our simulation results. We show

blue curves corresponding to 350 - 225 m, from bottom to top for the leftmost value. The red curves refer to 200 - 180m, from top to bottom.
From the discussion of the last chapter, we easily understand the different theoretical curves: for large impact parameters 350, 325, 300m) we have the situation corresponding to Fig. 4.20: normal emission from around the shower maximum dominates. For impact parameters around 250 meters, we have Cherenkov emission from around the shower maximum, as in Fig. 4.21, and get strong signals at large frequencies (GHz). Then finally below 200 meters, we have the situation sketched in Fig. 4.22: a double peak structure due to simultaneously arriving signals from very different positions of the shower: "normal" emissions from around the maximum, and Cherenkov emission from later times.
Although energy and inclination of the measured showers are unknown, it is nevertheless clear that the data show a double peak structure very similar to what we predict.

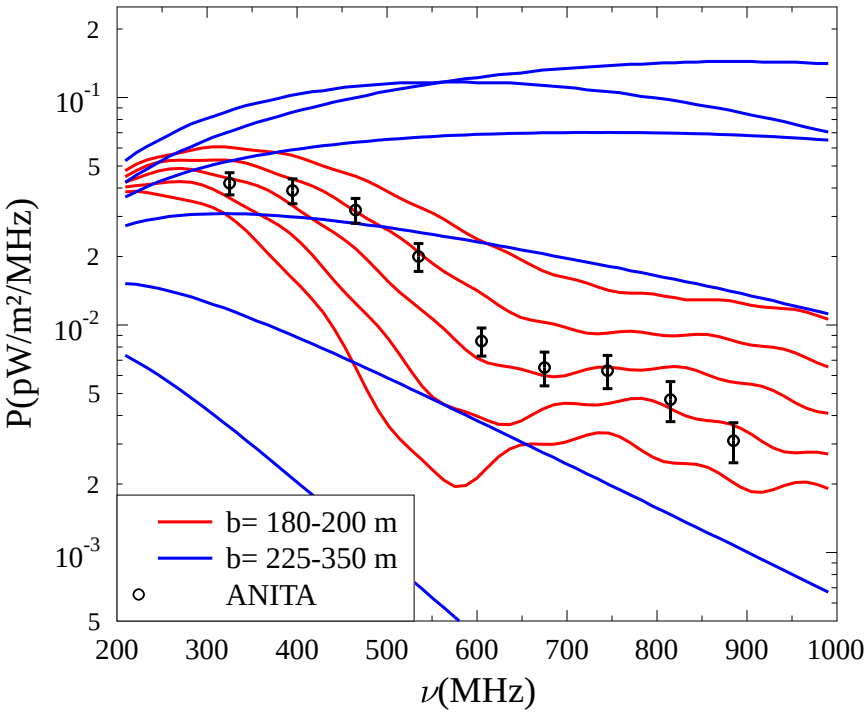

Figure 4.24: The predicted flux densities for radio emission from a 10^{17} eV energy shower at 60^o zenith angle for various impact parameters b are compared to the data for the sum of two events as measured by the ANITA balloon mission [71], where the data are taken from fig. 3 of that publication.

4.8 The emission mechanisms

The two main mechanisms contributing to radio emission, geomagnetic and charge excess, give a different polarization pattern. Where the geomagnetic emission is always polarized in the direction of the induced geomagnetic current, the charge-excess radiation has a radial polarization with respect to the shower axis [73, 94]. Evidence for the charge-excess component in air showers have been observed at the Pierre Auger Observatory [65] as will be discussed in the following chapter, and at the CODALEMA site [95]. Apart from an additional test of the Monte Carlo shower simulation, the importance of a thorough understanding of the charge-excess emission at distances where Cherenkov effects play a role lies in the fact that this is the main emission mechanism in dense media. This emission is thus crucial for experiments searching for GZK neutrino's through radio emission from showers induced in ice [96] or moon rock [97].
The maximum in the radio emission occurs at the observer distance where the shower maximum is seen at the Cherenkov angle. For geomagnetic emission, this is the maximum of the total electronic component, for charge excess this corresponds to the maximum in the electron-excess profile. These profiles do not necessarily peak at the same height and the Cherenkov peaks might be observed at different observer distances. Therefore, polarization analysis thus gives additional information about the relative peak position, X_{max}, of the total electronic component with respect to the charge-excess profile.
For the charge-excess analysis in [65, 98], and the one shown in Chapter 5, the variable R defined as

$$R = \frac{\vec{E}_x \cdot \vec{E}_y}{(E_x^2 + E_y^2)^{1/2}} \ , \tag{4.56}$$

is used. By definition the $\hat{x}$ direction is given by the projection of the geomagnetic component $\vec{e}_{geo} = -\vec{e}_\beta \times \vec{e}_B$ on the ground plane, where $\vec{e}_\beta$ is the unit vector pointing along the shower axis and $\vec{e}_B$ is the unit vector pointing in the direction of Earth's magnetic field. The $\hat{y}$ direction is given perpendicular to $\hat{x}$ in the ground plane. With this definition R vanishes independent of observer position if there would be no electric field component beside that of the geomagnetic emission. Since the charge-excess polarization is pointing radially inward from the observer position to the shower axis, R vanishes if the observer is positioned on the positive $\hat{x}$ axis, becomes negative moving to the $\hat{y}$ axis, goes to zero again on the $-\hat{x}$ axis, and becomes positive on the $-\hat{y}$ axis. It follows that if R is

plotted as a function of the observer angle ψ for a perpendicular incoming air shower with the magnetic field pointing to the north and ψ defined as $\psi = 0$ degrees for an observer positioned to the east of the impact point and $\psi = 90$ degrees for an observer positioned to the north of the impact point, a sinusoidal pattern should become visible if the geomagnetic emission is leading over the charge-excess emission which is generally the case. This

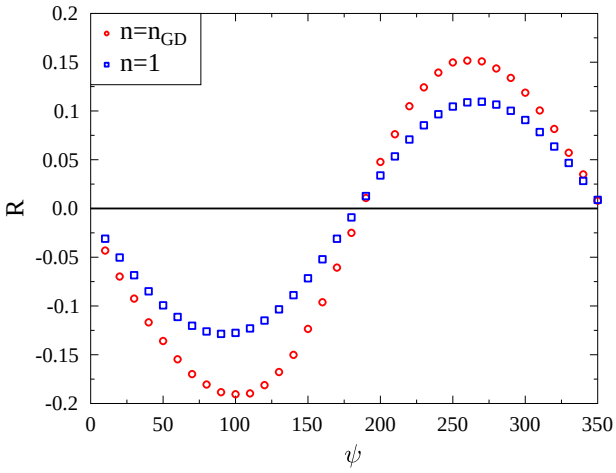

Figure 4.25: The value of R as defined in Eq. 4.56 as a function of ψ the observer angle in degrees.

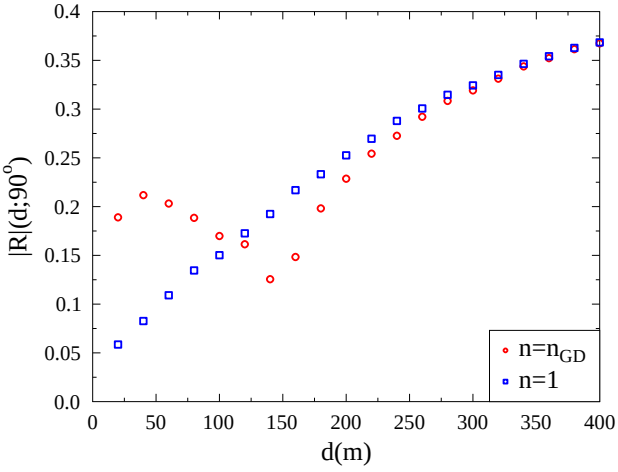

Figure 4.26: $|R|$ as defined in Eq. 4.56 at an observer angle $\psi = 90$ degrees as a function of distance from the shower axis d.

is shown in Fig. 4.25 for a 10^{17} eV shower for an index of refraction equal

to unity and also for a realistic index of refraction following the law of Gladstone and Dale, n_{GD}, given by Eq. (4.10) where $\rho(h)$ is the air density at an atmospheric height h. The observer distance $d = 75$ m is chosen in such a way that the shower maximum is observed at the Cherenkov angle for geomagnetic emission. For an index of refraction of unity we clearly observe a sinusoidal-like pattern. The differences in absolute value of R for $\psi = 90$ degrees and $\psi = 270$ degrees are due to statistical fluctuations. Since Cherenkov effects do not affect the polarization of the signal we do not expect the qualitative features of this pattern to change significantly for a realistic index of refraction. This is indeed the case as can be observed from Fig. 4.25. Nevertheless, even though the pattern does not change significantly, the maximum value of R increases.
This is also seen in Fig. 4.26 where we plot the absolute value of R at an observer angle of 90 degrees as a function of distance from the shower axis, $|R|(90°; d)$. Charge-excess emission scales with the opening angle with respect to the point of maximum emission. For an index of refraction equal to unity this is the opening angle with the shower maximum, which steadily increases with observer distance, and hence R also steadily increases with observer distance. For a realistic index of refraction the opening angle of maximum emission is equal to the Cherenkov angle and stays constant over the range of distances where Cherenkov effects are dominant. This is observed in Fig. 4.26 in the region below 140 meters.
The slope of the red circles and the dip at 140 meters can be understood from the fact that the charge-excess profile peaks closer to the surface than the total electronic component, as can be seen in Fig. 4.27, it follows that at 140 meters Cherenkov effects have diminished for the charge-excess component, but are still large for the geomagnetic emission and hence R becomes small. The slope of $|R|(90°; d)$ close to the Cherenkov distance is thus a clear signature for the relative position of the charge-excess maximum with respect to the maximum for the total electronic component. For distances larger than 140 meters, Cherenkov effects become small and the value of R for a realistic index of refraction converges to the value of R for a constant index of refraction equal to unity.

4.9 The lateral distribution function: The Cherenkov ring

Due to the extremely thin particle distribution close to the shower axis the electric field contains components at very high frequencies when the shower maximum is seen at the Cherenkov angle [70]. Away from the Cherenkov

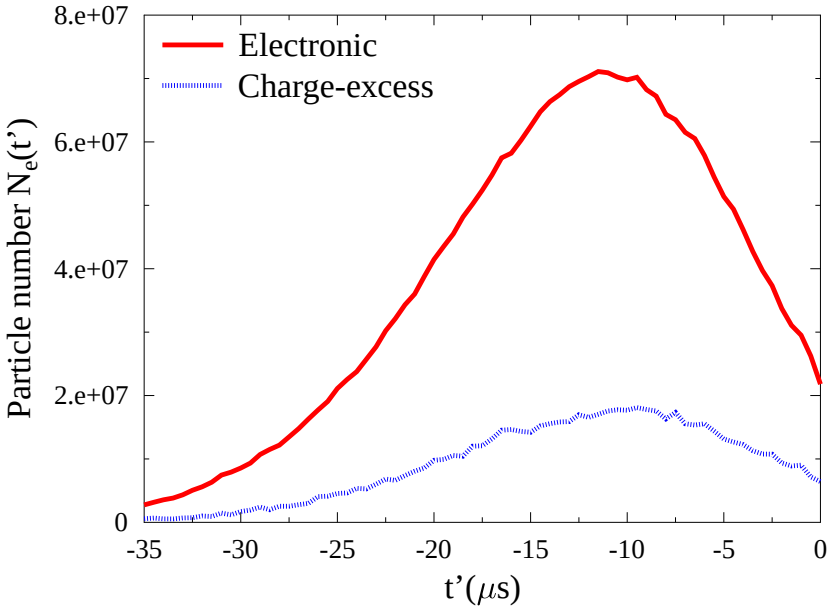

Figure 4.27: The total electronic component (full red line), and the charge-excess profile (striped blue line). The charge-excess profile peaks closer to Earth's surface than the total electronic component. The fluctuations in the profiles are due to thinning.

angle the emitted radiation from a finite length of the track is not seen at a single instant any more and the projection of the shower profile is the determining length scale. This is considered as the 'normal' varying current radiation, scaling with the derivative of the shower profile and limited to lower frequencies. This trend for the different frequency components is also seen in Fig. 4.28, where the LDF for the power,

$$P(\mu V^2/m^2/MHz) = \frac{\int_{\nu_1}^{\nu_2} E^2\ \nu\ d\nu}{(\nu_2 - \nu_1)}, \tag{4.57}$$

for different frequency bandwidths is shown for a typical 10^{17} eV proton shower. The LDF at low frequencies is naturally sensitive to emission on a rater long time scale, which is generally given by the 'normal' varying current emission and peaks close to the shower axis. For the higher frequencies the LDF becomes more sensitive for Cherenkov emission from close to the shower maximum and peaks further outward. In the $120 - 200$ MHz band, Cherenkov emission and normal emission compete with each other giving rise to a two peak structure.

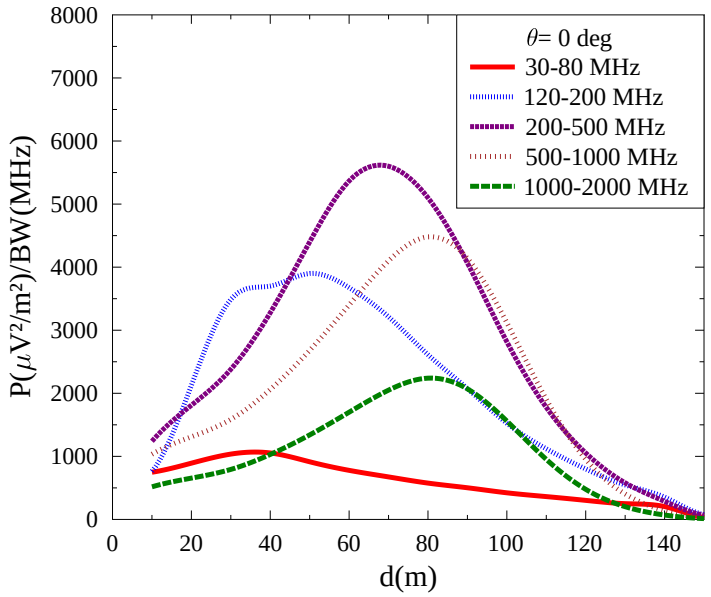

Figure 4.28: The LDF of the intensity divided by the bandwidth in different frequency regions.

4.10 Determining X_{max} from the radio signal

For an index of refraction equal to unity it was shown that one can distinguish between the chemical composition of different primary cosmic rays [63, 74]. This is due to the fact that at observer distances close to the shower axis the electric field is determined by the particle distributions in the shower front which do not differ significantly for proton and iron induced showers. At a large observer distances, on the other hand, the electric field is mainly determined by the shower profile, and thus also by X_{max}, the position where the particle number in the shower reaches a maximum. By taking ratios at different observer distances a handle on X_{max} is obtained. The X_{max} distribution is closely related to the chemical composition of the initial cosmic ray.

In this section we will show a similar ratio as well as a new, more direct procedure to yield accurate information about X_{max} when Cherenkov effects are taken into account.

In [91], it was noticed that the observer position d, through the Cherenkov angle is linked to the emission height along the shower axis, z, by

$$d_c = \sqrt{n^2\beta^2 - 1}\, z_c \,, \tag{4.58}$$

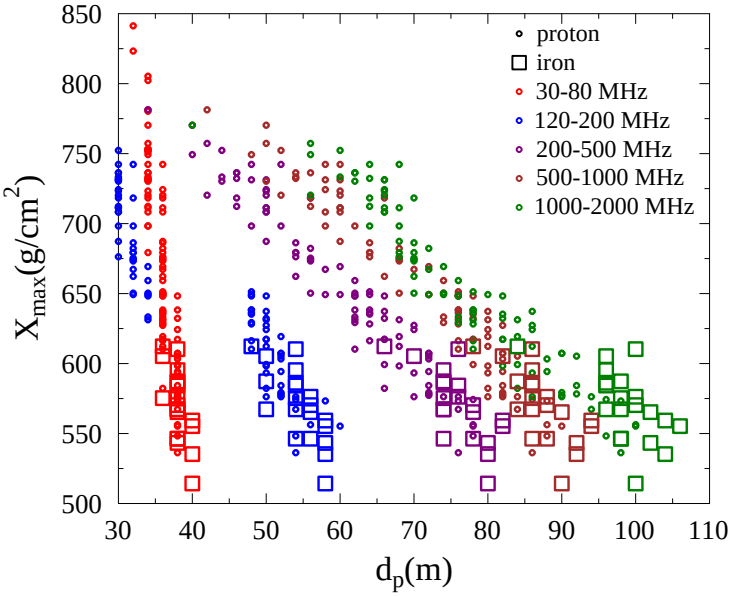

Figure 4.29: The value of $X_{max}(g/cm^2)$ as a function of $d_p(m)$ the position of the peak in the LDF for different frequency bands.

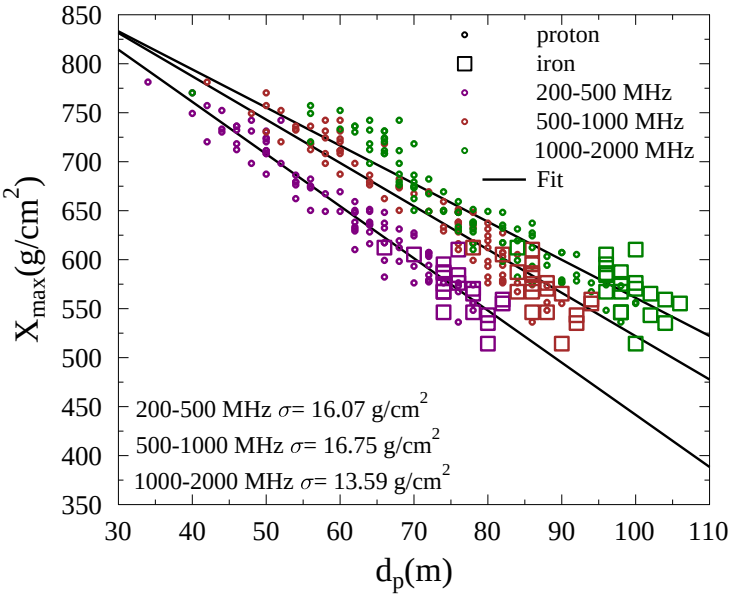

Figure 4.30: The value of $X_{max}(g/cm^2)$ as a function $d_p(m)$ fitted by Eq. 4.59. The standard deviation of the fit is of the order of $10 - 20$ g/cm^2

for a constant index of refraction n. In reality however, the index of refraction depends on altitude $n = n_{GD}$ following the law of Gladstone and Dale. To test if this can be used in realistic cases, we simulated the radio emission in EVA for a set of 100 proton and 20 iron perpendicular showers with an energy of $E = 10^{17}$ eV. For these simulations we determine the peak of the LDF for the power defined in Eq. (4.57), d_p, and the position of the shower maximum, z_m, that can be easily linked to X_{max}. In Fig. 4.29, we plot X_{max} as a function of d_p for different frequency bandwidths. From this figure it follows that X_{max} can be parameterized as

$$X_{max} = a + b \cdot d_p. \tag{4.59}$$

In Fig. 4.30, for the higher frequency bands (> 200 MHz) a fit with Eq. 4.59 is sufficient to obtain X_{max} with a precision of the order of $10 - 20$ g/cm^2. Cases with a peak position at distances less than 30 meters have been omitted from this analysis.
From Fig. 4.29 it is clear that for the low frequency bands (< 200 MHz), the sensitivity for X_{max} as a function of distance is small. For the $120-200$ MHz band a jump is observed in X_{max} as a function of distance. This jump is related to the two peak behavior in Fig. 4.28, and is due to the interplay between the normal radiation and Cherenkov emission. Following [63, 74] we plot in Fig. 4.31 X_{max} as a function of $Q^{BW}_{d2/d1}$ which is defined as

$$Q^{BW}_{d2/d1} = \frac{P^{BW}(\mu V^2/m^2/MHz; d = d2\ m)}{P^{BW}(\mu V^2/m^2/MHz; d = d1\ m)}, \tag{4.60}$$

the power in a fixed Band-With (BW) at distance $d = d2$ m divided by the power at a distance $d = d1$ m. This analysis is limited to bands at low frequencies (< 200 MHz). The simulations can be fitted with a logarithmic function given as

$$X_{max} = \alpha - \eta \log(Q^{BW}_{d2/d1}), \tag{4.61}$$

obtaining an accuracy of $\sim 15 - 20$ g/cm^2 using the ratio $Q^{30-80}_{300/100}$ in the $30 - 80$ MHz band at distances $d2 = 300$ m and $d1 = 100$ m, and the ratio $Q^{120-200}_{200/100}$ in the $120 - 200$ MHz band at distances $d2 = 200$ m and $d1 = 100$ m. The fit parameters a, b, α, η are given in Table 4.1 for the different fits.

4.11 Summary

In the first section a simple one dimensional model is used to obtain a good insight in Cherenkov effects and show that Cherenkov effects should play

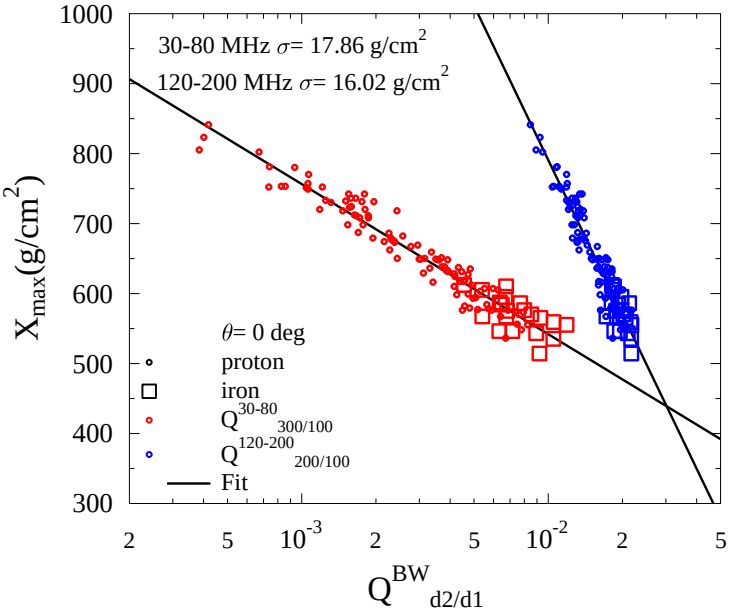

Figure 4.31: The value of $X_{max}(g/cm^2)$ as a function $Q^{30-80}_{300/100}$ and $Q^{120-200}_{200/100}$ for the low frequency bands ($<$ 200 MHz). The standard deviation of the fit is of the order of $15-20$ g/cm^2

Table 4.1: Fit parameters in Eq. (4.59), and Eq. (4.61).

Band-Width	scale parameter	slope parameter
30-80 MHz	α=112.8	η=93.2
120-200 MHz	α=-674.8	η=318.3
200-500 MHz	a=974.1	b=5.3
500-1000 MHz	a=964.1	b=4.4
1000-2000 MHz	a=949.7	b=3.9

an important role in the radio-emission from air showers. In the following section we presented a realistic calculation. The underlying currents are obtained from three-dimensional Monte Carlo simulations of air showers in a realistic geomagnetic field. The numerical procedures – simulations, fitting procedures, convolutions, referred to as EVA 1.0 – have been discussed. We showed that it is important to take into account for the density dependence of the index of refraction in air, given by the law of Gladstone and Dale. The new treatment leads in particular to strong emission at high frequencies (GHz). In certain cases, double peak structures are predicted, due to signals arriving simultaneously from different positions of the shower: "normal" emissions from around the maximum, and Cherenkov emission from later times.

In Section 4.8 we have shown that radio emission can be used to obtain relevant information about the emission mechanisms and the chemical composition. As examples we showed simulations for the observables R (Section 4.8) which distinguishes charge-excess and geomagnetic emission and Q (Section 4.10) which is sensitive to the mass of the cosmic ray. The parameter R is used to obtain the relative position of the charge-excess maximum with respect to the maximum of the total electronic component. Furthermore, it is shown that in the high frequency bands (> 200 MHz), X_{max} can be obtained directly from the position of the peak in the LDF with an accuracy of $10-20$ g/cm^2. In the low frequency bands (< 200 MHz) the parameter Q, which is a measure of the power at different distances from the shower axis, is used to obtain X_{max} with an accuracy of $15-20$ g/cm^2.

Chapter 5

Observation of the charge-excess effect in cosmic-ray-induced air showers

Part of this chapter is an adapted version of:

Observation of the charge-excess effect in cosmic-ray-induced radio pulses

E.D. Fraenkel[1], K.D. de Vries[1], W. Docters[1], O. Scholten[1], A.M. van den Berg[1]

GAP-2011-097, Pierre Auger Collaboration internal Gap-Note.

[1]Kernfysisch Versneller Instituut, University of Groningen, 9747 AA, Groningen, The Netherlands

5.1 Introduction

There are two main emission mechanisms, geomagnetic and charge excess, for radio emission of cosmic-ray-induced air showers. As shown in the previous chapters these mechanisms can be separated by their polarization pattern. Where the geomagnetic polarization is uni-directional in the direction of the Lorentz force acting on the charged leptons in the shower, the charge-excess polarization is pointing radially inward. These theoretical results were the basis of the charge-excess analysis developed for air showers measured at the Pierre Auger Observatory. In this chapter we first describe the different experimental set-ups that are used for the analysis, followed by a detailed discussion of the analysis chain. Finally, a direct comparison between theory and measurement is given and the results are discussed.

5.2 The Pierre Auger observatory

The Pierre Auger Observatory is the largest cosmic-ray detector on Earth. It spans a total area larger than 3000 km^2 and is located on the Pampa Amarilla in Argentina. The main purpose of the observatory is the detection of ultra-high-energy cosmic rays in the energy region above 10^{18} eV. At the Pierre Auger Observatory several different detection methods are used complementary to each other. The main detectors are the Surface Detector (SD), and the Fluorescence Detector (FD). The SD consists out of 1600 water tanks with a spacing of 1.5 kilometers. These tanks measure Cherenkov light from charged shower particles hitting Earth's surface and thus the tanks. The four FD stations each having several cameras, measure the ultra violet light that is emitted when charged particles in the shower interact with nitrogen in the atmosphere. In Fig. 5.1 one of the SD tanks is shown together with the FD detector at the Los Leones site in the background. Next to the two main detection systems several other techniques are under development. One is AMIGA [99] consisting out of underground muon detectors. There are several radio detection experiments such as AMBER, EASIER and MIDAS [100] measuring radio signals up to very high frequencies in the GHz range, while the AERA set-up is measuring in the MHz regime.

Figure 5.1: The Los Leones fluorescence telescope with on the foreground one of the water tanks of the surface detector at the Pierre Auger Observatory.

Figure 5.2: One of the LPDA's at the MAXIMA set-up.

5.3 Radio detection at Auger in the MHz regime

Results at the LOPES [49, 50] and CODALEMA [51, 52] experiments triggered plans for a larger array of radio antennas at the Pierre Auger Observatory. Using the existing infrastructure of the observatory in 2005 several

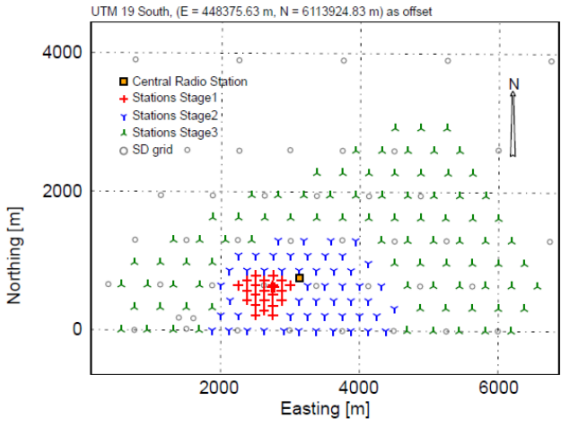

Figure 5.3: The layout of the AERA set-up.

prototype set-ups were installed such as the MAXIMA set-up close to the Baloon Launching Station (BLS) (see Fig. 5.2 for one of the Log Periodic Dipole Antennas, LPDA's, at one of the prototype set-ups), and the Rauger set-up [53, 54, 55].
Initially these set-ups were used for self-trigger and noise studies. Already in 2007 the first radio signals from cosmic rays were detected using plastic scintillator plates for trigger information. In a later stage also self-triggered events were measured [101]. At the same time experiment and theory were linked by the development of the radio extension to the Auger Offline [102] package. These developments lead to the construction of the Auger Engineering Radio Array (AERA) [101] which started in 2009. The AERA site is a 20 km^2 radio array that consists out of three parts. The layout of the site is given in Fig. 5.3. For the analysis in this chapter we will use data from the prototype set-ups and AERA phase one consisting of 24 antennas.

5.4 Data analysis: The Auger Offline package

Along with the construction of the AERA site, the Auger Offline package has been developed [102]. The Offline package is an analysis tool that makes it possible to process data from SD, FD, and radio detectors in one framework. The advantage is that a hybrid analysis can be done using the different detectors. The radio functionality in Offline can be divided into two separate data structures, the Stations and the Channels. The Station data structure contains information about the electric fields as measured at the antenna without any detector information except for its position and band-width. The Channel data structure on the other hand contains

the information from the measurement, such as the ADC voltages. The Offline package is build in such a way that one can easily go back and forward between the Station and Channel levels.
The "data" from Offline can be read from different sources, among which the MGMR and EVA simulations. After the read-in, analysis can be performed through a "module sequence" which is given in XML syntax. The main purpose of these analysis procedures concerning MGMR and EVA is the possibility to have a quantitative comparison with the measured data. There are several standard modules available to reach this goal, for example a band-pass filter, up-sampling of data, re-sampling of data, filtering, etc. Furthermore, a detailed simulation of the detector response is included.
For the charge-excess analysis described in this chapter, MGMR simulations are used. The input of the simulations (arrival direction, energy, etc.) is obtained from the SD. Since this analysis is done on the Voltage or Channel level, the detector response needs to be included, as well as a discretization of the time series. The analysis scheme is shown in Fig. 5.4.

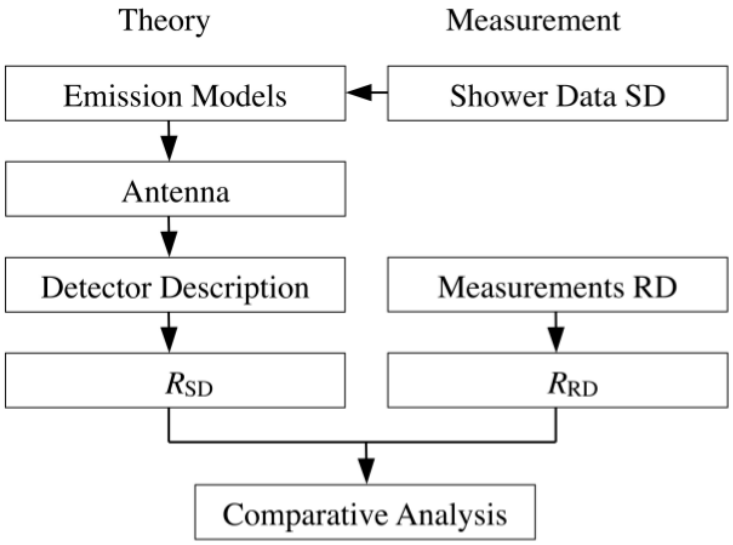

Figure 5.4: The analysis scheme used for the charge-excess analysis.

5.5 First hints of the charge-excess effect in cosmic-ray-induced air showers

For the charge-excess analysis the R parameter is used. In Section 4.8 a short introduction into this parameter was given for a simplified geometry.

For a comparison with real data the definition becomes slightly more complicated. The geomagnetic emission scales with the Lorentz force acting on the electrons and positrons in the shower front,

$$\vec{E}_{geo}(\vec{x},t) \propto -\vec{v} \times \vec{B} \propto \sin(\alpha), \tag{5.1}$$

where $\vec{v}$ is the shower velocity, $\vec{B}$ the magnetic field and $\sin(\alpha)$ the opening angle between the shower axis and the magnetic field. In general the direction of the geomagnetic polarization is in the direction of the Lorentz force. Therefore, we redefine our coordinate system in such a way that the $-\hat{x}$ direction is equal to the direction of the geomagnetic current projected on the ground plane, see Fig. 5.5 a). The simulated data is now processed through Offline following Fig. 5.4. The raw electric field values are converted to time sampled voltages $V_{xi}(\vec{x})$ and $V_{yi}(\vec{x})$. Where $\vec{x}$ is the observer position and i denotes the sample number. At this point the Hilbert transform [103], is added as the imaginary component of the signal, and the observable R is now defined as,

$$R(\psi) = \frac{2\sum_i Re(V_{xi}V_{yi}^*)}{\sum_i(|V_{xi}|^2 + |V_{yi}|^2)}, \tag{5.2}$$

where the observer dependence $\vec{x}$ is dropped. The observer angle ψ is defined as the angle between the observer and the $\hat{x}$ direction in the ground plane (see Fig. 5.5 a)). As noted the geomagnetic emission and thus the value of R depends on the opening angle of the shower axis and the magnetic field. To see this effect the value of R is plotted for all 124 scintillator triggered radio events in coincidence with the SD at the prototype set-up measured in May, June and July 2010. This is shown in Fig. 5.5 b) for MGMR simulations of all four antennas at the MAXIMA set-up. From Fig. 5.5 b) it clearly follows that the value of R at a fixed observer angle fluctuates over a rather large range, nevertheless we still observe a clear sinusoidal pattern.

For a direct comparison between data and MGMR simulations, the measured radio events in the period of May, June and July 2010 are used. At the 20'th of May, the antennas have been realigned and we will thus only consider data taken after this date. After selecting events with a signal-to-noise (S/N) ratio larger than two, defined by the power in the measured pulse divided by the power in a region in the same trace where only noise is measured, 53 out of 107 measured coincidences with the SD remain. Even though the analysis is done using the Auger Offline package, the SD reconstruction of these events is done using CDAS [104]. In a later stage it has been assured [105], that the reconstructed core positions with Offline and

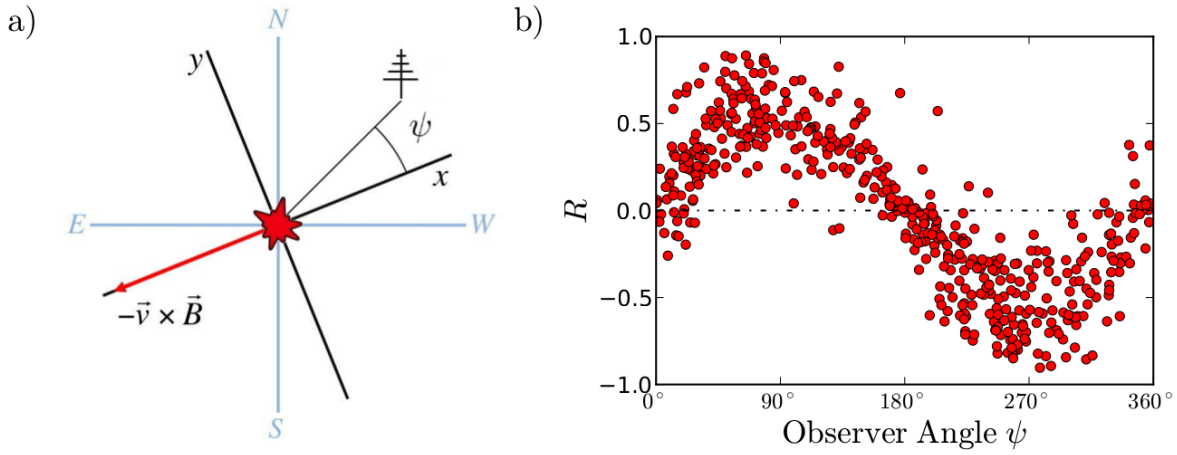

Figure 5.5: a) The coordinate system is rotated such that the geomagnetic emission is polarized in the $-\hat{x}$ direction. The observer angle is defined from the $\hat{x}$ direction to the $\hat{y}$ direction. b) R as a function of observer angle ψ for a set of 124 showers simulated with MGMR for all four MAXIMA antennas.

CDAS do not deviate significantly. For six events the deviation is larger than 100 meters, these events have been excluded from the analysis. The effect of including these events turned out to be negligible.

Another uncertainty may arise due to thunderstorms. Since for the used events there is no thunderstorm data available, no cuts have been made to exclude events that have been measured during thunderstorms.

The reconstructed SD parameters are used as an input for MGMR. The error in the SD reconstruction is now propagated through the MGMR simulation by simulating each event 100 times varied within the errors of the SD parameters. The error in the radio signal is obtained by means of the double-noise method described in [106]. The antenna and detector response are taken into account for by Offline, and the resulting voltages are used for a direct comparison with data. In MGMR there is the possibility to switch off the charge-excess emission. To check the no charge-excess hypothesis the analysis is also done for MGMR simulations without charge-excess emission.

In Fig. 5.6, the results are shown for both the zero-hypothesis where no charge excess is included into the simulations, top Fig. 5.6 a) and b), as well as the simulations with charge excess, bottom Fig. 5.6 c) and d). The left figures a) and c) show the measured value of R as a function of the simulated value, and the figures on the right b) and d) show the value of R as a function of the observer angle ψ.

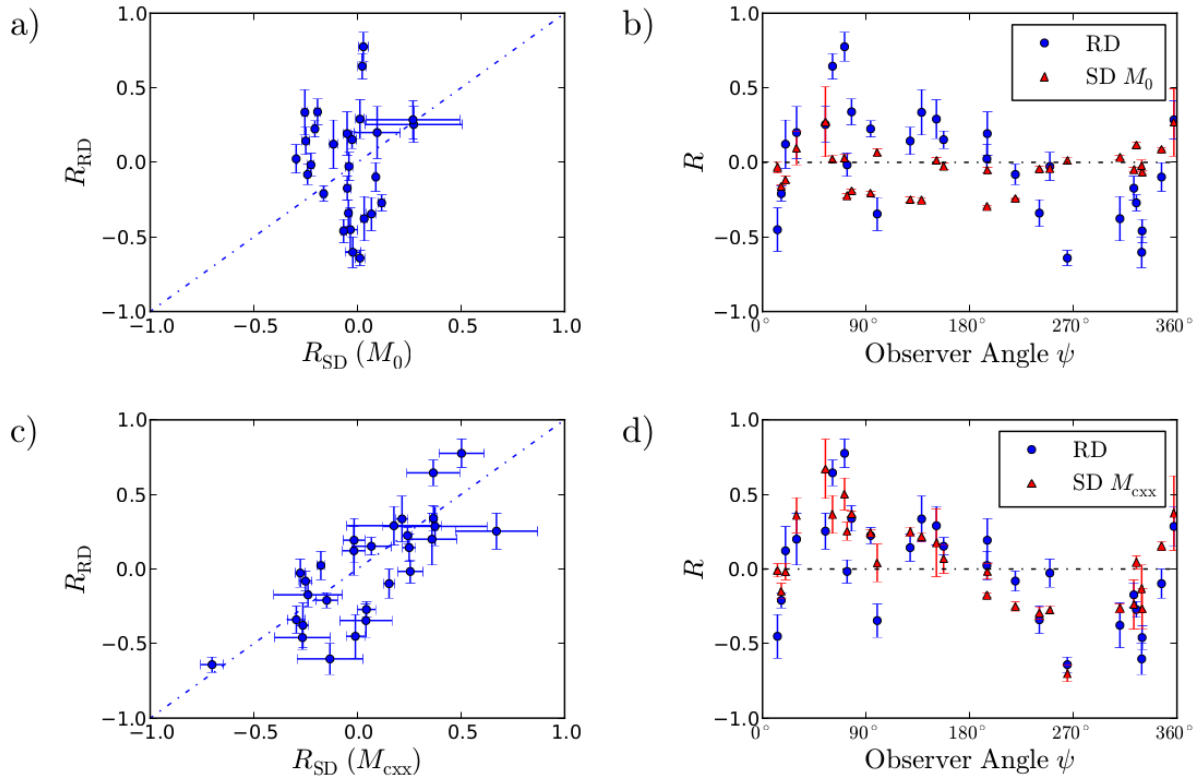

Figure 5.6: a) The measured value of R_{RD} as a function of the simulated value R_{SD} for the no charge-excess hypothesis. The dotted black line is given by $R_{RD} = R_{SD}$. b) The measured R_{RD} (blue circle) and the simulated R_{SD} for the no charge-excess hypothesis (red square) as a function of the observer angle ψ. c) The measured value of R_{RD} as a function of the simulated value R_{SD} for the charge-excess hypothesis. d) The measured R_{RD} (blue circle) and the simulated R_{SD} for the charge-excess hypothesis (red square) as a function of the observer angle ψ.

From Fig. 5.6 it can already be concluded that we see a strong hint for the charge-excess contribution. To quantify the charge-excess hypothesis, we can calculate the χ^2 value for both the charge excess as well as the no charge-excess hypothesis. The χ^2 value for a single event is defined as,

$$\chi^2_i = \frac{(R_{RD} - R_{SD})^2}{\sigma^2_{RD} + \sigma^2_{SD}}, \tag{5.3}$$

and the total and reduced χ^2 values are now obtained by,

$$\chi^2 = \sum_{i=1}^{D} \chi^2_i.$$
$$\chi^2_{red} = \chi^2/D. \tag{5.4}$$

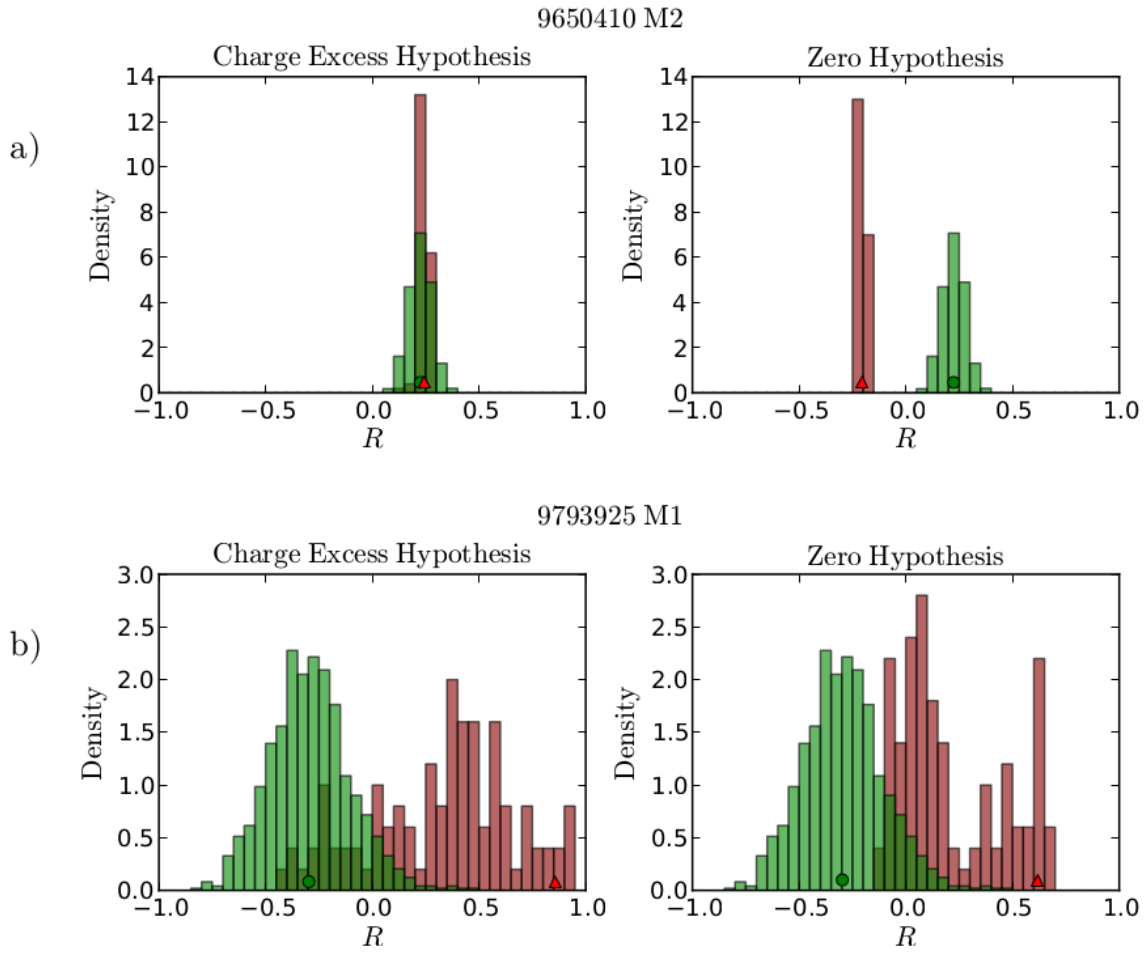

Figure 5.7: Examples of the histograms obtained for R including the RD measurement errors and the propagated SD errors. The histograms give the normalized density from which the Probability Distribution Function is obtained to calculate the normalized likelihood values. The errors used for the χ^2 analysis are given by the RMS of R as obtained from these histograms.

Where a χ^2_{red} equal to unity means that the model gives a good prediction of the data. By this definition of the χ^2 value, the errors are implicitly assumed to be Gaussian and obtained by taking the Root Mean Square (RMS), $\overline{(\bar{R} - R)^2}$ from the Probability Density Functions (PDFs) as shown in Fig. 5.7. In these histograms, the density of R is given in 40 bins for the SD varied simulations (green bars) and 975 RD values obtained from the double noise method (red bars). It has been tested that 40 bins is enough to give stable results. Since R is bounded, the propagation of the errors through the simulation is not linear. Furthermore, the radio data contains non-Gaussian components in the form of transients. This means

Table 5.1: The χ^2 (top) and standardized likelihood (bottom) values for the charge-excess hypothesis (left), the no charge-excess hypothesis (middle) and the Bayes factor (right).

a)	M_{cxx}		M_0		$B_{0,cxx}$
	χ^2	χ^2/D	χ^2	χ^2/D	
	90	3.2	561	20.0	$1 \cdot 10^{102}$

b)	M_0		M_{cxx}		$B_{0,cxx}$
r	$-2\ln L$	$(-2\ln L)/D$	$-2\ln L$	$(-2\ln L)/D$	
0.1%	85	3	229	8.2	$2 \cdot 10^{31}$
1.0%	79	2.8	185	6.6	$1 \cdot 10^{23}$
5.0%	71	2.5	148	5.3	$3 \cdot 10^{16}$

that the assumption of Gaussian errors as done for the χ^2 analysis is an approximation. A better measure taking into account for non-Gaussianities would be the normalized likelihood value defined by,

$$-2 \text{ Ln } L_i = -2 \text{ Ln } \frac{\int p_{RD}(x) p_{SD}(x) dx}{max_z \int p_{RD}(x) p_{SD}(x+z) dx}, \tag{5.5}$$

which is a measure for the overlap of the underlying PDFs as shown in Fig. 5.7. In the case of Gaussian errors it can be shown that $-2 \text{ Ln } L_i = \chi_i^2$.

Due to the binning in the PDFs, it may occur that the numerator in Eq. (5.5) becomes zero and hence the logarithm diverges. To prevent this, each bin is assigned a constant value such that there is a chance of $r = 1\%$ that the data is obtained from a completely flat distribution. The method has been checked for different values of r. The results for a signal-to-noise cut of S/N = 3 are shown in Table 5.1. In Table 5.1 a), the χ^2 values are given for the charge-excess hypothesis (left) and the no charge-excess hypothesis (right). In Table 5.1 b), the standardized likelihood is given for three different values of r for both hypothesis. Furthermore, from the obtained likelihoods, the Bayes factor given by

$$B_{cxx,0} = \frac{\prod_{i=1}^{n} L(X_i|M_{cxx})}{\prod_{j=1}^{n} L(X_j|M_0)} \tag{5.6}$$

can be calculated. This equals $B_{cxx,0} = 10^{23}$ for $r = 1.0\%$, giving a clear proof ($B_{cxx,0} >> 100$) that the zero-hypothesis (no charge excess) can be rejected. Nevertheless, the χ^2 or standardized likelihoods for the charge-excess hypothesis are still larger than unity, and hence the MGMR model does not fit the data perfectly. There might be several reasons for this. During the measurement period thunderstorm conditions were not monitored which might give rise to outliers in the data. In general the quality

of the data is an issue that has to be considered, where a larger signal-to-noise cut might lead to a lack of statistics. From the model point of view, the errors are underestimated since shower-to-shower fluctuations have been neglected and the primary particle is considered to be proton. Furthermore, MGMR ignores Cherenkov effects where in Section 4.8 it was already shown that at distances where Cherenkov effects play an important role there is a significant effect on the value for R. An even more interesting cause could be a missing radiation component that is up to now unknown.

5.6 Conclusions and Outlook

A detailed polarization study is performed using the so-called R parameter. From simulations a sinusoidal pattern is expected as a function of the observer angle ψ, which is clearly observed in the data. A more quantitative comparison shows that the zero-hypothesis using MGMR simulations where the charge-excess emission is switched off can be rejected. Nevertheless, the obtained χ^2 and standardized likelihood values are of the order 2-3 and hence the data is not fitted perfectly.
The next step would be a detailed comparison of the more realistic EVA simulations described in the previous chapter with the data. At the moment of writing this analysis is ongoing. In Fig. 5.8, we show preliminary results for R as a function of the observer angle ψ for the measured events at the prototype (MAXIMA) set-up measured in the period May 20th until June 29th 2011, and the AERA set-up measured in the period April 15th to Sep 15th 2011. In Fig. 5.9 the same analysis is shown for MGMR simulations. It clearly follows that, after applying filtering and including the detector response, the differences between EVA and MGMR become very small. This is to be expected, since the main difference between both approaches lies in the treatment of Cherenkov effects which are less prominent in the $30 - 80$ MHz band for which the analysis is done.

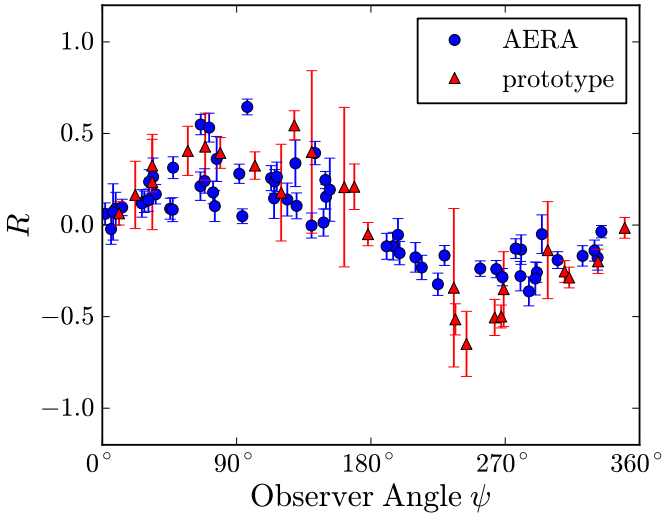

Figure 5.8: R as a function of the observer angle ψ for EVA simulations of measured events at the prototype (MAXIMA) set-up (red triangles) and the AERA set-up (blue circles). Figure from E.D. Fraenkel.

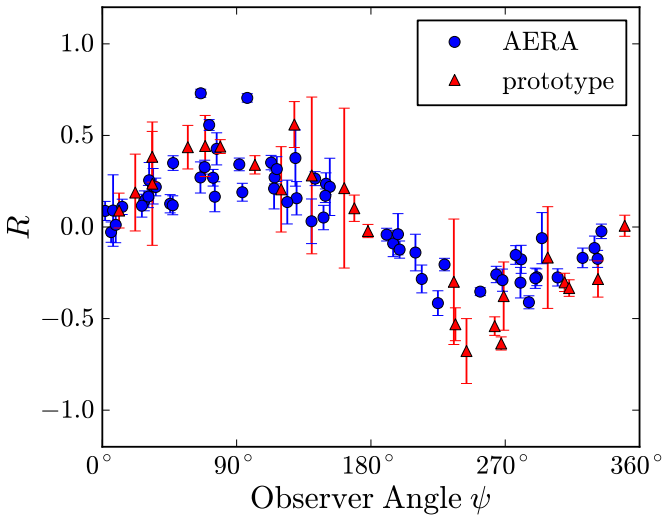

Figure 5.9: R as a function of the observer angle ψ for MGMR simulations of measured events at the prototype (MAXIMA) set-up (red triangles) and the AERA set-up (blue circles). Figure from E.D. Fraenkel.

Chapter 6

Summary and outlook

This thesis deals with the macroscopic modeling of radio emission from cosmic-ray-induced air showers. The main radio emission mechanism is due to the deflection of electrons and positrons in Earth's magnetic field. This mechanism, originally proposed by Kahn and Lerche [45], gives rise to a net transverse current in the shower front. The variation of the vector potential induced by this transverse current leads to coherent electromagnetic radiation. As predicted by Askaryan [44], due to several processes like Compton scattering and knockout of atomic electrons by particles in the shower there will be a net electron excess in the shower front which gives rise to a second emission mechanism. Coherence is typically reached over the dimensions of the shower which in early stages of this thesis work was thought to be of the order of meters. Hence the emission is coherent in the MHz radio regime.

In Chapter 2 the Macroscopic Geo-Magnetic Radiation (MGMR) model is discussed. It is found that a reformulation of the mathematical expressions lead to more stable numerical results in the regime of small impact parameters. The physical interpretation behind the different description lies in the different length scales which are seen by the observer. For observer distances far away from the shower axis (> 500 m) the shower front can be considered point-like and the electric field is fully determined by the projection of the shower profile toward the observer. On the other hand, for observers positioned close to the shower axis, since the signal in this case travels along with the shower, the electric field is fully determined by the shape of the shower front.

In section 2.5 the two main emission mechanisms, geomagnetic and charge excess, are discussed. It is shown that they can be separated by their polarization pattern. Where the geomagnetic emission is always polarized in the direction the Lorentz force acting on the particles, the charge-excess emission is polarized radially inward, in the direction of the observer to-

ward the shower axis. It follows that depending on the observer position both mechanisms can interfere. This is reflected in the Lateral Distribution Function (LDF) which is shown to be dependent on the angle of the observer with the shower core. The hybrid extension of MGMR is discussed in section 2.6, where several free parameters in MGMR are fitted using Monte Carlo simulations. The pancake thickness parameter L which is a measure for the size of the shower front is obtained and fixed to $L = 3.9$ meters. The fraction of charge excess in the shower is also simulated and fixed to its value close to the shower maximum of $C_x = 0.23$. Furthermore, in the hybrid mode the shower profile is obtained directly from Monte Carlo simulations. Using the hybrid mode, in section 2.7 it is shown that the radio signal can be used to distinguish between proton and iron induced showers. As mentioned, observers positioned close to the shower axis are mainly sensitive to the shower front which does not differ significantly for proton and iron induced showers. Observers positioned far away from the shower axis, however, are mainly sensitive to the shower profile. Since for iron induced showers the profile peaks higher in the atmosphere than for proton induced showers the observer at these distances becomes thus sensitive to the chemical composition of the initial cosmic ray. It is shown that the power ratio of signals close and far from the shower axis can be used to distinguish between proton and iron induced showers on average.

When MGMR [62, 63] was developed a huge difference between the macroscopic MGMR model and the microscopic models in time domain like REAS [61, 82] became apparent. In Chapter 3 the differences between both approaches are discussed in detail. First it is shown how the addition of a missing radiation component in the microscopic models, namely the emission due to the start and end-points of the particle tracks, resolved the major part of the differences with the macroscopic approach. It is shown that both REAS3 [72] and MGMR predict similar emission patterns. It is also shown that the remaining differences between REAS3 and MGMR are mainly due to the different treatment of the particle distributions in the shower front.

The simulations discussed so-far were done for an index of refraction of air equal to unity. In reality the index of refraction deviates from unity. Even though this deviation is small $O(10^{-4})$ in Section 4.1 it is argued that Cherenkov effects play a role in the emission at intermediate observer distances from the shower axis of the order $100 - 200$ m. In the following Section 4.2 we discuss how Cherenkov effects can be linked to a divergence in the vector potential. A more intuitive interpretation is given by linking the denominator of the vector potential which contains a singularity at the Cherenkov point, to the derivative of the emission time with respect to

the observer time. When Cherekov effects occur this derivative diverges, hence signals over a finite part of the shower profile arrive simultaneously at the observer. The remaining length scale to determine coherence is the projected size of the shower front. We show how to solve for this divergence by using the finite dimensions of the shower front. The derivatives acting on the denominator in the vector potential are shifted to the particle distributions in the shower front leaving only a square-root divergence in the electric field which is now safely integrated. The obtained expressions for the electric field are implemented in the Electric fields, using a Variable index of refraction in Air shower simulations (EVA) code described in Section 4.3. From full Monte Carlo air shower simulations it is noticed that most of the particles are located in a very thin disc close to the shower axis. This disc has a typical size of the order of centimeters or less. Therefore coherence is expected at extremely high frequencies in the GHz range. EVA simulations show the importance of including Cherenkov effects in the radio emission. A huge difference is observed with simulations done for an index of refraction equal to unity. At the Cherenkov angle the emission is shown to indeed contain high frequency components in the GHz range. Another interesting feature occurs when at the Cherenkov angle a part of the shower below the shower maximum is observed. The part of the shower which is beamed due to Cherenkov effects contains a comparable amount of power to the larger part of the shower which is observed over a longer time scale. It follows that the frequency spectrum contains a two-bump structure which is a clear signature for Cherenkov effects which might have been observed by the ANITA experiment [71]. Due to Cherenkov effects the relative position of the shower maximum for the excess charge with respect to the total electronic component can be obtained by a polarization analysis. It is also shown that the LDF of the radio signal at different frequencies contains a clear Cherenkov peak. In the high frequency bands ($>$ 200 MHz) the position of this peak can be used to determine the position of the shower maximum with an accuracy of the order $10-20$ g/cm^2. For the low frequency bands ($<$ 200 MHz) a similar ratio as used for the MGMR simulations in Section 2.7 is given to obtain an accuracy of $15-20$ g/cm^2 for the position of the shower maximum.

In Chapter 5 the polarization analysis done at the Pierre Auger Observatory is presented. The two main emission mechanisms, geomagnetic and charge excess, can be separated by their polarization pattern. For the analysis the parameter R is defined. When charge-excess emission is included in the simulation R shows a distinct sinusoidal pattern for an observer going around the shower axis at a fixed distance. As shown in Section 5.5 this sinusoidal pattern is clearly observed in the data. A more quantitative

comparison of the R parameter as obtained from simulations and data is also given. For this comparison two methods are used, first there is the χ^2 analysis assuming Gaussian errors. Analysis for MGMR including charge excess gives a $\chi^2_{red} = 3.2$ compared to a value of $\chi^2_{red} = 20$ when charge-excess emission is left out of the simulations. Another analysis based on the standardized likelihood is shown to take into account for non-Gaussianities. A Bayes factor of $B_{cxx,0} >> 100$ is obtained, and hence the zero-hypothesis being that there is no charge-excess emission can be rejected.
In this thesis several new results are presented. The latest is the inclusion of Cherenkov effects into the simulation of radio emission from air showers. One of the first predictions is that due to these Cherenkov effects the LDF has a distinct peak [66]. The predicted LDF is seen in Fig. 6.1. This effect might have been observed by LOFAR [92] as can be seen from Fig. 6.2. Nevertheless, a more detailed comparison including charge-excess emission and a more realistic geometry is needed. The detailed understanding of the radio LDF is one of the challenges that lies still ahead, but will certainly be answered in future measurements at LOFAR, the Pierre Auger Observatory, and several other experiments that are being planned at the moment.

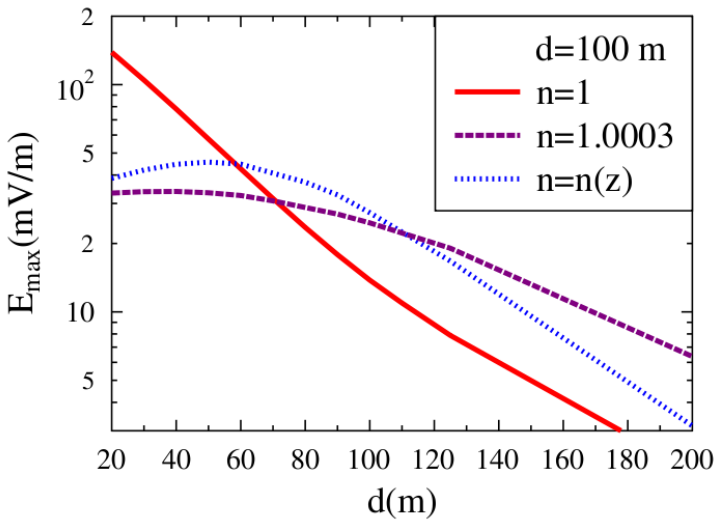

Figure 6.1: LDF of the pulse height as a function of distance to the shower core for the three choices for the index of refraction $n = 1$, $n = 1.0003$ fixed, and $n = n(z)$ realistic. Figure taken from [66]

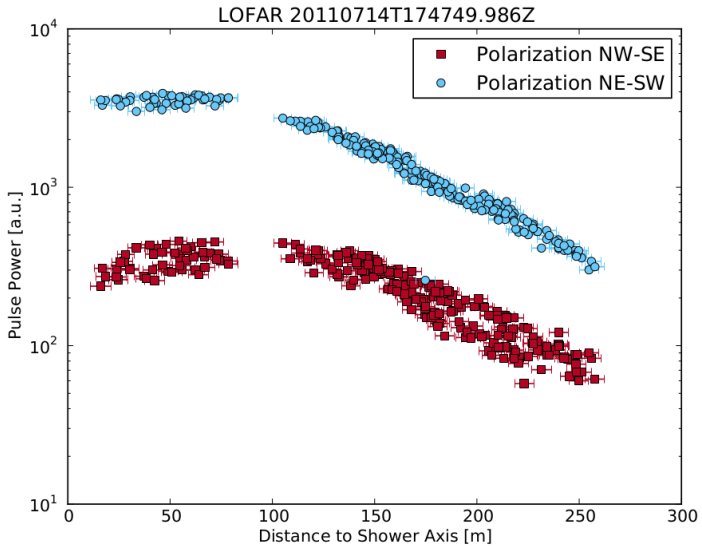

Figure 6.2: The LDF as measured for one of the LOFAR events. Figure taken from [92]

Chapter 7

Nederlandse samenvatting

In het begin van de 20e eeuw werd voor het eerst radioactieve straling waargenomen door Bequerel. Dit leidde tot verscheidene experimenten waar deze nieuwe straling werd onderzocht. In eerste instantie dacht men dat de straling veroorzaakt werd door materialen in onze aarde. Als de straling daadwerkelijk uit de aarde komt, zou deze moeten afnemen wanneer de metingen op grotere hoogte gedaan worden. Dit idee werd onder meer getest door Theodore Wulff. Hij verrichte metingen op de Eiffeltoren in Parijs. Het resultaat was dat de afname van de gemeten straling niet groot genoeg was. De enige conclusie was dan ook dat er nog een andere stralingsbron moest zijn. Deze bron werd gevonden door Victor Hess. In 1912 deed hij verscheidene experimenten met behulp van ballonvluchten om radioactieve straling te meten op verschillende hoogtes. Het resultaat van dit experiment is dat in eerste instantie de straling afneemt, maar nadat een hoogte is bereikt van enkele kilometers de straling weer toeneemt. De enig mogelijke conclusie is dat de straling vanuit ons universum komt, kosmische straling. Deze straling bestaat voornamelijk uit geladen deeltjes en atoomkernen.

Onze aarde wordt dagelijks gebombardeerd door kosmische straling. In 1939 was het Pierre Victor Auger die ontdekte dat de straling die op nabij gelegen plaatsen gemeten wordt, niet onafhankelijk is. Dit was de ontdekking van zogeheten deeltjeslawines. Wanneer een hoog energetisch deeltje uit ons universum op de atmosfeer van de aarde botst ontstaat er een lawine van nieuwe deeltjes die met ongeveer de lichtsnelheid richting het aardoppervlak vliegt. Afhankelijk van de energie van het inkomende kosmische deeltje bestaat de deeltjeslawine typisch uit een miljoen tot een miljard deeltjes.

De interesse in dit proefschrift gaat uit naar de meest energetische kosmische deeltjes die op dit moment bekend zijn. Op de hoogste energiën zijn deze deeltjes extreem zeldzaam. Op dit moment is er dan ook zeer

weinig bekend over deze kosmische straling. Wat voor deeltjes zijn het, is het een waterstofkern of een ijzerkern? Hoe komen ze aan deze extreme energiën? Waar komen ze vandaan? Op de hoogste energiën wordt de flux geschat op één deeltje per eeuw per vierkante kilometer. Om de meest energetische deeltjes toch te meten is dus een zeer groot oppervlak nodig. De grootste detectoren op dit moment zijn het Pierre Auger Observatorium in Argentinië en het Telescope Array in de Verenigde Staten. Hier worden de meest energetische deeltjes gemeten aan de hand van de geïnduceerde deeltjeslawine. De totale oppervlakte van deze detectoren bedraagt enkele duizenden vierkante kilometers.

Er zijn verschillende manieren om de geïnduceerde deeltjeslawines te detecteren. De twee meest gebruikte methodes zijn gronddetectoren en fluorescentiedetectoren. De gronddetectoren bestaan uit watertanks die geladen deeltjes in de lawine meten wanneer deze door de tanks bewegen. De fluorescentiedetectoren meten een zwak lichtsignaal dat in de lucht ontstaat wanneer een deeltjeslawine passeert. Dit proefschrift behandelt een nieuwe detectiemethode voor deze deeltjeslawines, namelijk radiodetectie. De deeltjeslawine bestaat voornamelijk uit geladen deeltjes, elektronen, positronen en muonen. De elektronen en positronen worden door hun lading in tegenovergestelde richting afgebogen in het aardmagneetveld. Deze ladingsscheiding levert een netto stroom op binnen de deeltjeslawine. De tijdsvariatie van de door deze stroom geïnduceerde potentiaal geeft vervolgens coherente straling in het MegaHertz (MHz) - GigaHertz (GHz) gebied. De coherentie op deze frequenties komt door de typische dimensies van de deeltjeswolk. De dikte van deze wolk varieert van enkele centimeters in het centrum tot enkele meters verder naar buiten. Een tweede stralingsmechanisme komt voort uit het feit dat er binnen de ladingswolk meer elektronen dan positronen aanwezig zijn. Dit komt onder andere doordat elektronen worden losgeslagen uit luchtmoleculen wanneer de wolk passeert.

Dit proefschrift begint met een beschrijving van het Macroscopic GeoMagnetic Radiation (MGMR) model. Dit model berekent de radiostraling aan de hand van analytische uitdrukkingen die de deeltjeslawine beschrijven. Een nieuwe wiskundige uitdrukking wordt bepaald die met name geschikt is om de radiostraling dichtbij de as van de deeltjeslawine te bepalen. Deze as is gedefinieerd als de fictieve lijn die vanaf het oorspronkelijke deeltje tot aan het aardoppervlak loopt. Verder wordt ook de interferentie tussen de emissie door de afbuiging van elektronen en positronen in het aardmagneetveld en de emissie door het ladingsoverschot in de deeltjeslawine behandeld. Het wordt duidelijk dat beide mechanismes gescheiden kunnen worden aan de hand van de polarisatie van het radiosignaal als functie van de antennepositie ten opzichte van de as van de deeltjeslawine.

Ook wordt de hybride versie van MGMR geïntroduceerd. In deze versie is het mogelijk is om het aantal deeltjes in de lawine als functie van tijd uit een Monte-Carlo simulatie te gebruiken in plaats van een analytische uitdrukking. Dit maakt het mogelijk om statistische fluctuaties mee te nemen in de berekening van het radiosignaal. Als voorbeeld hiervan wordt de signaalsterkte als functie van de afstand tot de as van de deeltjeslawine bepaald. Dit wordt gedaan voor verschillende kosmische deeltjes die op de aarde botsen, namelijk protonen en ijzerkernen. Het volgt dat door middel van het radiosignaal statistisch onderscheid gemaakt kan worden tussen de verschillende deeltjes.
Tijdens de ontwikkeling van het MGMR model werd duidelijk dat de voorspellingen van MGMR sterk verschilden met het op dat moment meest gebruikte model om radiostraling van de deeltjeslawine te berekenen, REAS. Door de totaal verschillende methodes die beide modellen gebruiken om de radiostraling te berekenen was het niet duidelijk wat de oorzaak was van dit verschil. Waar MGMR de macroscopische ladingsverdelingen van de deeltjeslawine gebruikt om de straling te berekenen, gebruikt REAS een microscopische beschrijving die de straling van elk individueel geladen deeltje berekent en optelt. De pulssterkte varieerde tot een factor tien tussen de beide modellen, waar de pulsvorm van MGMR bipolair is en die van REAS unipolair. In hoofdstuk drie wordt beschreven hoe de toevoeging van een extra stralingsmechanisme in het REAS model een groot deel van de verschillen kan verklaren. Het vervolg van dit hoofdstuk geeft een gedetailleerde vergelijking tussen de beide modellen na toevoeging van dit extra stralingsmechanisme. Het volgt dat beide modellen goed met elkaar overeenkomen en dat de emissiemechanismes hetzelfde zijn. De pulsvorm is voor beide modellen bipolair en de pulshoogte komt goed overeen ver van de as van de deeltjeslawine en verschilt tot een factor drie dichtbij de as. Dit verschil is zeer waarschijnlijk te verklaren door een aantal benaderingen in het MGMR model, waarbij de ladingswolk als een lijnstroom wordt beschouwd en de laterale uitgebreidheid dus niet wordt meegenomen. De dikte van de wolk wordt hierbij overschat. Dit volgt ook uit de berekeningen gedaan in hoofdstuk vier.
De berekeningen in hoofdstuk twee en drie zijn gedaan voor radio-emissie in vacuüm, ofwel met een brekingsindex gelijk aan één. In werkelijkheid vindt het stralingsproces in lucht met een eindige dichtheid plaats. Hoewel de brekingsindex van lucht zeer weinig afwijkt van zijn waarde in vacuüm (slechts enkele promillen), wordt in hoofdstuk vier aangetoond dat dit vergaande gevolgen heeft voor de berekende radiostraling. De snelheid van een radiosignaal in een dicht medium is langzamer dan de snelheid van hetzelfde signaal in vacuüm, de lichtsnelheid. De deeltjeslawine heeft echter zoveel

energie dat deze zich met de lichtsnelheid in vacuüm verplaatst. Hierdoor beweegt de bron van het uitgezonden signaal sneller dan het signaal zelf. Dit is te vergelijken met een vliegtuig die zich sneller voortplant dan de snelheid van het geluid, of een schip dat met hoge snelheid door het water beweegt. In beide gevallen heeft dit als gevolg dat het signaal extreem versterkt wordt, denk hierbij aan de knal op het moment dat een vliegtuig door de geluidsbarrière beweegt en de boeggolf van het schip. In het geval van elektromagnetische straling en dus ook radiostraling spreekt men van het Cherenkov effect. Dit is een geometrisch effect, dat alleen op vaste, relatief kleine, afstanden van de as van de deeltjeslawine plaatsvind. Dit is typisch tussen de 50 en 150 meter van de as. In de wiskundige uitdrukking voor het radiosignaal levert dit grote problemen op in de vorm van divergenties. Om deze divergenties veilig op te kunnen lossen, wordt gebruik gemaakt van de eindige dimensies van de ladingswolk. Hiervoor is de EVA code ontwikkeld. De macroscopische eigenschappen van de deeltjeslawine en de ladingswolk worden nu direct bepaald uit een Monte-Carlo simulatie. De verkregen ladingsverdelingen en stromen worden gefit om gladde analytische functies te verkrijgen. Deze dienen vervolgens als input voor de berekening van de radiostraling. Een belangrijk resultaat van de Monte-Carlo simulatie is dat de ladingsverdeling dichtbij de as van de deeltjeslawine zeer smal is. De dikte van de ladingswolk is van de orde van enkele centimeters, in plaats van meters wat tot dan toe aangenomen werd. De straling in het gebied waar Cherenkov effecten van belang zijn is typisch coherent over de dikte van de ladingswolk. Een dikte van de orde van centimeters geeft coherente radiostraling in het GHz gebied wat tot voorheen niet mogelijk werd geacht. Een ander belangrijk resultaat is dat de intensiteit van het radiosignaal voor een realistische brekingsindex niet constant afvalt als functie van de afstand tot de as van de deeltjeslawine. Dit was wel het geval voor berekeningen in het vacuüm. Het volgt dat er een piek in de intensiteit als functie van afstand tot de as van de deeltjeslawine ontstaat. De positie van de piek is direct gerelateerd aan de positie waar de deeltjeslawine het maximaal aantal elektronen en positronen heeft bereikt. Dit is van groot belang aangezien deze positie gebruikt wordt als maat voor de massa van het inkomende kosmische deeltje.

Een directe vergelijking met data is gegeven in hoofdstuk vijf. De data is gemeten bij het Pierre Auger Observatorium in Argentinië. Zoals in hoofdstuk twee, drie en vier in detail beschreven wordt zijn er twee mechanismes voor radiostraling van de deeltjeslawine. De eerste is door afbuiging in het aardmagneetveld, zogeheten geomagnetische straling. Dit mechanisme is inmiddels in meerdere experimenten aangetoond als het leidende emissiemechanisme. Het tweede emissiemechanisme is door een netto lad-

ingsoverschot in de deeltjeswolk. Dit mechanisme is tot nog toe niet aangetoond in een natuurlijk proces. Voor de datavergelijking in hoofdstuk vijf is de parameter R gedefinieerd. Deze parameter is in het geval van enkel geomagnetische straling altijd gelijk aan nul. In het geval van een extra emissiemechanisme zoals die door het ladingsoverschot zal deze afwijken van nul. In hoofdstuk vijf wordt aangetoond dat simulaties met de bijdrage door het ladingsoverschot een veel betere correlatie geven met de data dan simulaties met enkel het geomagnetische mechanisme. Dit resultaat is de eerste sterke aanwijzing dat de emissie door een netto ladingsoverschot in de ladingswolk daadwerkelijk voorkomt in een natuurlijk proces.

Chapter 8

Acknowledgements

The completion of this thesis would not have been possible without the support of many people. I will try to thank all of them even though it is merely impossible to do so without forgetting someone.
Of course there are my supervisors Olaf Scholten and Klaus Werner. Olaf, many thanks for your support the last five years. You were always available to answer my questions, to help me out if I could not solve a problem, or just for a friendly chat. During the many discussions we had, I really learned to do physics instead of blindly following the mathematical answers. I am looking forward to continue working with you in the future, of which I am sure will be the case. Klaus, many thanks for giving me the opportunity to come to Nantes for a few months to work on the development of the EVA code. I had a very nice stay in Nantes enjoying the weather and relaxed atmosphere. I enjoyed the many discussion we had about the mathematical and numerical framework of the EVA code.
I would like to thank Heino Falcke, Francis Halzen and David Seckel for being part of my reading committee. David, many thanks for the fruitful physics discussions we had at the conferences we both attended.
I would also like to thank my colleagues from the astroparticle physics group at KVI. I am very grateful to Ad van den Berg for the nice times at KVI and during the shift at the Pierre Auger observatory in Argentina. Many thanks for the discussions we had and the many times you gave me useful advice. Daniel, I very much enjoyed working with you. It was fun to discover that either Earth's magnetic field had flipped or someone interchanged a cable, luckily the latter was the case. I enjoyed the many discussions we had, and of course also the first exiting results of the charge-excess analysis. Wendy, many thanks for the nice chats we had about physics and soccer. Also many thanks for your help with the 'Nederlandse samenvatting' of this thesis. Stefano, thank you for the physics discussions and chats as my office mate at KVI. I really enjoyed the nice 'Italian'

style coffee we were able make using your coffee machine. I would like to thank Sybren and Stijn for the nice discussions and chats we had. Herbert, Nasser, Kader and Oksana I always enjoyed the nice APP lunches we had. I would also like to thank the people in Nijmegen, Charles, John, Harm, Stefan, José, Anna and Sander for the many nice discussions and collaboration.
Next to the astroparticle physics group, I also enjoyed being a member of the theory group. I would like to thank Daniel Boer, Rob Timmermans, and Lex Dieperink for their support. I always enjoyed the talks about soccer with Rob, who luckily did not support the wrong soccer team (even though opinions seem to differ about the definition of the wrong team). Also many thanks to my other colleagues at the theory group, Auke, Daren, Jacob, Keri, Laura, Lotje, Olena, Renato, Sophie and Wouter.
There are of course many others I would like to thank from KVI. Ronnie Hoekstra and Gerco Onderwater, many thanks for the nice chats during the lunches, coffee breaks and while playing volleyball. I would like to thank Peter Dendooven for giving me the opportunity to assist you with the Optics course. I would like to thank my office mates, Vanni, Mohammed and Elmer, for the nice chats we had. Ali, Ayan, David, Duurt, Ganesh, Geert, Hans, Joost, Mayerlin, Ola, Olga, Oscar, Stefan, Steven, Bodha, Corine, Wilbert many thanks for giving me a nice time at KVI. Amarins, thanks for the nice chats we had and all the volleyball matches we played. Annet, Carla, Eveline, Grietje, Harry, Hilde, Marjan, Miranda, Robert and Simone, many thanks for your support during the last five years at KVI.
Jordy de Vries, thank you for being a good friend and my paranimph. I enjoyed being your room mate, despite the little soccer issue we have (something with supporting the wrong team). I would also like to thank Henry, Martin and Stijn for the nice times we had in Groningen. Corien, thanks for the good times as my room mate and helping me out with the layout of my thesis. Frank, many thanks for the fun and drinks we had as a room mate and while playing in the same soccer team. Also many thanks to all the other team members I had playing indoor soccer in Groningen. Henk, many thanks for the good times in Groningen as well as Ootmarsum. Aline, thanks for making the trip from Groningen to Ootmarsum less boring for many times.
Next to all the people in Groningen, there are of course my friends from Ootmarsum I would like to thank for their support during the (often tough times in) the weekends. Bram, Brian, Cas, Daan, Dirk, Gert-Jan, Gijs, Jan, Joris, Nick, Niels, Peter, Robbert, Rudy, Roy, Roy, Tom, Toon, many thanks for the good times. I would also like to thank the members of the 'klootschiet' and soccer teams I join.

To conclude I am very thankful to my family, father, mother and brother for all the support you have given me throughout the years. I am very grateful that you have always supported me in the choices I made. This thesis would not have been possible without you.

Chapter 9

Publications

9.1 Refereed publications

2012 *A Realistic Treatment of Geomagnetic Cherenkov Radiation from Cosmic Ray Air Showers*
K. Werner, K.D. de Vries, O. Scholten
Astropart. Phys. **37**, 516 (2012)

Macroscopic Geo-Magnetic Radiation model; polarization effects and finite volume calculations.
K.D. de Vries, O. Scholten, K. Werner
Nucl. Inst. Meth. A **662**, S175-S178 (2012)

Coherent radiation from extensive air showers
O. Scholten, K.D. de Vries, K. Werner
Nucl. Inst. Meth. A **662**, S80-S84 (2012)

The convergence of EAS radio emission models and a detailed comparison of REAS3 and MGMR simulations.
T. Huege, M. Ludwig, O. Scholten, K.D. de Vries
Nucl. Instr. Meth. A **662**, S179-S186 (2012)

Search for signatures of magnetically-induced alignment in the arrival directions measured by the Pierre Auger Observatory.
P. Abreu *et al.*, The Pierre Auger Observatory Collaboration [K.D. de Vries]
Astropart. Phys. **35**, 354-361 (2012)

2011 *Coherent Cherenkov Radiation from Cosmic-Ray-Induced Air Showers*
K.D. de Vries, A.M. van den Berg, O. Scholten, K. Werner
Phys. Rev. Lett. **107**, 061101 (2011)

Advanced functionality for radio analysis in the Offline software framework of the Pierre Auger Observatory.
P. Abreu *et al.*, The Pierre Auger Observatory Collaboration [K.D. de Vries]
Nucl. Inst. Meth. A **635**, 92-102 (2011)

The effect of the geomagnetic field on cosmic ray energy estimates and large scale anisotropy searches on data from the Pierre Auger Observatory.
P. Abreu *et al.*, The Pierre Auger Observatory Collaboration [K.D. de Vries]
JCAP **1111**, 022 (2011)

The exposure of the hybrid detector of the Pierre Auger Observatory.
P. Abreu *et al.*, The Pierre Auger Observatory Collaboration [K.D. de Vries]
Astropart. Phys. **34**, 368-381 (2011)

The Pierre Auger Observatory scaler mode for the study of solar activity modulation of galactic cosmic rays.
P. Abreu *et al.*, The Pierre Auger Observatory Collaboration [K.D. de Vries]
JINST **6**, P01003 (2011)

Search for First Harmonic Modulation in the Right Ascension Distribution of Cosmic Rays Detected at the Pierre Auger Observatory.
P. Abreu *et al.*, The Pierre Auger Observatory Collaboration [K.D. de Vries]
Astropart. Phys. **34**, 627-639 (2011)

Anisotropy and chemical composition of ultra-high energy cosmic rays using arrival directions measured by the Pierre Auger Observatory.
P. Abreu *et al.*, The Pierre Auger Observatory Collaboration [K.D. de Vries]
JCAP **1106**, 022 (2011)

The Lateral Trigger Probability function for the ultra-high energy cosmic ray showers detected by the Pierre Auger Observatory.
P. Abreu *et al.*, The Pierre Auger Observatory Collaboration [K.D. de Vries]
Astropart. Phys. **35**, 266-276 (2011)

2010 *The lateral distribution function of coherent radio emission from extensive air showers: Determining the chemical composition of cosmic rays.*
K.D. de Vries, A.M. van den Berg, O. Scholten, K. Werner
Astropart. Phys. **34**, 267-273 (2010)

A new limit on the Ultra-High-Energy Cosmic-Ray flux with the Westerbork Synthesis Radio Telescope.
S. ter Veen, S. Buitink, H. Falcke, C.W. James, M. Mevius, O. Scholten, K. Singh, B. Stappers, K.D. de Vries
Phys. Rev. D **82**, 103014 (2010)

Update on the correlation of the highest energy cosmic rays with nearby extragalactic matter.
P. Abreu *et al.*, The Pierre Auger Observatory Collaboration [K.D. de Vries]
Astropart. Phys. **34**, 314-326 (2010)

Atmospheric effects on extensive air showers observed with the Surface Detector of the Pierre Auger Observatory.
J. Abraham *et al.*, The Pierre Auger Observatory Collaboration [K.D. de Vries]
Astropart. Phys. **32**, 89-99 (2009), Erratum-ibid. **33**, 65-67 (2010)

The Fluorescence Detector of the Pierre Auger Observatory.
J. Abraham *et al.*, The Pierre Auger Observatory Collaboration [K.D. de Vries]
Nucl. Inst. Meth.A **620**, 227-251 (2010)

A Study of the Effect of Molecular and Aerosol Conditions in the Atmosphere on Air Fluorescence Measurements at the Pierre Auger Observatory.
J. Abraham *et al.*, The Pierre Auger Observatory Collaboration [K.D. de Vries]
Astropart. Phys. **33**, 108-129 (2010)

Measurement of the Depth of Maximum of Extensive Air Showers above 10^{18} *eV.*
J. Abraham *et al.*, The Pierre Auger Observatory Collaboration [K.D. de Vries]
Phys. Rev. Lett. **104**, 091101 (2010)

Measurement of the energy spectrum of cosmic rays above 10^{18} *eV using the Pierre Auger Observatory.*
J. Abraham *et al.*, The Pierre Auger Observatory Collaboration [K.D. de Vries]
Phys. Lett. B **685**, 239-246 (2010)

Trigger and aperture of the surface detector array of the Pierre Auger Observatory.
J. Abraham *et al.*, The Pierre Auger Observatory Collaboration [K.D. de Vries]
Nucl. Inst. Meth. A **613**, 29-39 (2010)

9.2 Non-refereed conference proceedings

2011 *Cherenkov effects in radio emission from cosmic-ray induced air showers*
K.D. de Vries, A.M. van den Berg, O. Scholten, K. Werner
32nd International Cosmic Ray Conference
Beijing, China

A detailed comparison of MGMR and REAS3 simulations
M. Ludwig, T. Huege, O. Scholten, K.D. de Vries
32nd International Cosmic Ray Conference
Beijing, China

2009 *Modeling coherent geomagnetic radiation from cosmic ray induced air showers*
K.D. de Vries, O. Scholten, K. Werner
31th International Cosmic Ray Conference
Lodz, Poland

9.3 Internal notes Pierre Auger collaboration

2012 *Methods for polarization analysis of cosmic-ray induced radio pulses*
E.D. Fraenkel, A.M. van den Berg, O. Scholten, K.D. de Vries
under review

2011 *Observation of the charge-excess effect in cosmic-ray-induced radio pulses*
E.D. Fraenkel, K.D. de Vries, W. Docters, O. Scholten, A.M. van den Berg
GAP-2011-097

Locating transient noise sources at Radio Detection sites
A.M. van den Berg, W. Docters, E.D. Fraenkel, K.D. de Vries, K. Weidenhaupt
GAP 2011-083

Physics data set from MAXIMA
A.M. van den Berg, A. Aminaei, J. Coppens, W. Docters, H. Falcke, E. D. Fraenkel, S. Grebe, S. Harmsma, J.R. Hörandel, S. de Jong, J.L. Kelley, A. Nelles, O. Scholten, H. Schoorlemmer, C. Timmermans, K.D. de Vries, G. Zarza
GAP 2011-009

2010 *The radio extension of Auger Offline*
S. Fliescher, D. Fraenkel, B. Fuchs, S. Grebe, T. Huege, M. Konzack, M. Melissas, P. Oliva, N. Palmieri, J. Rautenberg, A. Schmidt, H. Schoorlemmer, F. Schröder, A. Stutz, K.D. de Vries
GAP 2010-056

9.4 Submitted articles

2012 *The air shower maximum probed by Cherenkov effects from radio emission*
K.D. de Vries, O. Scholten, K. Werner
Submitted to Astroparticle Physics

The EVA code; Macroscopic modeling of radio emission from air showers based on full MC simulations including a realistic index of refraction.
K.D. de Vries, O. Scholten, K. Werner
Submitted to AIP Conference Series

First results from EVA simulations; Cherenkov effects and the composition of the initial cosmic ray
K.D. de Vries, O. Scholten, K. Werner
Submitted to AIP Conference Series

What the radio signal tells about the cosmic-ray air shower
O. Scholten, K.D. de Vries, K. Werner
Submitted to EPJ Conference Series

Bibliography

[1] "The Nobel Prize in Physics 1903". Nobelprize.org. 25 Jul 2012 http://www.nobelprize.org/nobel_prizes/physics/laureates/1903

[2] T. Wulf, Phys. Zeitschr. **10**, 997 (1909)

[3] V. Hess, Phys. Zeitschr. **13**, 1084 (1912)

[4] P.A.M. Dirac, Proc. R. Soc. Lond. A **117**, 610 (1928)

[5] Carl D. Anderson, Physical Review **43(6)**, 491 (1933)

[6] "The Nobel Prize in Physics 1936". Nobelprize.org. 25 Jul 2012 http://www.nobelprize.org/nobel_prizes/physics/laureates/1936

[7] P. Auger et al., Rev. Mod. Phys. **11(34)**, 288 (1939)

[8] J. Linsley, Phys. Rev. Lett. **10**, 146 (1963)

[9] K. Greisen, Phys. Rev. Lett. **16**, 748 (1966)

[10] G.T. Zatsepin, V.A. Kuzmin, Pisma Zh. Eksp. Teor. Fiz.**4**, 114 (1966)

[11] C.J. Bell, et al., J. Phys. A **12**, 990 (1974)

[12] D.M. Edge, A.C. Evans, H.J. Garmston, J. Phys. A**6**, 1612 (1973)

[13] B.N. Afanasiev, et al. in: M. Nagano (Ed.), Proceedings of the Tokyo Workshop on Techniques for the Study of Extremely High Energy Cosmic Rays

[14] N. Chiba, et al., AGASA Collab., Nucl. Instrum. Methods A **311**, 338 (1992)

[15] R. Abbasi, et al., HiRes Collab., Phys. Rev. Lett. **100**, 101101 (2008)

[16] Karl-Heinz Kampert for the Pierre Auger Collaboration, Proc. of 32nd ICRC, Beijing, China, 2011

[17] H. Kawai, et al., TA Collab., Nuclear Phys. Proc. Suppl. **175**, 221 (2008)

[18] W. Heitler. The Quantum theory of Radiation, Oxford Univ. Press (1954)

[19] J. Matthews, Astropart. Phys. **22**, 387 (2005)

[20] D. Heck et al., FZKA Report 6019 (1998)

[21] G. Bossard, H.J. Drescher, N.N. Kalmykov, S. Ostapchenko, A.I. Pavlov, T. Pierog, E.A. Vishnevskaya, and K. Werner, Phys.Rev. **D63**, 054030 (2001)

[22] T. Bergmann, R. Engel, D. Heck, N.N. Kalmykov, Sergey Ostapchenko, T. Pierog, T. Thouw, K. Werner, Astropart.Phys. **26**, 420 (2007)

[23] T. Abu-Zayyad, et al., HiRes-MIA Collaboration, Phys. Rev. Lett. **84**, 4276 (2000)

[24] R. Engel for the Pierre Auger Collaboration, Proc. of the 30th ICRC, Merida, Mexico **4**, 385 (2007)

[25] H.S. Ahn, et al. ATIC-2 Collab., Proc. of 28th ICRC, Tsukuba, Japan , 1853 (2003)

[26] N.L. Grigorov, et al., Yad. Fiz. **11**, 1058 (1970)

[27] N.L. Grigorov, et al., Proc. of 12th ICRC., Hobart, Australia **2**, 206 (1971)

[28] V. Derbina, et al., Astrophys. J. **628**, 41 (2005)

[29] M. Amenomori, et al., Tibet AS Collaboration, Astrophys. J. **678**, 1165 (2008)

[30] T. Antoni, et al., KASCADE Collaboration, Astropart. Phys. **24**, 1 (2005)

[31] J.C. Arteaga-Velazques, et al. KASCADE-Grande Collaboration, Proc. of 15th Int. Symposium on Very High-Energy Cosmic Ray Interactions, Paris, 2008

[32] M. Nagano, et al., J. Phys. **G10**, 1295 (1984)

[33] M. Nagano, et al., J. Phys. **G18**, 423 (1992)

[34] T. Abu-Zayyad, et al., HiRes-MIA Collaboration, Astrophys. J. **557**, 686 (2001)

[35] J. Abraham, et al., Pierre Auger Collaboration, Phys. Rev. Lett. **101**, 061101 (2008)

[36] J. Blmer, R. Engel, J.R. Hrandel, Progress in Particle and Nuclear Physics **63**, 293 (2009)

[37] F. Salmida for the Pierre Auger Collaboration, Proc. of the 32nd ICRC, Beijing, China, 2011

[38] D.I Keda, H.S Agawa, Y.T Sunesada, D.C. Rodriquez, T.Z.A AbuZayyad, for the Telescope Array Collaboration, Proc. of the 32nd ICRC, Beijing, China, 2011

[39] H.R. Allan: Progress in Elementary Particle and Cosmic Ray Physics; **10**, 171 (1971)

[40] P.M.S. Blackett and A.C.B. Lovell. Proc. Phys. Soc. London A **177**, 183 (1941)

[41] J.V. Jelley, et al., Nature **205**, 658 (1965)

[42] H.R. Allan et al. Nature **225**, 253 (1970)

[43] D.J. Fegan and D.M. Jennings, Nature **223**, 722 (1969)

[44] G.A. Askaryan, Sov. Phys. JETP **14**, 441 (1962); **21**, 658 (1965)

[45] F.D. Kahn and I. Lerche, Proc. Royal Soc. London **A289**, 206 (1966)

[46] S.A. Colgate, J. Geophys. Res. **19**, 4896 (1967)

[47] M. Fuji and J. Nishimura, in Proc. 11th IUPAP Conf. on Cosmic Rays, Budapest, 1969

[48] C. Castagnoli, G. Silvestro, P. Picchi, and G. Verri, Nuovo Cimento **63B**, 373 (1969)

[49] H. Falcke, et al., Nature **435**, 313 (2005)

[50] W. D. Apel, et al., Astropart. Phys. **26**, 332 (2006)

[51] D. Ardouin, et al., Astropart. Phys. **26**, 341 (2006)

[52] D. Ardouin and the CODALEMA Collaboration, Astropart. Phys. 31 **3**, 192-200 (2009)

[53] A.M. van den Berg for the Pierre Auger Collaboration, Proc. of the 30th ICRC, Merida, Mexico **5**, 885 (2008)

[54] J. Coppens, Pierre Auger Coll., Nucl. Instr. and Meth. A **604**, S41 (2009)

[55] B. Revenu, Pierre Auger Coll., Nucl. Instr. and Meth. A **604**, S37 (2009)

[56] S. Fliescher, Pierre Auger Coll., Nucl. Instr. and Meth. A **662**, S124-S129 (2012)

[57] A. Horneffer, et al., LOFAR CR-KSP, Nucl. Instr. and Meth. A 6172010482

[58] S. Böser for the IceCube collaboration, Nucl. Instr. and Meth. A 6622012S66

[59] H. Falcke and P. Gorham, Astropart. Phys. **19**, 477 (2003)

[60] D.A. Suprun, P.W. Gorham, J.L. Rosner, Astropart. Phys. **20**, 157 (2003)

[61] T. Huege, H. Falcke, Astronomy & Astrophysics **430**, 779 (2005)

[62] Olaf Scholten, Klaus Werner, Febdian Rusydi, Astropart. Phys. **29**, 94 (2008)

[63] K.D. de Vries, A.M. van den Berg, Olaf Scholten, Klaus Werner, Astropart. Phys. **34**, 267 (2010)

[64] T. Huege, M. Ludwig, O. Scholten, K.D. de Vries, Nucl. Instr. and Meth. A **662**, S179 (2012)

[65] H. Schoorlemmer for the Pierre Auger Collaboration, Nucl. Instr. and Meth. A **662**, S134 (2012)

[66] K.D. de Vries, A.M. van den Berg, O. Scholten, K. Werner, Phys.Rev.Lett. 107 2011 061101

[67] T. Huege, M. Ludwig, C. James, proceedings of ARENA 2012, to be published

[68] J. Alvarez-Muniz, W. R. Carvalho, Jr., E. Zas, Astropart. Phys. **35**, 325-341 (2012)

[69] V. Marin, B. Revenu, Astropart. Phys.**35**, 733-741 (2012)

[70] K. Werner, K.D. de Vries, O. Scholten, Astropart. Phys. **37**, 516 (2012)

[71] S. Hoover et al., PRL **105**, 151101 (2010)

[72] M. Ludwig, T. Huege, Astrop. Phys. 34 (2011) 438–446

[73] Klaus Werner and Olaf Scholten, Astropart. Phys. **29**, 393 (2008)

[74] T. Huege, R. Ulrich, R. Engel, Astropart. Phys. **30**, 96 (2008)

[75] N.A. Porter, C.D. Long, B. McBreen, D.J.B Murnaghan and T.C. Weekes, Phys. Lett. **19**, 415 (1965)

[76] O. Scholten and K. Werner, Nucl. Instr. and Meth. A **604**, S24 (2009).

[77] T. Gousset, J. Lamblin, and S. Valcares, Astropart. Phys.**31**, 52 (2009).

[78] C. Riviere, Nucl. Instr. and Meth. A **662**, S191 (2012)

[79] V. Marin, Nucl. Instr. and Meth. A **662**, S171 (2012)

[80] M. Ludwig, and T. Huege, Nucl. Instr. and Meth. A 6622012S164

[81] J. Knapp et al., Astropart. Phys. **19**, 77 (2003)

[82] T. Huege, H. Falcke, Astronomy & Astrophysics **412**, 19 (2003)

[83] G. Agnetta et al., Astropart. Phys. **6**, 301 (2003)

[84] J.D. Jackson, Classical Electrodynamics, Wiley, New York, 1999

[85] G.N. Afanasiev, V.G. Kartavenko, and Yu.P. Stepanovsky, J. Phys. D **32**, 2029 (1999)

[86] W.D. Apel et al. -LOPES collaboration, Astropart. Phys. **32**, 294 (2010)

[87] C. W. James, H. Falcke, T. Huege, M. Ludwig, Phys. Rev. E (submitted), arXiv:1007.4146

[88] M. Ludwig, T. Huege, Proc. of the 32nd ICRC Beijing, China, 2011

[89] N.N. Kalmykov, A.A. Konstantinov, and R. Engel, Nucl. Phys. B **151**, 347 (2006); Phys. At. Nucl. **73**, 1191 (2010)

[90] W.R. Nelson et al., The EGS4 Code System, SLAC report 265, 1985

[91] K.D. de Vries, O. Scholten, and K. Werner, Nucl. Instr. and Meth. A **662**, S175 (2012)

[92] A. Corstanje et al, arXiv:1109.5805v1, Proc. of the 32nd ICRC, Beijing, China, 2011

[93] ANITA Collab: S. Hoover et al., To be submitted to Phys. Rev. Lett arXiv:1005.0035v2

[94] K.D. de Vries, O. Scholten, and K. Werner, Proc 31th ICRC, Lodz, Poland, 2009

[95] V. Marin for the CODALEMA Collaboration, Proc. 32nd ICRC, Beijing, China **1**, 291 (2011)

[96] P.W. Gorham et. al., Phys. Rev. Lett. **103**, 051103 (2009)

[97] O. Scholten et. al., Phys. Rev. Lett. **103**, 191301 (2009)

[98] E.D. Fraenkel for the Pierre Auger Collaboration, Proc. of the 23rd ECRS, Moscow, Russia, To be published.

[99] F. Sánchez for the Pierre Auger Collaboration, Proc. of the 32nd ICRC Beijing, China, 2011

[100] P.S. Allison, for the Pierre Auger Collaboration, Proc. of the 32nd ICRC Beijing, China, 2011

[101] J.L. Kelley, for the Pierre Auger Collaboration, Proc. of the 32nd ICRC Beijing, China, 2011

[102] Pierre Auger Collaboration (P. Abreu (Lisbon, IST) et al.). Nucl. Instr. and Meth. A **635**, 92 (2011)

[103] E.D. Fraenkel, A.M. van den Berg and O. Scholten., Technical report, [Pierre Auger Collaboration], GAP 2011-051.

[104] A. Letessier-Salvon, Technical report, [Pierre Auger Collaboration], GAP 1999-03

[105] J. Neuser, K.-H. Kampert, J. Rautenberg, Technical report, [Pierre Auger Collaboration], GAP 2011-070

[106] E.D. Fraenkel, A.M. van den Berg, O. Scholten and K.D. de Vries. Technical report, [Pierre Auger Collaboration], GAP Note currently under review by AERA group.